FINAL SCIENTIFIC/TECHNICAL REPORT

Project Title: Great Plains Wind Power Test Facility

Award Number: DE-FG-06-GO86092
Project Period: 08/15/2006 through 09/30/2013
Principle Investigator: John Schroeder, Ph.D., Professor of Atmospheric Science. Email: john.schroeder@ttu.edu; Tel: 806-834-5678

Recipient: Texas Tech University; DUNS#: 041367053

Working Partners: Elahi Mehran, Elizabeth State University, melahi@mail.ecsu.edu

Cost-Sharing Partners: N/A

DOE Project Team: DOE HQ Program Manager – Jose Zayas
DOE Field Contract Officer – Pamela Brodie
DOE Field Grants Management Specialist – Fania Gordon
DOE Field Project Officer – Brad Ring
DOE/CNJV Project Monitor – Melissa Callaway

Date of Report: 01/30/2014

Signature of Submitting Official:
(Electronic signature is acceptable)

Acknowledgement: This report is based upon work supported by the U.S. Department of Energy under Award No. DE-FG-06-GO86092.

Disclaimer: Any findings, opinions and conclusions or recommendations expressed in this report are those of the author(s) and do not necessarily reflect the views of the Department of Energy.

Proprietary Data Notice: There is no proprietary material contained in this report.

Table of Contents

List of Acronyms

AEP - Annual Energy Production
AGL - Above Ground Level
CAPE - Connective Available Potential Energy
CDF - Cumulative Distribution Function
CGST - Center for Geospatial Technology
CPNL - Coefficient of Performance Net of Losses
CMOS - Complementary metal-oxide-semiconductor
DTU - Danish Technical University
EPA - Environmental Protection Agency
EPSD - Evolutionary Power Spectral Density
FAST - Fatigue, Aerodynamic, Structures and Turbulence code
GEV - Generalized Extreme Value
IDEAL - Institute for the Development and Enrichment of Advanced Learners
IEC - International Electrotechnical Commission
LEUWCD - Llano Estacado Underground Water Conservation District
MAR - Multivariate Autoregressive Modeling
MCPE - Marginal Clearing Price of Energy
MCS - Monte Carlo Simulation
MRI - Mean Recurrence Intervals
NMED - New Mexico Environment Department
NI - National Instruments
NREL - National Renewable Energy Laboratory
NWI - National Wind Institute
PSC - Parkhill Smith and Cooper, Inc.
SCOUT - Severe Convective OUtflow in Thunderstorms
PPA - Power Purchase Agreement
PPI - Plan Position Indicator
PV - Photovoltaic
RHI - Range Height Indicator
RTC - Reese Technology Center
RTI - Running Turbulence Intensities
SECO - State Energy Conservation Office
SWiFT - Scaled Wind Farm Technology facility
SODAR - Sound Detection and Ranging
TTU - Texas Tech University
TCEQ - Texas Commission for Environmental Quality
TDA - Texas Department of Agriculture
THP - Texas High Plains
TWDB - Texas Water Development Board
WRC - Water Resources Center
WiSE - Wind Science and Engineering Research Center (now called National Wind Institute)
WTM - West Texas Mesonet
WTWWS - West Texas Water Well Service

List of Figures

List of Tables

Executive Summary

This multi-year, multi-faceted project was focused on the continued development of a nationally-recognized facility for the testing, characterization, and improvement of grid-connected wind turbines, integrated wind-water desalination systems, and related educational and outreach topics. The project involved numerous faculty and graduate students from various engineering departments, as well as others from the departments of Geosciences (in particular the Atmospheric Science Group) and Economics. It was organized through the National Wind Institute (NWI), which serves as an intellectual hub for interdisciplinary and transdisciplinary research, commercialization and education related to wind science, wind energy, wind engineering and wind hazard mitigation at Texas Tech University (TTU). Largely executed by an academic based team, the project resulted in approximately 38 peer-reviewed publications, 99 conference presentations, the development/expansion of several experimental facilities, and two provisional patents.

> Provisional Patent (filed 07/27/2012), System and Method for Evaluating Wind Flow Fields Using Remote Sensing Devices, Application Number: US61/676,394 - Schroeder, J. L., B. D. Hirth, and J. G. Guynes.
>
> Provisional Patent (filed 08/14/2012), Apparatus and Method for Using Radar to Evaluate Wind Flow Fields for Wind Energy, Application Number: 61/683,022 - Schroeder, J. L., J. G. Guynes, and B. D. Hirth.

The first research and development task was largely focused on documentation of wind flow characteristics found in the US Great Plains and assessing their impacts on turbine reliability and performance. While initiated with a broader base of activity, including subtasks focused on the evaluation of asymmetric spur gears in wind turbine design, the development of a turbine health monitoring system, and a Ph.D. dissertation studying the applicability of firming wind energy with solar energy; as time elapsed, this task became more focused on complex wind flow characterization and its inherent link to turbine performance and reliability. This research thrust mimics the natural strength of the atmospheric science and engineering groups at TTU and the long established research history. This task also resulted in the continued development and maintenance of various field facilities supporting various facets of wind energy research, including a 200 m meteorological tower located at Reese Technology Center, the West Texas Mesonet and the TTUKa radars. Important results include the establishment of an upgraded, well maintained, and well instrumented site which now supports the DOE/Sandia National Laboratory Scaled Wind Farm Technology Facility; the development of two TTUKa research radars that have been used to offer unprecedented cinematic animations and data fields of complex flows of importance to wind energy; and the development of conditional simulation techniques that offer a more realistic integration and replication of inflow conditions and characteristics across the rotor sweep.

The second research and development task was focused on integrated wind-water desalination systems. West Texas is geographically located at the nexus of the wind-water opportunity as it is found in the heart of the wind energy development region, while also extracting the majority of its water supply from a depleting aquifer. Opportunities exist to assist rural communities struggling to provide potable water systems that meet state and federal requirements, and this task was largely focused on the creation of a

integrated wind-water demonstration system in Seminole, Texas using a wind turbine and a reverse osmosis treatment system. This successful integration occurred by amassing a significant number of partners including the City of Seminole, the Texas Water Development Board, the Renewable Energy Demonstration Pilot Program in the Texas Department of Agriculture, and the State Energy Conservation Office.

As TTU is an institution of higher education, the remaining task was dedicated to education and outreach efforts. This included numerous facility tours, the organization and presentation of technical materials at national and international conferences, the development of an annual “Run on the Wind” summer camps for middle school children as well as a curriculum for middle school teachers, and maintaining web and social media sites.

Introduction

This project was divided into three main tasks. Task 1 was largely dedicated to research and development efforts to characterize the wind flow and weather events common to the Great Plains and to understand their impact on wind turbine performance, loading and fatigue. Task 2 was dedicated to research and development of coupling wind power with water treatment technologies to lower the energy costs associated with desalination. The remaining task was dedicated to wind energy educational and outreach efforts. Project contributions were as diverse as the faculty base that participated in the project.

Perhaps the single most significant result of task 1 is the development and usage of the TTUKa research radar technologies and associated techniques to measure the complex flows of the atmospheric boundary layer. In October 2011, the TTU team used the technology to instantaneously track a single utility scale turbine wake for more than 30 rotor diameters downwind. This initial accomplishment far exceeded the capabilities of available LIDAR technologies, even though LIDAR technologies had already been "matured" in the market for 5-10 years. Building upon this success, the team quickly collected another dataset, this time using two radar systems to fully define the horizontal wind field using dual Doppler synthesis techniques. This information not only allowed for the study of wake evolution and structure, but also provided details about the inflow conditions across the entire rotor sweep, which was later used to accurately predict power output from the turbine. In the summer of 2012, the team acquired several data sets from large wind arrays containing 35-70 turbines each. These initial data sets were analyzed and the team published the world's first dual Doppler analysis of the complex flows across a wind plant in 2013. This analysis included documentation of wake structure and evolution, turbine-to-turbine interaction, enhanced "wind channels" between turbine wakes, the influence of nearby terrain, transient gusts and lulls, and even array edge effects. Working with an industry partner, the team was able to obtain high temporal resolution wind turbine power output data and relate it to the radar-derived inflow fields. This comparison yielded a comprehensive and independent power curve for the wind plant. TTU has filed for patents to cover the usage of dual-Doppler radar technologies and techniques for wind energy applications. The conversation process for these patents is currently ongoing.

The most significant contribution of Task 2 was the assembly of a pilot-scale field demonstration of wind-powered desalination of brackish groundwater in cooperation with the town of Seminole, Texas. In 2005, researchers from TTU's NWI and Water Resources Center (WRC) began exploring the potential for connecting locally owned renewable wind energy systems with the electrical needs for pumping and treating locally available brackish groundwater. Electricity can be up to 50 percent of the total cost of the treatment, and behind-the-meter application of renewable energy can reduce the community's grid electricity needs when the wind is sufficient, essentially storing lower cost energy in the produced water. Seminole, a town of about 6,400 residents with a declining Ogallala well field impacted by arsenic and fluoride, became a suitable partner as city officials were interested in drilling deeper wells into the Dockum formation to tap the water in Santa Rosa aquifer. The NWI and WRC research team worked with the City to develop and deploy a field-scale demonstration project with funding from several local, state, and federal sources. Operation began in July 2013 for a planned 12-month period. The results will provide operational experience and economic data for planning of larger-scale systems.

Task 3 was focused on education and outreach activities associated with the broad technical work, and the promotion of wind energy in general. These activities include developing summer camps and curriculum materials for middle school children, numerous presentations at technical conferences, and providing a multitude of tours to various participants from US Senators and Representatives to local school groups. While this education and outreach mission is important, this technical report focuses mainly on documenting the results and outcomes which emanated from the research development tasks.

Internally at TTU, the overall project was administered by NWI, with each task divided into subtasks, which were each led by a principle investigator(s). Some faculty contributed to multiple subtasks, while others only contributed to one. Some faculty participated in activities during the entire project duration, while others did not. Given the diversity and the broad foundation of the project's activity and its structure, this report is organized in a manner that follows each subtask, providing background information, results, discussions and conclusions, as appropriate for each subtask.

Task 1: Research and Development: Great Plains Wind Characteristics and their Effects on Turbine Reliability.

Task 1 was largely focused on research and development activities associated with measurement of Great Plains wind characteristics and their impacts on turbine performance and reliability. However, a few ancillary tasks, which were independent of wind flow characterization, were also included w.r.t. wind turbine performance and reliability. Task 1 was divided into 10 subtasks, which are each summarized.

Subtask 1.1: Maintain/Upgrade 200 m Tower, TTUKa Radars and WTM Observational Facilities.

1.1.1. The 200 m Instrumented Tower Located at Reese Technology Center.

The TTU 200 m tower represents the only research-grade meteorological tower of its kind in the United States. Established in 2001, the tower platforms collect wind, temperature, relative humidity and pressure measurements at 10 individual instrumentation levels 24 hours per day. While extremely valuable, the tower system had been plagued by poor quality. Inconsistent and noisy data from the full sensor array, as well as communications and general power distribution problems, were prevalent to an extent that the tower data had been deemed unusable on many occasions for research purposes prior to and during 2009. Starting in 2010, TTU made a significant effort to upgrade and solve the remaining technical issues.

Initially, the 200 m tower AC power distribution system at the Reese Field Site was analyzed and several ground loop problems that existed between the lightning protection system, the earth grounding system, the three-phase return line reference, the tower single-phase return line reference, the tower uninterruptable power distribution system and each of the other field site systems were resolved. Resolving the various ground loop problems completely removed the 60 cycle AC line noise from being transferred throughout the tower distribution system, referenced each DC sensor supply system to the same AC return line potential, and resulted in an overall noise reduction at the various sensor excitation supplies of over 3:1.

Next, all sensor data cables and connections were verified, reconfigured or replaced in order to establish system wide standardization of proper grounding termination, shielding, excitation and/or sensor reference supply, noise immunity and impedance matching techniques. This operation resulted in a significant increase in the dynamic measurement range of each input channel by reducing the average single-ended sensor noise level output amplitude by more than 50% system wide, as read at the input of each data acquistion channel.

Even after significant improvement in overall noise reduction had been achieved, the West Texas Mesonet had mounted a VHF transceiver system to the tower which posed serious intermodulation difficulties, resulting in significant voltage spikes being induced onto the data stream for various sensors within the vicinity of the antenna system. Work then began in order to establish other means of real-time data telemetry for the few remaining stations within the WTM that were still utilizing the VHF tower network. The VHF radio network was shutdown and the RF equipment was completely removed from the tower in 2011.

Beginning in the Fall of 2011, major hardware and software improvements were made to the TTU 200 m instrumented tower to enhance performance, measurement capabilities and data quality while continuously reducing system noise. Pre-existing RM Young analog ultra-sonic wind sensors were upgraded to Gil research-grade digital sonic units. These new sonics allowed for an increased sampling rate (50 Hz), simplified data stream, and improved data quality. The implementation of the new sonic sensors was accompanied by an upgrade to the entire tower data acquisition hardware and software system. Tower data acquisition hardware was upgraded from the antiquated National Instruments (NI) Compact Fieldpoint controllers to the more modern and capable NI Compact Rio controllers. Software for the tower, which had previously been contracted and developed externally, was completely reconstructed, providing improved system reliability, stability, and flexibility for modifications. In addition, temperature, relative humidity, and barometric pressure sensors were added to every level on the tower yielding a more complete measurement system (Figure 1.1.1). Upgrades to the 200 m tower became the catalyst for increased research, including research contracts with Alstom and the establishment of the Scaled Wind Farm Technology facility, while daily maintenance efforts continue.

Figure 1.1.1. Collection of TTU 200 m tower hardware and software upgrades.

1.1.2. The TTUKa Research Radars.

These TTUKa research radar systems were designed primarily for the initial purpose of investigating fine scale temporal and spatial atmospheric motions and their impact through the use of both single and dual-Doppler rapid deployment strategies. In order to accomplish these goals, both high spatial resolution and system sensitivity were critical design criteria. Table 1.1.2. summarizes the various milestones achieved throughout the duration of the project build.

The completion and testing of the first radar system in its initial configuration provided proof of concept, proved viability of the overall system design and formed the basis for future comparative testing between the two systems. The major digital signal processor upgrade immediately doubled the range resolution of both systems due to software enhancements made possible within the new architecture that allowed for chaining of the digital filter pairs. In addition, this upgrade also increased overall system sensitivity an additional 15dB through enhancements in the technology of the new IF digitizer. Additional improvements were accomplished in reducing the system noise floor by discrete adjustments within the analog block up/down conversion stages.

Table 1.1.2. Timeline of TTUKa Technological Advancements.

Spring 2008	Last component for first radar arrived; transmitter and differential circulator testing complete.
June 2009	First radar completed. TWTA helix final driver stage redesign/rebuild.
July 2009	Pulse compression formulation/testing began.
Spring 2010	Second radar completed.
July 2011	Major DSP upgrade increased dynamic range by 15dB, increasing range resolution from 32 m to 15 m by software chaining of digital filter compute cycles.
August 2011	Reduced LNA noise figure, both systems.
May 2012	Pulse compression refinement for wind farm work began.
August 2012	Major antenna upgrade began.
February 2013	Achieved 9 m range gate resolution across all conventional pulses and 12µs compressed pulse by software remapping of DSP compute cycle.
May 2013	Mitigated ground target azimuthal smearing by implementation of real-time spectral filter.
June 2013	TTUKa1 antenna/receiver chain upgrades completed. Antenna gain now 54.5dB, half-power beamwidth 0.33º. Receiver noise floor -97.5dBm for 20µs compressed pulse.
July 2013	Mitigated turbine radial interference issues via spectral clutter filtering and post processing enhancements.
August 2013	TTUKa2 antenna/receiver chain upgrades completed.
September 2013	Final tuning of both receiver chain up/down conversion units in order to match performance of the two radar systems.

Experimentation with the reformulation of the pulse compression digital filter conversion chains was critical for optimization of performance. A comparison of a poorly formulated pulse compression burst pulse, Figure 1.1.2a, with a well formulated pulse compression burst pulse, Figure 1.1.2b outer plot, are shown in the spectral response plots below. For each plot, the horizontal axis indicates frequency, although the scale has been expanded 10:1 in Figure 1.1.2b as compared to Figure 1.1.2a. The vertical axis in both plots indicates amplitude in -10dB steps per major division with 0dB noted in yellow. In addition, the inner plot of Figure 1.1.2b indicates the digital pulse compression filter response which was engineered to capture and pass approximately 99.84% of the main lobe analog burst pulse envelope forward into the digital signal processor.

Several points of interest can be found in direct comparison of the two spectral response plots. First, the first sidelobe levels as compared to the peak amplitude of each waveform are of interest. In Figure 1.1.2a, the first sidelobe is only approximately 16dB down from the peak, whereas in Figure 1.1.2b, the first sidelobe level (outer waveform) is located over 35dB down from the peak. Next, the passband response of the main lobe is attenuated approximately 2.5dB (peak downward shift below the yellow 0dB line) in Figure 1.1.2a, as compared to no peak amplitude attenuation in Figure 1.1.2b. Also of interest are the large number of sidelobe peaks and the slowly decaying amplitude roll off in Figure 1.1.2a, as compared to Figure 1.1.2b, recalling that Figure 1.1.2b is expanded on a 10:1 scale in the horizontal. Finally, the extended and almost completely flat main lobe envelope with steep dropoff in Figure 1.1.2b, which lends itself much more readily to almost complete digital conversion, is beneficial.

Each of these factors critically influence target range-time sidelobe artifacts, point target discrimination, and distributed target sensitivity.

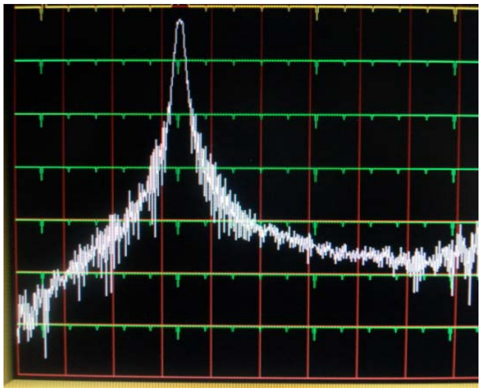

Figure 1.1.2a. Poorly Formed PC Burst.

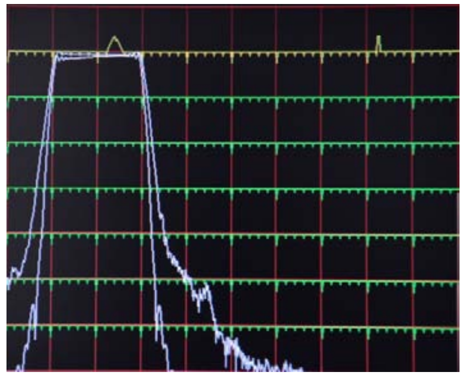

Figure 1.1.2b. Well Formed PC Burst.

The cassegrain reflector upgrade significantly improved overall system performance and sensitivity. The increase in parabolic reflector gain from 50.8dB to 55.9dB was leveraged to further reduce the down conversion system gain, resulting in an overall reduction of the system noise floor across each pulse width, while simultaneously increasing the dynamic range an additional 6dB. In addition, the 1km downrange azimuthal resolution was increased from 8.55 m to 5.76 m by narrowing the 3dB beamwidth from 0.49° to 0.33°.

The TTUKa radars have served a multitude of research projects at TTU. For the purposes of this award, the usage of the radars to benefit the wind energy community is documented in the summary for Subtask 1.2 contained in this report.

1.1.3. The West Texas Mesonet.

The West Texas Mesonet (WTM) is an independent project collaborating with the Atmospheric Science Group under the NWI at TTU. The first WTM station came online at Reese Center, 12 miles west of Lubbock, in June of 2000. Since that time, our network has grown to 79 mesonet stations and six boundary layer SODAR units covering 54 counties (see Figure 1.1.3.1) in the Texas Panhandle, South Plains, Rolling Plains, Permian Basin, Trans Pecos, Concho Valley, Big Country, Edwards Plateau, Hill Country and eastern New Mexico. Our mission is to provide accurate meteorological data for distribution to a variety of facets in our region including operational meteorology, wind energy interests, agriculture and farming, research, and media.

Each WTM station sends real-time meteorological data back to Reese Center every one-to-five minutes and agricultural data every fifteen minutes. All stations are nearly identical in configuration and sensors (see Figure 1.1.3.2) with the following data parameters sent in real-time:

- 10 meter Wind Speed and Direction
- 9 meter Temperature
- 20 ft Wind Speed
- 2 meter Wind Speed
- 2 meter Solar Radiation
- 2 meter Temperature
- 1.5 meter Temperature/Relative Humidity/Dewpoint
- Barometric Pressure (Sea-level pressure and Altimeter)
- Precipitation
- Leaf Wetness
- Soil Temperature at five-levels
- Soil Moisture at four-levels

Beyond providing consistent maintenance, the West Texas Mesonet has installed 31 new regional near-surface stations and six boundary layer SODAR units across West Texas and eastern New Mexico (see Figure 1.1.3.3) with the assistance of the DOE award. SODAR's (Sound Detection and Ranging) are acoustic devices for the measurement of three-dimensional wind speed and direction and turbulence characteristics of the atmospheric boundary layer (lowest 1200 feet). The purpose of the WTM SODARs are to obtain real-time wind speed and direction data with height to study the impact of low-level jet phenomena on wind turbine farms and other wind power interests across the southern High Plains. Each SODAR unit was also located on/near airports *(*see Figure 1.1.3.4*)* to help aviation interests warn aircraft of low-level wind shear. Every WTM station and SODAR installation is a partnership (see Table 1.1.3.1) with a collaborating city, county, private landowner, federal or state agency. In most cases, these groups help offset communication costs. Real-time data from the WTM are provided free of charge to any individual or group. We strive to meet the highest standards for the collection and dissemination of weather and agricultural information.

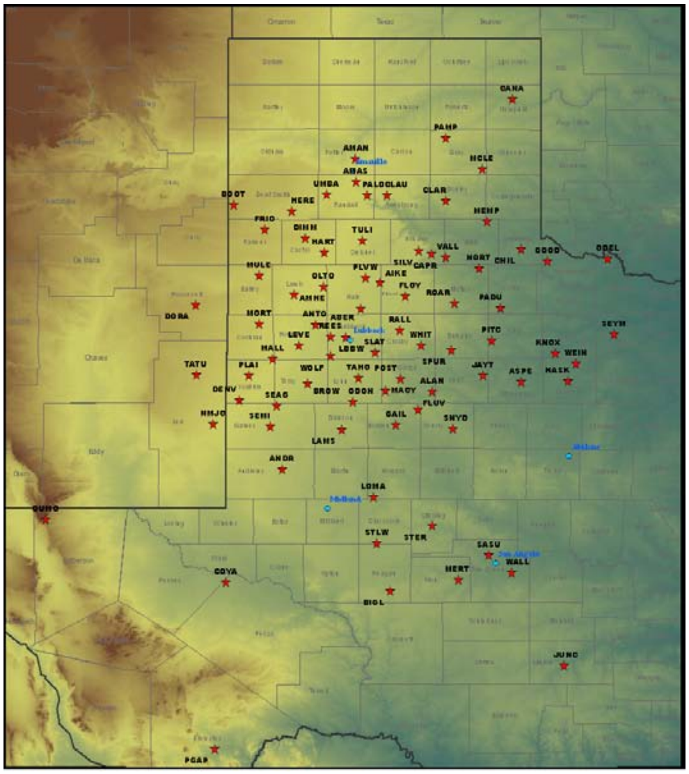

Figure 1.1.3.1. Map of West Texas Mesonet Stations through October 1st, 2013.

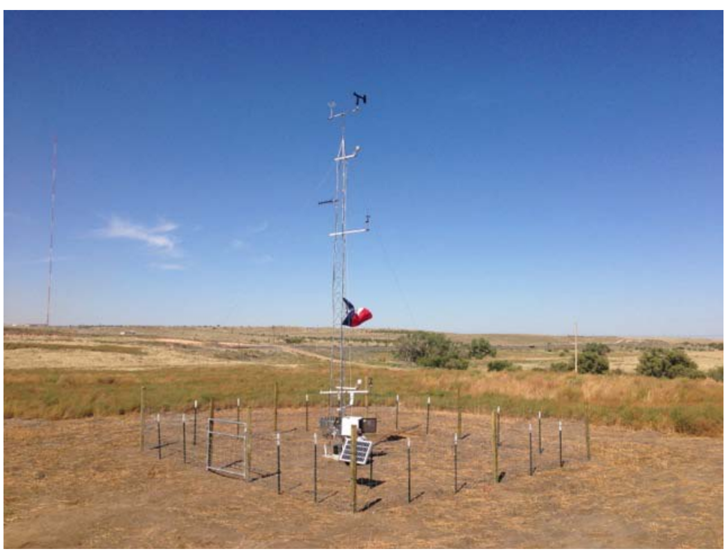

Figure 1.1.3.2. Photograph of the Amarillo North West Texas Mesonet station in September 2013.

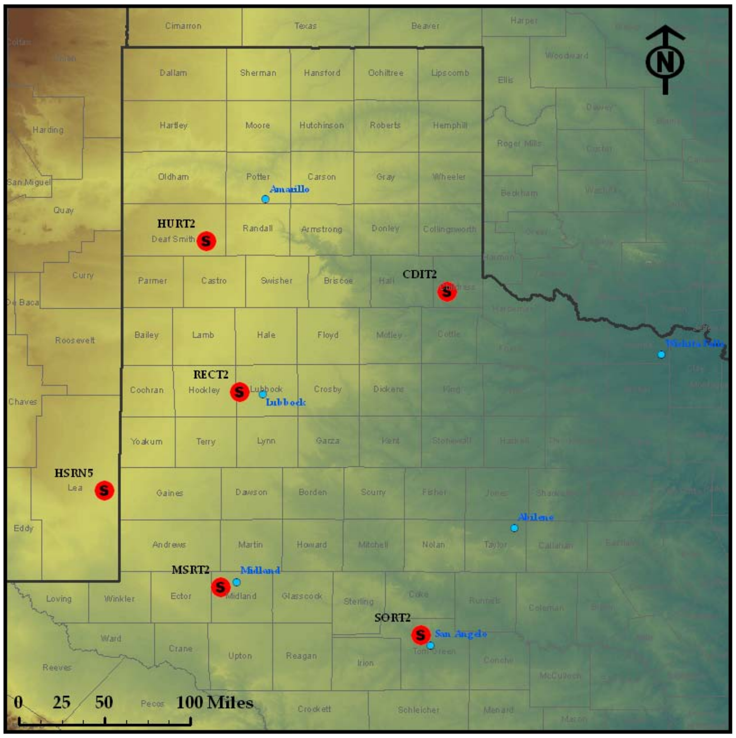

Figure 1.1.3.3. Map of existing West Texas Mesonet SODAR locations through October 1st, 2013.

Figure 1.1.3.4. Photograph of the Midland SODAR (MSRT2) located on the main runway at Midland International Airport.

Table 1.1.3.1. List of Collaborating Organizations for West Texas Mesonet stations and SODAR installations during period of DOE CDP Project 2006-2013.

Mesonet Station (Name/#)	Organization	Completion Date
Turkey 2WSW (#49)	Valley ISD/Hall County EM/City of Turkey	September 2006
Childress 2NNE (#50)	Childress County EM/City of Childress	February 2007
Tatum NM 2SW (#51)	Tatum ISD/National Weather Service Midland	October 2007
Northfield 1S (#52)	Simpson Ranch/National Weather Service Lubbock	February 2008
Dora NM 2SW (#53)	Dora ISD/Roosevelt County Volunteer Fire Dept.	March 2008
San Angelo 7NW (#54)	Angelo State University	October 2008
St. Lawrence 5SW (#55)	Braden Ranch and Glasscock County EM	January 2009
Haskell 1NW (#56)	Rolling Plains Groundwater Conservation District	May 2009
Wall 1E (#57)	Wall Cooperative Gin	November 2009
Seymour 3NW (#58)	Rolling Plains Groundwater Conservation District	November 2009
Knox City 3NW (#59)	Rolling Plains GCD/USDA	March 2010
Pine Springs (#60)	National Park Service/National Weather Service	September 2010
Quitaque 3NNW (#61)	Caprock Canyons State Park/Texas Parks & Wildlife	December 2010
Odell 4ENE (#62)	City of Vernon	May 2011
Coyanosa 2N (#63)	Coyanosa Cooperative Gin	May 2011
Big Lake 1WNW (#64)	Santa Rosa Water Conservation District	June 2011
Junction 1SSW (#65)	Texas Tech University Junction	January 2012
Hobbs NM 5NW (#66)	New Mexico Junior College	March 2012
Canadian 6E (#67)	Texas Parks & Wildlife	June 2012
Canyon 13E (#68)	Palo Duro Canyon State Park/ Texas Parks & Wildlife	September 2012
Bootleg 11WNW (#69)	Hereford and Bootleg Volunteer Fire Dept.	November 2012
Sterling City 4W (#70)	Sterling County Underground Water Cons. District	November 2012
Mertzon 3NNE (#71)	Irion Co. Underground Water Conservation District	February 2013
Persimmon Gap (#72)	Big Bend National Park/National Weather Service	March 2013
Weinert 2NNE (#73)	Rolling Plains Groundwater Conservation District	April 2013
Claude 12SW (#74)	Armstrong County Emergency Management	April 2013
Amarillo 7SSE (#75)	City of Amarillo	June 2013
Umbarger 3NNE (#76)	City of Amarillo	August 2013
Lomax 1SSE (#77)	Lomax Cooperative Gin	September 2013
Amarillo 9NNE (#78)	City of Amarillo	September 2013
Aiken 3WSW (#79)	High Plains Underground Water Dist./TAWC	Under Construction

SODAR (Name/#)	Organization	Completion Date
Hereford (HURT2/#1)	City of Hereford and Hereford Municipal Airport	October 2011
Reese (RECT2/#2)	Texas Tech University	February 2012
San Angelo (SORT2/#3)	Angelo State University	March 2012
Hobbs (HSRN5/#4)	New Mexico Junior College	April 2012
Midland (MSRT2/#5)	City of Midland/Midland International Airport	February 2013
Childress (CDIT2/#6)	City and County of Childress	May 2013

Subtask 1.2: Use the TTUKa Radars to Attempt High-Resolution Measurements of Wind Flow Structure in Weather Events Common to the Great Plains and Turbine Wakes.

1.2.1. Wind Turbine Wakes and Wind Farm Complex Flows.

Beginning the Fall 2011, the TTUKa radars have been successfully utilized to document wind flows relevant to wind energy applications. Multiple short-duration field campaigns were executed following a systematic data collection methodology. Initially TTU focused on documenting the wake of a single utility-scale turbine, but the team quickly built towards the collection of complex flows measurements from multiple wind farms. The result of this work was the construction of multiple peer-reviewed publications, submission of two patents, delivery of multiple several conference presentations, and generation of significant industry collaboration.

1.2.1.1. Introduction.

Optimizing new and existing wind farms requires enhanced knowledge of the complex flow fields that exist within and surrounding them. Existing models fail to accurately describe the flow through wind farms, in particular the impact of turbine wakes, which contributes to an estimated 10-20% underperformance of expected wind farm efficiency (Barthelmie et al. 2010, Barthelmie and Jenson 2010, Schepers et al. 2012). Poor understanding of the modulated flows through wind farms leads to uncertainty in optimizing wind farm design and layout as well, including individual turbine spacing (Meyers and Meneveau 2012, Chowdbury et al. 2012). The need for comprehensive full-scale measurements from within wind farms is well advertised by the wake modeling community to validate and improve current model schemes (Barthelmie et al. 2007, 2009, 2013, Mckay et al., 2013, Gaumond et al. 2013), including wake behavior in complex terrain (Politis et al. 2012).

To date, full-scale wind flow observations through wind farms are exceedingly limited both in quantity and spatial coverage. Point measurements collected by meteorological towers and turbine Supervisory Control and Data Acquisition (SCADA) systems generally represent isolated observations averaged over 10-minute intervals (Barthelmie et al. 2007, Barthelmie et al. 2009, Schepers et al. 2012). Wake deficits and structure can only be assessed with these measurements for limited wind direction regimes, limited downwind distances, and limited horizontal and vertical extents. Scanning Light Detection And Ranging (LIDAR) technologies can provide two-dimensional horizontal and vertical data fields, but current technologies offer a limited maximum range of only a few kilometers and published wake studies using LIDAR have only been focused on wakes from single turbines (Käsler et al. 2010, Bingöl et al. 2010, Trujillo et al. 2011, Iungo et al. 2013, Smalikho et al. 2013). LIDAR also offers much slower scanning/revisit times than what advanced radar technologies can already provide.

The TTUKa radars have been designed to document fine-scale boundary layer flows when compared to traditional Doppler radar technologies. This differentiation allows for the assessment of the wind flows important for wind farm performance, including the structure and evolution of turbine wakes, with a much larger footprint and higher spatial and temporal resolution than can be provided by any other existing remote sensing technology. The use of innovative single- and dual-Doppler scanning techniques yields data analysis products that can serve a diverse range of wind energy interests.

1.2.1.2. Results and Discussion.

The first successful single-Doppler measurements of a single utility-scale turbine wake were made in the Fall of 2011 west of Lubbock, TX. These measurements led to the development of the first ever publication utilizing Doppler radar to resolve fine-scale flows relevant for wind energy (Hirth et al. 2012). Using single-Doppler line of site measurements, a single turbine wake was documented to exceed 30 rotor diameters in distance, emphasizing the significant observational footprint Doppler radar provides over other available remote sensing technologies used for turbine wake detection (Kasler et al. 2010, Iungo et al. 2013). The ability to capture horizontal (Figure 1.2.1.1) and vertical slices (Figure 1.2.1.2) through a wake to assess velocity deficits and associated wake turbulence were highlighted. The TTUKa radars are able to scan horizontal and/or vertical sectors with revisit times of only a few seconds, allowing for the rapid assessment of evolving wake structure and tracking of turbulent eddies (using spectrum width) associated with the wake.

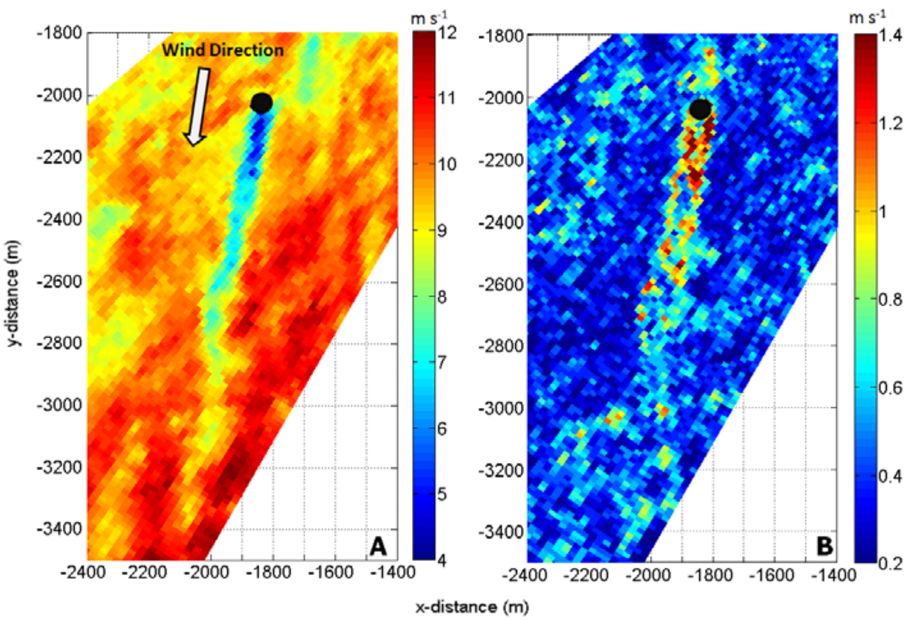

Figure 1.2.1.1. Horizontal PPI single-Doppler (A) radial velocity (m s^{-1}) and (B) spectrum width (m s^{-1}) showing the wake downstream of a single utility scale turbine. (Adapted from Hirth et al. 2012.)

The first ever dual-Doppler dataset of a single turbine wake was analyzed and submitted in the Spring of 2012 (Hirth and Schroeder 2013). Coordinated data collection was conducted by two radars utilizing volumetric scanning. The employed scanning strategies allowed for the synthesis of the actual horizontal wind speed and direction over a three-dimensional domain. Wake structure and evolution was assessed every 45-seconds for nearly a continuous hour period. Abrupt changes in wind speed and direction during the analysis period were related to significant changes in wake structure (Figure 1.2.1.3). The dual-Doppler wind fields also allowed for the assessment of wake deficits through the width and depth of the rotor sweep. To do this, a wake tracking algorithm was developed and applied to each dual-Doppler volume. Average and maximum wake deficits were assessed at various downwind distances for each volume (Figure 1.2.1.4). Composite deficits over the data collection period were constructed and related to power output deficits that would be experienced by a hypothetical turbine residing in the wake. The dual-Doppler wind fields were also merged with the turbine data, as the dual-

Doppler wind field upstream of the turbine was used to project the turbine power output. The projected power output over the hour period was found to be within 0.1% of the actual turbine power output over that period.

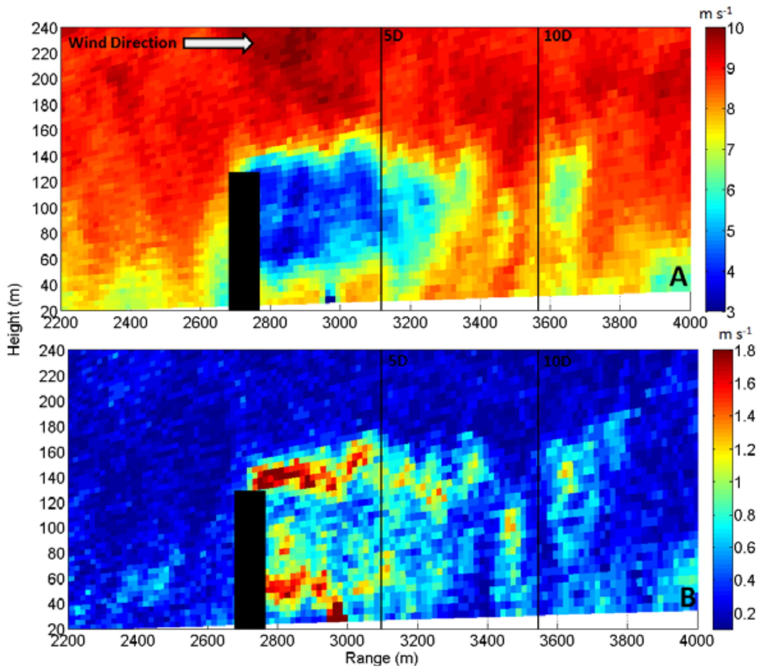

Figure 1.2.1.2. Same as Figure 1.2.1.1, but for a vertical RHI radar scan.

These single turbine datasets provided the proof-of-concept and validation for taking the radar systems to collected measurements within large turbine arrays. A small field campaign was conducted in the Spring and Summer of 2012 where multiple wind plants were visited throughout West Texas and various scanning strategies were employed. A tremendous knowledge base was obtained during these efforts, including an improved understanding of how to coordinate and scout deployments and what scanning techniques were most effective. The first successful single-Doppler TTUKa measurements of a large turbine array were collected on May 8, 2012 over a scanning sector containing roughly 70 utility scale turbines (Figure 1.2.1.5). This data set revealed tremendous information about wind farm complex flows structure, including turbine-to-turbine interaction, wake behavior, and the impact of transient gust and lull features traversing the wind farm. Additional single-Doppler datasets were collected documenting the impact of complex terrain and abrupt wind shifts (e.g. thunderstorm outflows).

A monumental dataset was collected on June 6, 2012 utilizing both TTUKa radars to acquire the first ever dual-Doppler dataset within a large turbine array containing 36 turbines. This dataset captured a wide variety of complex flows measurements including wake evolution, turbine-to-turbine interaction, high-momentum channels between individual wakes, the impact of complex terrain, and wind farm edge effects (Figure 1.2.1.6). A publication associated with this work has been constructed and is currently in press (Hirth et al. 2014). Radar derived wind maps were merged with wind turbine data to validate the dual-Doppler wind fields and construct a site specific power curve. The radar derived power curve and associated wind field measurements were used to accurately project the power output for 29 turbines over a 100 minute period. Wake structure was also assessed looking at comparisons in turbine inflow using vertical cross-sections through portions of the analysis domain (Figure 1.2.1.7). This dataset highlights the tremendous potential the TTUKa radar systems have in advancing the wind energy industry. Radar measurements could be used to assist industry needs spanning resource assessment, wake modeling and wind farm layout, wind farm maintenance, and inputs for advanced controls systems.

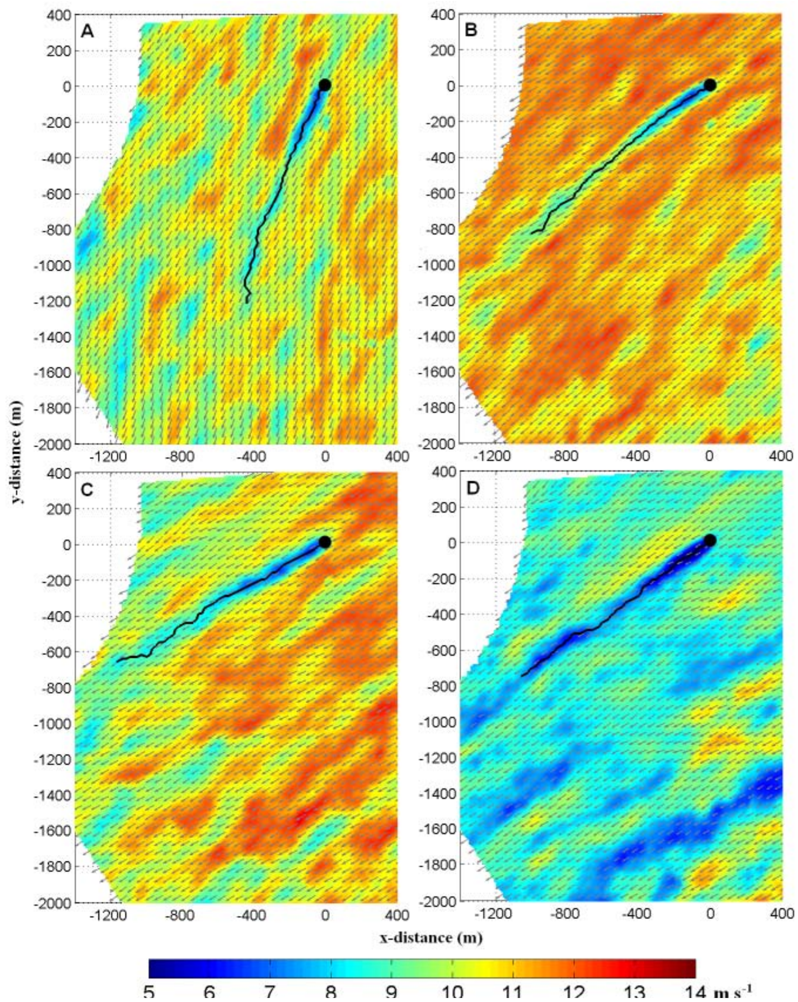

Figure 1.2.1.3. TTUKa dual-Doppler -synthesized horizontal wind speed (m s^{-1}) on 27 Oct 2011 at 80 m AGL at (a) 1233, (b) 1241, (c) 1304, and (d) 1317 UTC. Horizontal wind vectors are shown. The black dot represents the location of the turbine. (Adapted from Hirth and Schroeder 2013.)

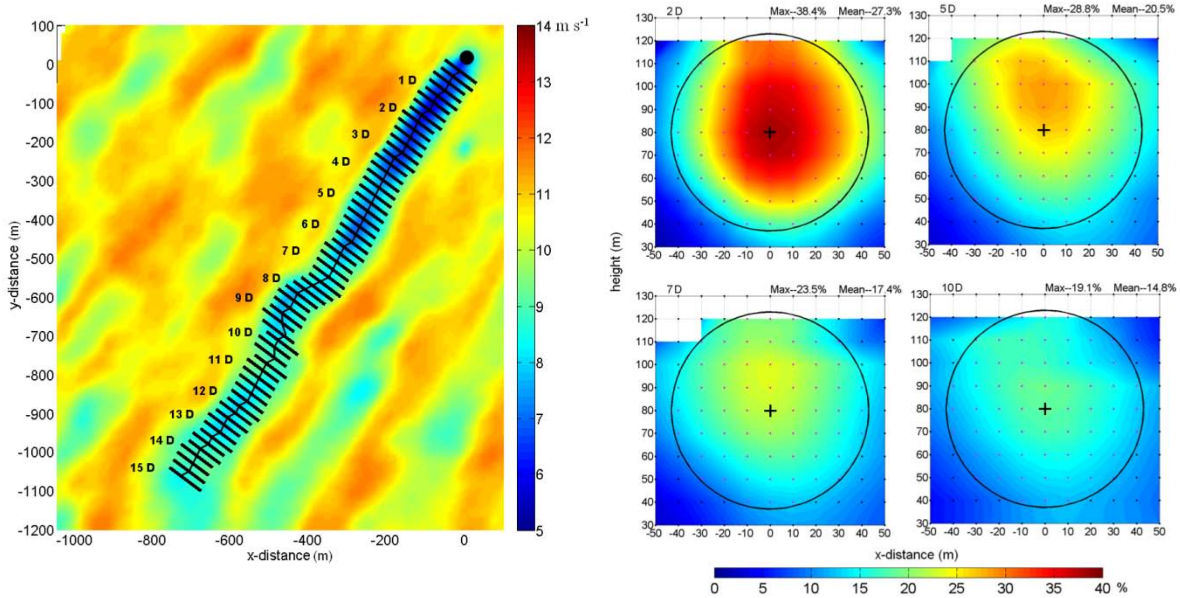

Figure 1.2.1.4. Example of the employed wake tracking algorithm and composite mean and maximum wake deficits at various downwind distances. (Adapted from Hirth and Schroeder 2013.)

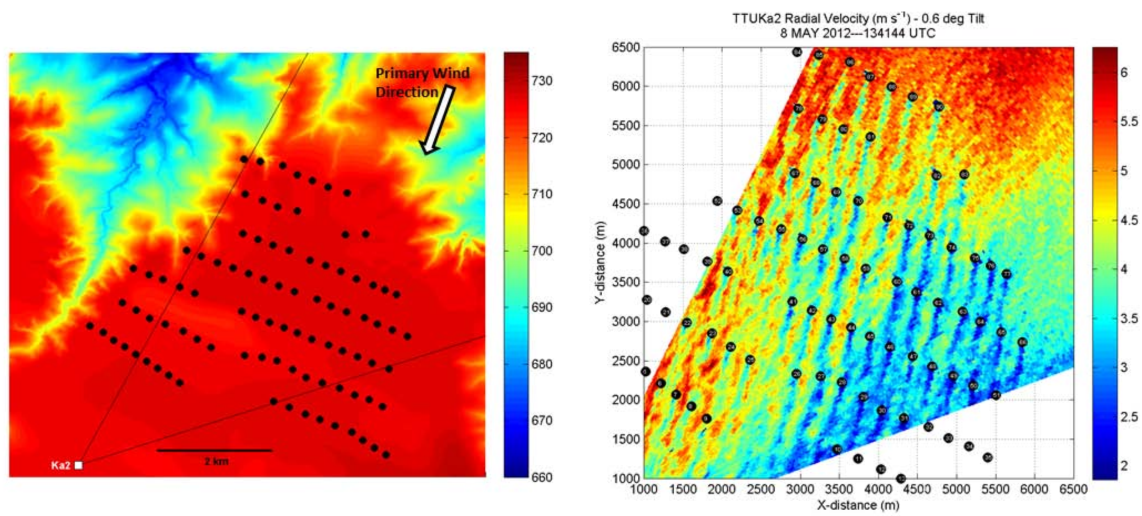

Figure 1.2.1.5. (Left) Schematic of a TTUKa deployment within a wind farm and (Right) single-Doppler radial velocity (m s^{-1}) showing multiple turbine wakes and turbine-to-turbine interaction.

1.2.1.3. Conclusions.

The NWI at TTU has pioneered the usage of radar technology and techniques in the wind energy community. As a result, two patents are currently being converted, and new measurements are revolutionizing our understanding of the complex flows found within wind farms. The constructed publications and podium presentations given at multiple domestic and international conferences have fostered widespread industry interest into the TTUKa radar capabilities, including the development and execution of multiple research and service contracts.

Using single-Doppler scanning methods, fast evolving wake structure can be assessed every few seconds, providing tremendous information about the nature of wake spreading and meandering, as well as the tracking of turbulent eddies as they propagate downwind into successive turbines. Dual-Doppler techniques allow for the construction of a three-dimensional domain of the horizontal wind fields roughly every minute. These wind fields can be used to construct vertical wind profiles, assess turbine inflow across the entire rotor sweep, generate turbine and wind farm power curves and project wind farm power output, assess the impact of local terrain, and provide wind maps for use in resource assessment. When coupling Doppler radar wind measurements with available turbine power performance data, complex flows can be related to the expected power output deficits for multiple turbines located within various portions of a wind farm.

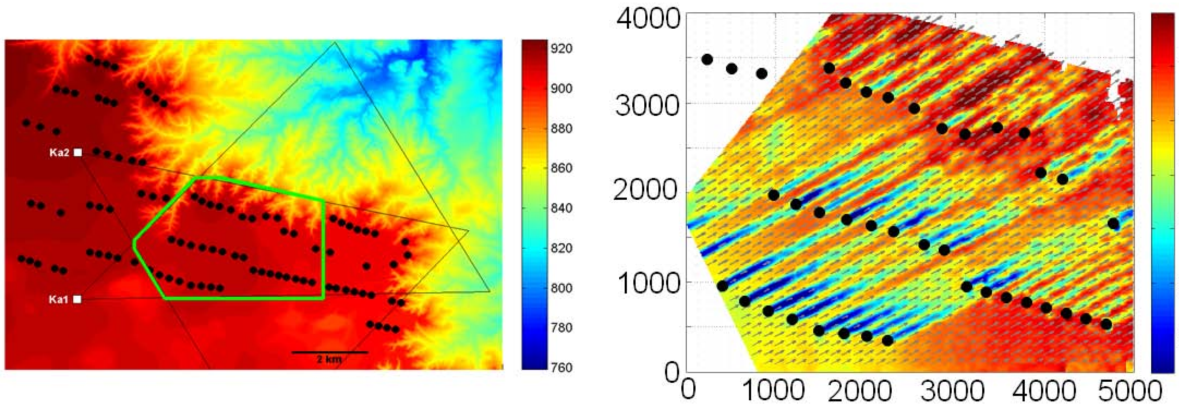

Figure 1.2.1.6. (Left) Schematic of a TTUKa dual-Doppler deployment within a wind farm and (Right) dual-Doppler radial velocity (m s^{-1}) showing various wind farm complex flows features. (Adapted from Hirth et al. 2013.)

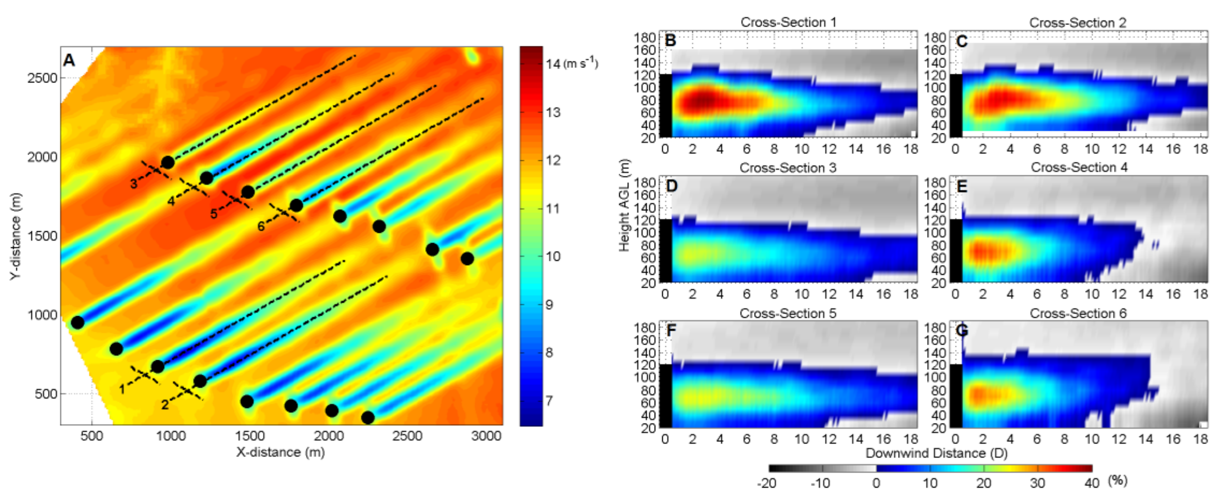

Figure 1.2.1.7. (A) Ten-minute composite DD wind speed at hub height (80 m) from 1559 – 1609 UTC (Volumes 24-34) on 6 June 2012 overlayed by six vertical cross-section reference lines. Ten-minute composite vertical cross-sections (B) 1, (C) 2, (D) 3, (E) 4, (F) 5, and (G) 6 are shown, represented as a wind speed percent difference from the wind profile 1 D upstream of each turbine. (Adapted from Hirth et al. 2013.)

The measurements acquired in this project represent the first known dual-Doppler synthesized wind fields describing the complex flows around a single turbine, and within and surrounding a wind farm. In particular, turbine wake structure and evolution is documented, including turbine-to-turbine interaction. Wake structure is found to be modulated by transient gust/lull features and complex terrain. Channels of higher momentum are found between individual wakes when the wind direction is oriented perpendicular to a row of turbines. These channels represent a wind speed excess through the depth of the rotor sweep from what is found upstream of the wind farm, and a potential source of additional power output that is not captured by current wind farm operations procedures. Real-time dual-Doppler wind maps can be used to provide situational awareness to large turbine arrays to more effectively anticipate the impact of rapidly changing wind conditions (e.g. wind ramp events). Within the farm, these same wind maps can feed individual turbine and wind farm control systems to potentially steer turbine wakes and mitigate the known large power output deficits that result from current turbine-to-turbine interactions.

Measurements such as those provided in this study can also be incorporated into wake modeling efforts to improve expected power output projections for a given wind farm. More accurate numerical representations of wake spreading and meandering can be constructed, as well as the inclusion of the high wind speed channels between wakes that have been documented in multiple TTUKa radar measurement campaigns. A more realistic depiction of wake structure and behaviour can then be used to improve turbine layout methods, including a better understanding of appropriate turbine spacing and turbine row orientation.

In the absence of turbines, these same data collection and analyses methodologies can be used to aid resource assessment and to improve the understanding of local terrain effects. Rather than relying on point tower measurements or vertically pointing “virtual” meteorological towers currently provided by some LIDAR systems, three-dimensional wind maps over the entire footprint of a potential wind farm yield a much more comprehensive and continuous understanding of the local wind behaviour for a specific site. The data collected in this study have repeatedly shown the Doppler radar velocity measurements to match well with existing anemometry from both fixed towers and turbine nacelles.

Future work will likely focus on constructing a catalog of wind farm complex flows data collected by the TTUKa radars from a wide variety of wind farms to assess similarities and differences based on wind farm layout, turbine type, local terrain and roughness, and atmospheric conditions. The impact of adjusting first-order turbine controls will also be evaluated to assess the impact of changing turbine operation (yaw, pitch, etc.) on turbine-to-turbine interaction and overall wind farm performance. The presented advanced scanning Doppler radar technology, data collection strategies and analyses methods carry significant potential to improve wind farm optimization by providing comprehensive measurements of the complex flows within and surrounding them.

1.2.2. Complex Flow Measurements from Thunderstorm Outflows.

1.2.2.1. Introduction.

Instrumented towers are typically used to collect wind profile data, but their use is restricted by infeasibilities related to tower heights and locations. These limitations have spurred the development and use of remote sensing instruments in evaluating the vertical structure of wind. Mobile Doppler radars in particular possess a unique advantage in collecting data within rare, design-relevant atmospheric phenomena. A single Doppler radar can only resolve line of sight velocities, while data from two Doppler radars can be synthesized to obtain the full wind vector. Methods have been developed to obtain a wind profile from both single-Doppler and dual-Doppler volumes. These methods, which are all based on collecting horizontal plan position indicator (PPI; constant elevation, multiple azimuths) scans at multiple elevation angles, lack the temporal and spatial resolution necessary to resolve fine-scale features in the wind profile. In addition to PPIs, most radars are able to scan multiple elevation angles along a single azimuth, referred to as a Range-Height Indicator (RHI) scan. If two radars perform RHIs along azimuths separated by approximately 90 degrees, then the intersection of the coordinated RHI planes represents a vertical set of points where dual-Doppler wind syntheses are possible and wind speed and direction profiles can be retrieved. A similar method was previously used with two coherent Doppler lidars (Calhoun et al. 2006), but only a limited comparison was performed with other remotely sensed data. Using a similar technical approach, the objective of this research is to validate profiles estimated with coordinated RHIs through comparisons with wind profile data from anemometers on a 200 m instrumented tower. As very few comparisons of dual-Doppler data with data from anemometers exist in the literature, this research also provides an opportunity to compare the mean and turbulent characteristics of remotely sensed volumetric data and point measurement data from anemometers.

1.2.2.1.a. Instrumentation.

Radar data were collected using the TTUKa mobile Doppler radars (Weiss et al. 2009; Hirth et al. 2012). These mobile Doppler radars are capable of high spatial and temporal resolution with 15 m range-gate spacing and a 0.49° half-power beam width (prior to an upgrade in late summer 2012). Additionally, RHI scans are performed with a 0.1° angular resolution leading to oversampling in elevation. The implementation of a pulse compression technique combines the sensitivity achieved using a relatively long pulse without sacrificing range resolution. One consequence of transmitting within the Ka band is the tendency of the signal to attenuate in regions of higher precipitation. This effect was seen during data collection for the present study and occasionally resulted in brief data voids.

Both TTUKa radars were deployed to the NWI field site at Reese Technology Center (RTC) in Lubbock, TX. This site maintains several instruments that can be used to assess the local wind profile and provide comparisons to the wind profiles estimated from the coordinated RHIs. This study will focus on the 50Hz data collected by UVW anemometers at 8 different levels of a 200 m tall tower. The tower is surrounded by flat terrain characterized by roughness lengths between 0.009 and 0.01 m and populated by few obstructions. Instrumentation is mounted along boom arms extending 4.26 m from the center of the tower and oriented to the northeast (300 degrees). The tower incorporates both UVW and sonic anemometers which are mounted 3.65 m and 4.26 m from the tower respectively. However, poor quality of the sonic data in several events precluded use of the data for the validation. Though the instrumentation configuration and lack of standard cup anemometry currently prevents IEC certification, the 200 m tower still provides robust data for comparison to other platforms.

1.2.2.1.b. Validation Dataset Descriptions.

A total of five validation datasets were acquired at the NWI field site for comparison. Atmospheric conditions varied considerably for each dataset. Four datasets were collected in precipitating environments, while one dataset was collected in a non-precipitating environment (or clear air). This variety also yielded comparisons at a wide range of wind speeds. Additionally, the intersection point of the RHIs and the resulting distance of each radar from the intersection point varied with each deployment (Table 1.2.2.1). A typical radar scanning strategy for data collection consisted of RHIs being performed from 0 - 45 ° and PPIs intermittently included. However, the scanning strategy was altered for both the 4 June 2012 and the 28 June 2013 deployment in order to improve the temporal resolution of the radar data. This improvement was accomplished by eliminating PPIs from the scanning strategy and limiting RHIs to 6° in elevation. This elevation angle ensured that data were collected in the lowest 200 m by both radars for comparison to the tower.

Table 1.2.2.1. Deployment characteristics from each event described in the text.

Date of Event	Separation between RHI Intersection and Tower (m)	Distance to RHI Intersection from Ka1 / Ka2 (m)	Event Type
12/05/2011	263.72	1650 / 1740	Stratiform precipitation
03/19/2012	304.52	2880 / 2700	Weak dryline convection
06/04/2012	390.54	2880 / 2595	Thunderstorm outflow
06/15/2012	113.88	2925 / 2880	Thunderstorm outflow
06/28/2013	192.94	2724 / 2911	Clear air

1.2.2.1.c. Data Processing and Quality Control.

The analysis of a given radar dataset begins by isolating the time periods of data fit for analysis. This process involves not only lining up the data from both radars temporally, but also considering sections of data rendered unusable by second-trip echoes, incoherencies, or attenuation. Once select portions of the dataset are identified, quality control procedures are implemented. These include heading verification via Unidata's Integrated Data Viewer, unfolding radial velocities that exceeded the Nyquist velocity, and correcting radar "jitter." The latter is a phenomenon caused by hysteresis in the vertical offset of successive RHIs by approximately 0.5°. The correction of the radar jitter results in some data loss below the 0.5° elevation. The intersection point of the RHIs and the distance between each radar and the intersection point are computed using the latitude, longitude, and north-relative RHI angles (based on the corrected radar heading) of the radars. The radial velocity data located at the intersection point are then separated into height bins spanning 20 m in the vertical. The height of each bin is then assigned as the mean height of the observations contributing to the bin. This is necessary to account for differences in the elevation angles of the RHIs. For elevation angles greater than 0°, the vertical component of the radial velocity is removed. The binned radial velocity profiles are then synthesized to obtain dual-Doppler wind speed and direction profiles. Wind speed and direction data from the 200 m tower required significantly less quality control. Data were examined for erroneous values (spikes, dropouts, etc.) which were subsequently removed.

1.2.2.2. Results and Discussion.

1.2.2.2.a. Wind Speed and Direction Results.

The event mean profiles in Figure 1.2.2.1 illustrate that the dual-Doppler wind speeds generally match those of the tower. Comparing the wind speed magnitudes of the profiles from each event, it can be seen that the mean near-surface (5 m) dual-Doppler wind speeds were consistently greater than the 4 m UVW wind speeds. The magnitude of this difference between the two platforms varied for each event (Figure 1.2.2.2). The greatest difference between the 5 m dual-Doppler wind speeds and the 4 m UVW wind speeds was associated with the two outflow events (06/04 and 06/15) while the smallest differences were noted in the clear air and snow event (06/28 and 12/05). This suggests scatterer type and size may impact the dual-Doppler wind speed estimates near the surface. Above the surface, the trends vary by event with wind speed magnitudes of the two thunderstorm outflow events being overestimated by the dual-Doppler profiles through most of the depth of the profiles. Given the anemometer placement along the boom arm of the tower, it should be noted that the UVW anemometers are in the wake of the sonic anemometers for flows approximately parallel to the boom arm. This effect, along with the influence of the tower itself, could contribute to reduced UVW wind speeds values. The mean dual-Doppler wind direction profiles show very little deviation from the tower profiles in all events (not shown).

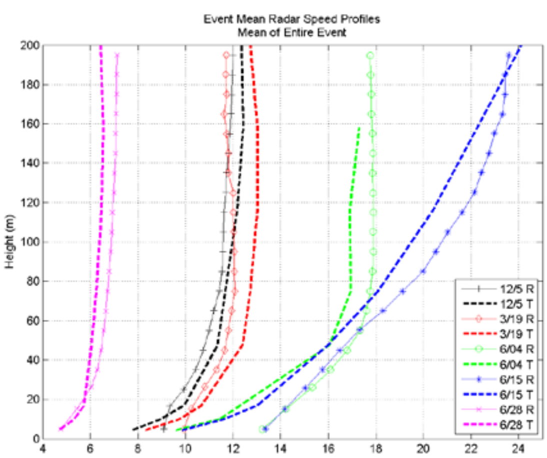

Figure 1.2.2.1. Comparison of mean dual-Doppler radar and UVW anemometer wind speeds for each event. "T" and "R" in the legend indicate "Tower" and "Radar" profiles respectively.

In addition to dual-Doppler wind profiles, this method also allows for the generation of dual-Doppler wind time histories. These time histories can be compared to UVW wind time histories at corresponding levels of the tower for cases when radar data were collected with adequate temporal resolution (e.g., 06/04 and 06/28). Using these time histories, various averaging times for both the dual-Doppler and the UVW data were also investigated. In general, the correlation between the tower wind speed and the dual-Doppler derived wind speed for each level increases with averaging time; r-squared values above 0.9 were noted for most levels using a 10 minute average.

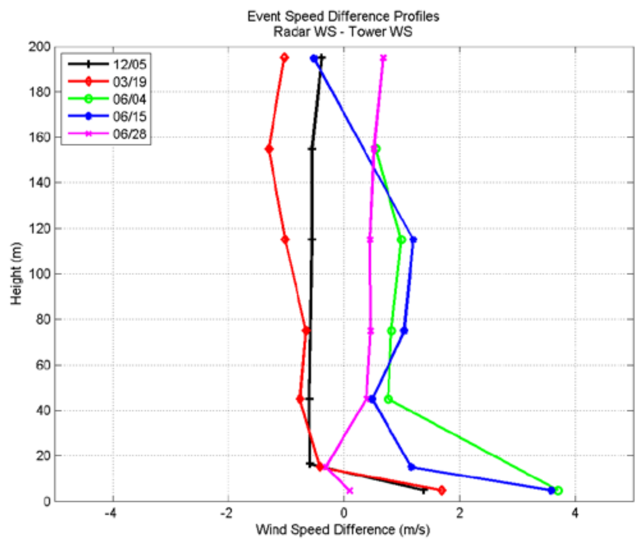

Figure 1.2.2.2. Wind speed difference profiles for each event. Difference computed as mean radar wind speed - mean tower wind speed for each level.

1.2.2.3.b. Turbulence.

The greater temporal resolution of the 4 June 2012 dataset allowed for the investigation of turbulence parameters. Turbulence intensity can be defined as a ratio between the root mean square and the mean wind speed. Running turbulence intensities (RTI) were derived with data from both platforms according to the method outlined in Holmes et al. (2007). This particular method incorporates a running mean into the computation of turbulence intensity to mitigate the effect non-stationarities in a wind speed time history. As in Holmes et al. (2007), a 40 second moving average is used for the running mean. The mean RTI for each level of radar and corresponding tower data was computed to produce a mean profile (Figure 1.2.2.3). The profiles indicate that the running turbulence intensities computed with the radar data are lower than those computed with the tower data. This effect is most likely due to the averaged properties inherent in the radar data. Smaller scales of turbulence are lost within the volumetric average of each radar bin. This effect is most pronounced near the surface where shear induced mechanical mixing is most prevalent and a greater portion of energy is distributed to smaller scales of turbulence. Above this near-surface layer, radar turbulence intensities are consistent with those of the tower.

To further investigate the ability of the radar to capture turbulence, power spectral density (PSD) estimates were computed for each level of the 200 m tower and compared to those at corresponding levels in the radar data. The time histories (over 2.5 hours in length) for each level of tower and radar data were divided into 10 minute segments. PSDs for each segment were averaged together to produce an average PSD for each corresponding tower and radar height. Near the surface, less energy is contained in the smaller scales measured by the radar as the radar spectra begin a substantial deviation from the tower spectra at approximately 0.009 Hz (Figure 1.2.2.4, left). Also, the lower Nyquist frequency further limits the resolution of the radar data to below 0.4 Hz. Farther above the surface, the spectra of the data radar show good agreement with those of the tower with the primary limiting factor of the radar data being the Nyquist frequency (Figure 1.2.2.4, right).

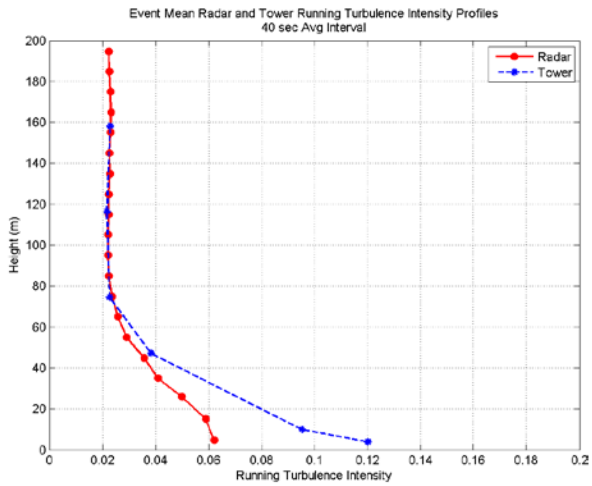

Figure 1.2.2.3. Running turbulence intensity profiles for the dual-Doppler radar and UVW tower data from the 4 June, 2012 dataset.

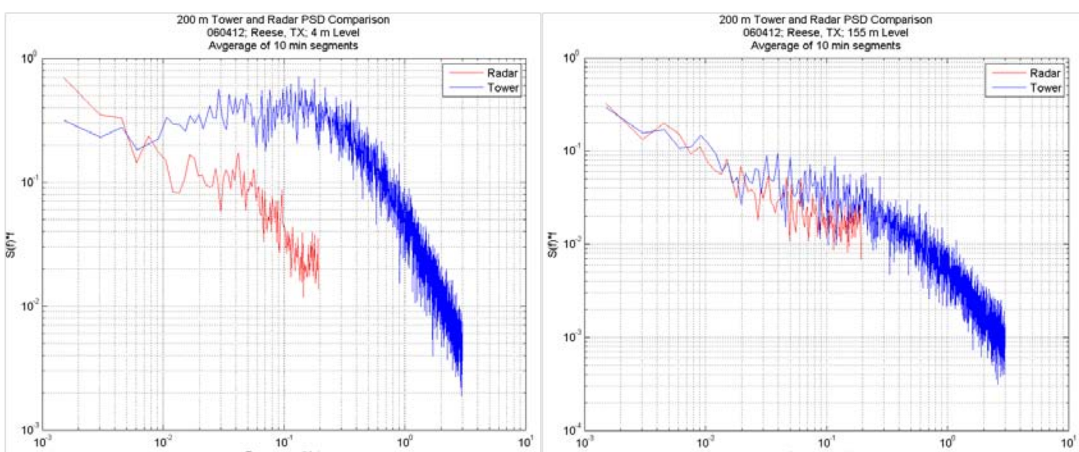

Figure 1.2.2.4. Power spectral density comparison for the dual-Doppler radar and UVW tower dataset from 4 June 2012 at the 5 m (left) and 155 m (right) levels.

1.2.2.3. Conclusions.

A new method was introduced in which coordinated RHIs from two high-resolution mobile Doppler radars were used to acquire dual-Doppler wind speed and direction profiles. This method was successfully verified in a comparison with data from UVW anemometers at multiple levels of a 200 m meteorological tower in multiple atmospheric conditions. Though mean wind speeds were slightly overestimated and turbulence was underestimated below elevations of 40 m, the results provide confidence for application of the coordinated RHI method at elevations above 40 m. The high temporal and spatial resolution of the TTUKa radar data allowed for the comparison of dual-Doppler and UVW time histories, which supported the trends seen in the profiles. Multiple effects can contribute to differences seen in the comparisons. Several of the datasets were acquired within thunderstorm outflows which are known to be highly non-stationary. As a result, small-scale features seen in the data of one platform may not be resolved in that of the other (given the separation distance between the measurement locations). Also, the instrumentation layout along the boom arms of the tower could also contribute to lower observed UVW wind speeds at boom-parallel wind directions as noted with other anemometers (Pedersen et al. 1992). Despite the differences between the two platforms, the comparison illustrates the accuracy of using dual-Doppler methods in wind speed direction estimation.

These techniques have recently been employed to obtain valuable wind profiles within design-level thunderstorm outflow events in Project SCOUT. Thunderstorms capable of producing strong damaging outflow winds were targeted across the Great Plains. The coordinated RHI method was used to obtain wind speed and direction profiles ahead of the thunderstorm gust front and within the high-intensity winds of thunderstorm outflow. Examples from a design-level event from SCOUT are included in Figure 1.2.2.5. Although the analysis of SCOUT datasets continues, these preliminary data can be used to improve structural design codes, validate many numerical models, and contribute to better understanding of the structure of thunderstorm outflow winds.

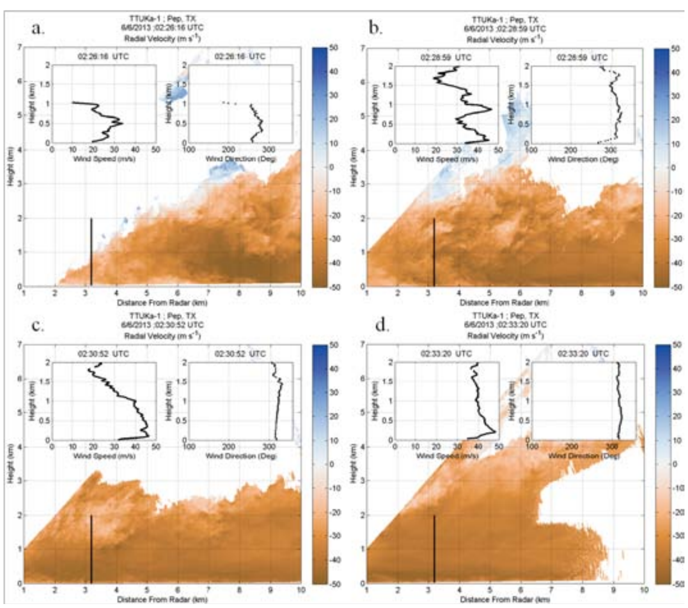

Figure 1.2.2.5. Single Doppler RHI snapshots and inset wind speed and direction profiles from 4 selected time periods of the Pep, TX dataset. Warm colors indicate inbound radial velocities, while cool colors indicate outbound radial velocities. Vertical black bar in the RHI represents the location of the inset dual-Doppler wind profiles.

Subtask 1.3: Use the 200 m Tower to Measure the Wind Characteristics of Significant Weather Events Common to the Great Plains. Incorporate the Measured Field Data into Computer-Based Wind Turbine Simulations to Estimate the Effect on Wind Turbine Loading and Reliability.

1.3.1. Estimating Extreme Loads.

1.3.1.1 Introduction.

Reliability- and performance-based wind turbine design requires estimation of extreme responses with various mean recurrence intervals (MRIs), i.e., 50 years. The International Electrotechnical Commission standard (IEC 61400-1 2005) recommends a load (response) extrapolation procedure to estimate the large extreme responses from short-term 10 min simulations of turbine response at various mean wind speeds. Based on these simulations, the distributions of extreme responses over 10 min conditional on various wind speeds are estimated and fitted with given probability distribution models, which are then combined with the distribution of mean wind speed for the estimation of overall short-term extreme value distribution. The extreme responses with various MRIs are subsequently estimated. For instance, the 50-year extreme response corresponds to an exceeding probability of 3.8×10^{-7} in terms of 10 min maxima, which requires information of probability distribution at the very upper tail.

Previous studies have shown that the predicted long-term extreme responses are very sensitive to the probability models used in fitting the extreme value distributions at various wind speeds. Different distribution models, while fitting the simulated extreme data well, can have very distinct behaviors in the upper tails that result in very different predictions of long-term extremes (Agarwal and Manuel 2008; Freudenreich and Argyriadis 2008). In order to provide a guideline for the appropriate implementation of the extrapolation procedure mandated by current wind turbine design standards, a number of studies were carried out. Among these research efforts, Moriarty (2008) carried out direct Monte Carlo simulation (MCS) of turbine response for a total of 5 years of operation involving about 48,000 samples of 10 min simulations per year. Natarajan and Verelst (2011) utilized principal component analysis technique to weight the sampled outliers and reduce the extrapolation uncertainty from different sample sizes. Besides, the asymptotical sampling method and Markov chain Monte Carlo simulation are also applied (Sichani et al. 2011; Sichani and Nielsen 2012).

In this study, a two-phase research program is conducted. Phase one is to develop a more efficient MCS framework that enables a direct simulation of extreme response distribution with much reduced computational efforts. Phase two is to evaluate the performance of different statistical extrapolation methods used in the practical design of wind turbines by comparing the predictions to the ones from phase one.

1.3.1.1.a. Wind Turbine Model and Random Wind Field.

The 5MW onshore baseline wind turbine model developed by the National Renewable Energy Laboratory (NREL) is used, which has a hub height of 90 m and rotor diameter of 126 m (Jonkman et al. 2009). The turbine uses variable-speed and collective pitch-control configuration with a rated wind speed of 11.4 m/s and a rated rotor speed of 12.1 rpm. The turbine operating wind speed range is between cut-in speed of 3 m/s and cut-out speed of 25 m/s. The random wind field in terms of *u*-, *v*- and *w*-components of wind fluctuations is represented by a 15-by-15 grid with a width of 137 m in both directions, which is sufficient to cover the rotor when the possibility of yaw and tilt are accounted. The turbulence model as specified in the IEC standard is used in this study.

1.3.1.1.b. Wind Turbine Responses and Extrapolation for Long-term Extremes.

The FAST (Fatigue, Aerodynamics, Structures, and Turbulence) code is used for turbine response analysis, which is a comprehensive aeroelastic simulator capable of predicting the extreme and fatigue loads of three-bladed, conventional, horizontal-axis wind turbines (Jonkman and Buhl 2005). The time history sample and the power spectral density (PSD) function of out-of-plane bending moment under mean wind speed at hub height (U_{hub}) of 15 m/s is displayed in Figure 1.3.1.1 as an example, where $\text{P} = 0.2017$ Hz is the frequency of turbine rotation.

To determine the extreme turbine responses with a given MRI, i.e., 50 years, the operational wind speed range is divided into 12 wind speed bins with a width of 2 m/s. Simulations of turbine response are carried out for the quantification of extreme value distribution of turbine responses conditional on wind speed. i.e., $\Pr\,(Y > y | V = v)$, where Y is the extreme value of 10 min response, and $V = U_{\text{hub}} = v$ is the mean wind speed at turbine hub height. The short-term extreme response distribution conditional on wind speed can be determined by controlled MCS or statistical extrapolation method, which will be discussed later in detail. These conditional distributions are then integrated with the Rayleigh distribution of mean wind speed to estimate the overall short-term extreme value distribution (IEC 61400-12005)

$$\begin{aligned}\Pr(Y > y) &= \int_v \Pr(Y > y|V = v) f(v) dv \\ &= \sum_{j=1}^{12} \Pr\big(Y > y|V = v_j\big)\left[e^{-\pi\left(\frac{v_j - 0.5\Delta v_j}{2v_{\text{ave}}}\right)^2} - e^{-\pi\left(\frac{v_j + 0.5\Delta v_j}{2v_{\text{ave}}}\right)^2}\right]\end{aligned} \quad (1)$$

where $f(v)$ is the probability density function (PDF) of mean wind speed, which follows a Rayleigh distribution; v_{ave} is expected value of the mean wind speed; v_j $(j = 1,2,\cdots,12)$ are the mean wind speeds at bin centers; and Δv_j is the bin width. In this study, $v_{\text{ave}} = 10$ m/s and $\Delta v_j = 2$ m/s. Then the long-term extreme response with a given MRI is determined from the probability of exceedance $\Pr(Y > y)$. The probability of exceedance of R-year extreme response is calculated as $10/(R \times 365 \times 24 \times 60)$. The 1-year, 10-year and 50-year extremes correspond to the probability of exceedance of 1.9×10^{-5}, 1.9×10^{-6} and 3.8×10^{-7}, respectively.

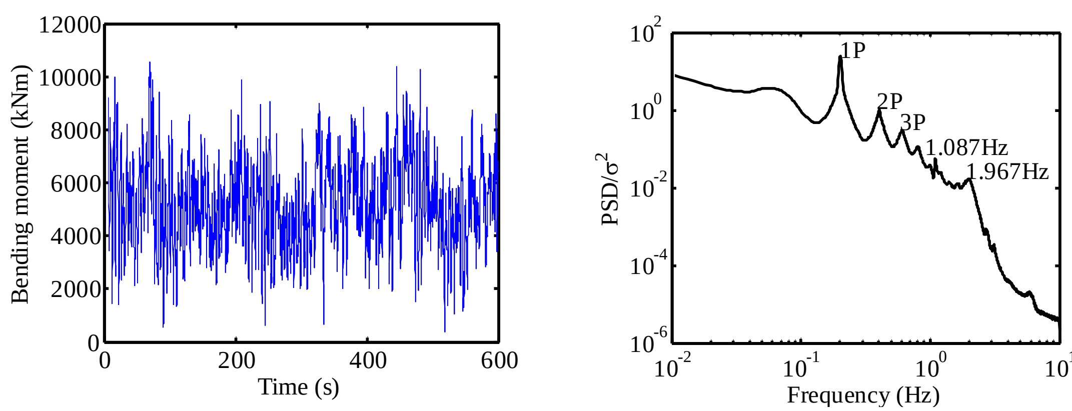

(a) Time history (b) PSD function

Figure 1.3.1.1. Blade root out-of-plane bending moment (U_{hub} = 15 m/s).

1.3.1.2. Results and Discussion.

1.3.1.2.a. Long-term Extreme Responses by Controlled MCS.

The direct MCS is prohibited for simulating a rare event as the required sample size of MCS is inversely proportional to its occurrence probability. Therefore, a controlled MCS framework that combines importance splitting (ISp) with multivariate autoregressive (MAR) modeling of wind excitations was developed in Ding and Chen (2013). Following this scheme, to determine the probability of exceedance of response within 10 min, i.e., $p_f = \Pr\,(Y > y)$, an increasing sequence of intermediate thresholds, $0 < y_1 < y_2 < \cdots < y_m = y$, can be selected, where m is total number of thresholds. (See also in Au and Beck 2001). Then the evaluation of a rare event is transformed to estimations of a sequence of subset events with larger conditional probabilities.

$$\Pr(Y > y_m) = \prod_{i=1}^{m} p_i \qquad (2)$$

where $p_i = \Pr\,(Y > y_i | Y > y_{i-1})$. The ISp is a method that splits important sample paths into multiple branches at various stages of simulation, by which the conditional probability p_i for a given threshold (or the threshold for a given conditional probability) can be evaluated. The implementation and optimal setting of this framework are discussed in detail in Ding and Chen (2013).

This framework is applied to evaluate the wind turbine responses under various mean wind speeds. During each run of the proposed ISp scheme, 200 samples are used on each stage for the determination of thresholds with given conditional probabilities. Totally 20 independent runs are conducted and the final results are obtained by the ensemble average of the estimates. Figure 1.3.1.2 shows the overall probability of exceedence for the blade root out-of-plane bending moments in terms of 10 min extreme response, which is obtained by first determining the conditional probability of exceedance on each wind speed bin, i.e., $\Pr\,(Y > y | V = v_j)$, $(j = 1, 2, \cdots, 12)$, then integrating with the distribution of mean wind speed following Eq. (1). The year-long data set reported in Moriarty (2008) from direct MCS is also presented. Comparison of the results from the proposed framework and year-long data set shows both results are in very good agreement. It is worth mentioning that there is only 5 years of data obtained from direct MCS by Moriarty (2008). To further evaluate an extreme response with a MRI of 50 years ($p_f = 3.8 \times 10^{-7}$), 2,630,000 (i.e., $1/p_f$) samples are needed to generate one extreme estimate when direct MCS scheme is used. On the other hand, a very good estimate from the proposed framework can be obtained by only about 25,600 samples (20 runs with 1280 samples per run) for each wind speed bin, which makes the simulation feasible.

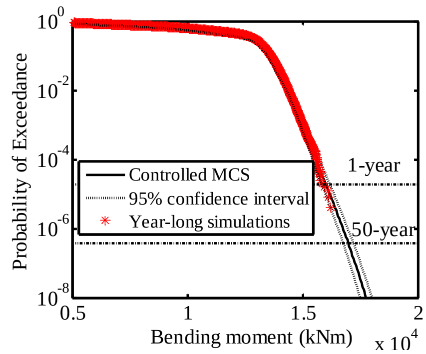

Figure 1.3.1.2. Simulated overall probability of exceedance for blade root out-of-plane bending moments.

1.3.1.2.b. Long-term Extreme Responses by Statistical Extrapolation: Global Maxima Method.

In current wind turbine design standards, the estimation of long-term extreme responses has to be relied on a limited number of 10 min response time histories at given wind speeds. Following the extrapolation procedure described in IEC standard, extremes extracted from 200 response time histories at each wind speed bin (Figure 1.3.1.3(a)) are used to fit selected probability distributions, such as Gumbel distribution, quadratic Gumbel distribution, lognormal distribution, generalized extreme value (GEV) distribution and Weibull distribution. In this application, the distribution model parameters are determined based on method of moments, except that the quadratic Gumbel distribution is by curve fitting to the CDF. The final results are shown in Figure 1.3.1.3(b), as compared to the results from controlled MCS. It is evident that the statistical extrapolations from global maxima are greatly relying on the prescribed distribution models.

1.3.1.2.c. Long-term Extreme Responses by Statistical Extrapolation: Translation Process Method.

The translation process method collects information of the entire response time history and relates it to an underlying Gaussian process through a monotonic translation model, which is based on the translation process theory (Grigoriu 1995). For a given value of non-Gaussian process, the corresponding value of the underlying Gaussian process is determined such that both values are associated with an identical value of cumulative distribution function (CDF). This procedure for quantifying the translation function is referred to as CDF mapping. Once the analytical translation model is fixed, the extreme value distribution of the response time history can be established based on the well-developed extreme value theory for Gaussian process (Chen and Huang, 2009).

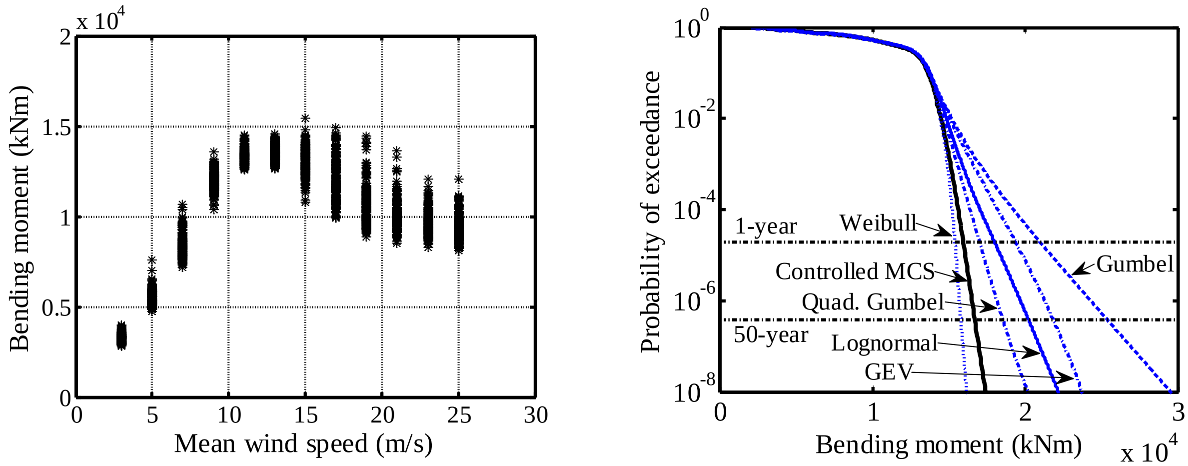

(a) 200 extremes in each wind speed bin (b) Extrapolated overall probability of exceedance

Figure 1.3.1.3. Blade root out-of-plane bending moment.

This method is applied as an alternative for statistical extrapolation of long-term extreme response of wind turbines. The advantage of this method relies on two aspects: first, a distribution model is not required to be specified thus the great influence of distribution model on the extrapolation can be eliminated; second, the extreme value analysis is derived from the response time history instead of its maxima, so more response process information is used and the predictions are expected to be more stable. However, the improved performance of this method is relied on an accurate representation to the upper tail of empirical translation function. The details of the translation model and its model coefficients based on least square optimization are referred to Ding et al. (2013). Figure 1.3.1.4 shows the predictions from the improved translation process method with comparison to the results from controlled MCS, which demonstrates that the results from extrapolation with translation process method is acceptable. The prediction difference for MRIs of 1 and 50 years are less than 5%.

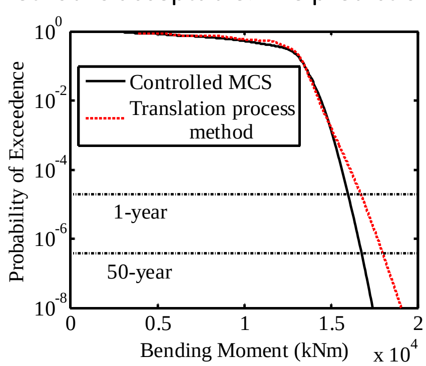

Figure 1.3.1.4. Probability of exceedance by controlled MCS and extrapolation with translation process method.

1.3.1.3. Conclusions.

An effective controlled MCS framework for evaluating long-term extreme responses of wind turbines was proposed, which combines the ISp method with MAR modeling of excitations. This framework significantly enhanced the computational efficiency as compared to the traditional MCS method and it enables a direct simulation of the long-term extreme responses. This framework is also applicable for the evaluation of extreme responses of other dynamical structural systems, which is not limited to the wind turbines.

The performances of statistical extrapolation methods were investigated with comparison to the predictions from controlled MCS. It was confirmed that the global maxima method was less reliable as its prediction was greatly affected by the prescribed probability distribution model used to fit the maximum data. The translation process method with improved modeling of translation function at the upper tail region led to satisfactory results. With the advantage of a significant saving of computational effort and acceptable accuracy compared to the direct simulation, the translation process method is one of the good candidates for statistical extrapolations of wind turbine extreme responses.

1.3.2. Simulation of Turbine Inflow and Assessment of Turbine Response.

1.3.2.1. Introduction.

Historically, the understanding of wind in the earth's atmospheric boundary layer and its effects on structures has mostly been derived from the study of wind loading of structures such as buildings and bridges. This knowledge base has been used in the structural design of wind turbines. Considering the mechanical nature of wind turbines and the wind regimes to which they are susceptible, however, this practice may potentially be inadequate or even inappropriate. For the reliability of buildings and bridges, except for problems related to vortex-shedding, only winds of high speeds are critical. Wind turbines, however, are subjected to not only extreme loading at high wind speeds, but also fatigue loading at low to moderate wind speeds (e.g., 3 m/s to 25 m/s at hub height) since this is the speed range over which they operate. Consequently, it can be problematic to neglect the unique characteristics of low-to-moderate speed winds and use the models and parameters that are only applicable to high speed wind in the assessment of wind turbine fatigue loading. For example, the mean wind speed and direction profiles as well as the turbulence characteristics of low-to-moderate speed wind in the lower atmospheric boundary layer can be significantly different from those of high speed winds since the former depend significantly on the thermal effects, manifested as atmospheric stability, while the latter can be assumed to be atmospherically neutral due to the dominant mechanical effects compared to the thermal effects. Although some recent studies have parametrically investigated the effect of atmospheric stability on the mean wind speed profiles and the consequent influence on wind turbine fatigue loading (e.g., Ameya and Wim 2007, Jonathon and Christian 2006), these studies are not based on comprehensive meteorological measurement to the heights of current and especially future wind turbines. As a result, the characteristics of the wind in stable boundary layers at the upper part of the wind turbine blade swept area might not have been adequately represented. Also, in assessing the extreme loading of wind turbines, the current practice assumes that the turbulence is stationary. This can be problematic as many types of extreme wind, such as thunderstorm downbursts, can be highly non-stationary (e.g., Chen and Letchford 2006, Chen and Letchford 2005).

Problems such as these in the current practice of wind turbine structural design are further exacerbated with the rapid growth in wind turbine size, which results in large sweeping areas by wind turbine blades. To date, the rated capacity of land-based commercial horizontal-axis wind turbines has reached 3 MW, and that of offshore turbines has reached 5 MW (Bilgili et al. 2011), with much larger ones being developed. The hub-height and the rotor diameters of these turbines have reached or exceeded 100 m. The effects of the size increase on wind turbine reliability are two-fold. On the one hand, the structures themselves have become increasingly more flexible and, consequently, more susceptible to undesirable wind-induced oscillations. On the other hand, the increased size of the blade sweeping area subjects these structures to potential spatially varying, much more complex, wind fields. While one should not discount the effect of the structural change of wind turbines, improved representation of the inflow wind field has a critical impact on the loading of all types of wind turbines. Therefore, to improve the reliability of wind turbines, it is imperative to further advance the understanding of wind as well as to develop methodology that can be used to simulate wind turbine inflow field.

Motivated by these considerations, this part of the research conducted measurement to characterize various types of wind and, on this basis, developed methodologies for numerical simulation of inflow fields critical for the structural response of utility-scale wind turbines. The core parameters characterized using this measurement were used as input to wind simulations which generated statistics for assessment of the response of representative wind turbines to wind loading. The findings from these research efforts are summarized in the subsequent sections.

1.3.2.2. Results and Discussion.

1.3.2.2.a. Characterizing the Wind.

The experimental facility used in this part of the study a 200 m meteorological tower located near the campus of Texas Tech University in Lubbock, Texas. This tower is instrumented with 10 levels (0.9 m, 2.4 m, 4.0 m, 10 m, 17 m, 46 m, 75 m, 116 m, 158 m, and 200 m, respectively, above ground) of research grade ultrasonic anemometers. Propeller-based UVW anemometers are instrumented at the upper 8 levels. At every level, the tower is also instrumented with temperature, barometric pressure and humidity sensors. From December 7, 2011 to February 18, 2012, all channels were sampled at 20 Hz; after this period, the sampling rate was 50 Hz. The system records a data file every half an hour. Figure 1.3.2.1 shows a satellite image of the tower and the surrounding terrain, which is flat and with minimal obstructions.

Data recorded by the tower from December 2011 to July 2012 will be used subsequently to assess the wind characteristics in stable boundary layers. Data associated with wind at any level going through or nearly going through the tower are excluded. The statistical data to be presented are based on 10-minute segments obtained by splitting each 30 minute record into three segments.

The Monin-Obukhov length and the gradient Richardson number are two parameters most commonly used to describe the stability of the atmospheric boundary layer (Stull 1988). With the availability of temperature and barometric pressure measurements at all the levels of instrumentation, the gradient Richardson number is chosen herein to represent the stability of the boundary layer at the site of the

200 m tower. The gradient Richardson number is defined as

$$Ri = \frac{g}{\overline{\theta}}\left(\frac{\partial\overline{\theta}}{\partial z}\right)\left(\frac{\partial\overline{U}}{\partial z}\right)^{-2} \quad (1)$$

where *g* is the gravitational acceleration, *U* is the mean horizontal wind speed, *z* is the height above ground, and *Θ* is the potential temperature given by

$$\theta = T\left[\frac{1000}{P}\right]^{0.286} \quad (2)$$

where *T* is the absolute temperature and P is the barometric pressure in hectopascal. The overbars in equation 2 represents averaging. Stable, neutral and unstable atmospheric boundary layers are represented by *Ri*>0, *Ri*=0, and *Ri*<0, respectively.

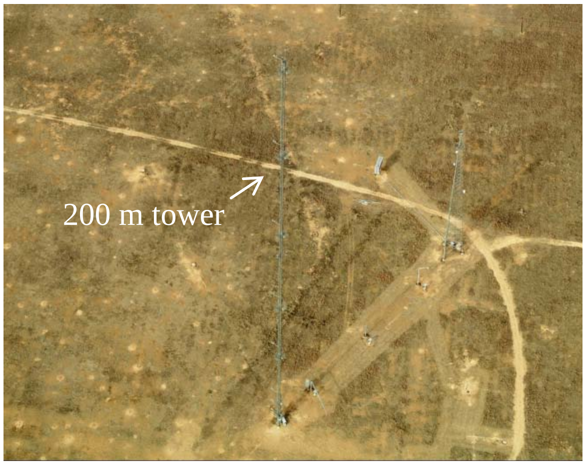

Figure 1.3.2.1. 200 m meteorological tower and surrounding terrain (Windows Live).

The stability of the atmospheric boundary layer is closely related to the diurnal cycle. During the day, the heat from the sun causes the boundary layer to be convective (stable); during the night, the surface of the earth cools down and the boundary layer becomes statically stable. True neutral atmospheric boundary layers are seldom observed.

Figure 1.3.2.2. shows the average diurnal variation of the gradient Richardson number. Only records with mean wind speed greater than 5 m/s at the 116 m level are used to generate this graph and the subsequent graphs showing the statistics of the measurements. UTC in this graph represents Coordinated Universal Time. For the period of measurements, before March 11, 2012, the UTC time is 6 hours ahead of the local time; after this day, the UTC time is 5 hours ahead of the local time. It can be seen that on average, the atmospheric boundary layer over this site is stable from early evening to early morning and unstable during the day time. The transition occurs shortly after sunrise and shortly before sunset.

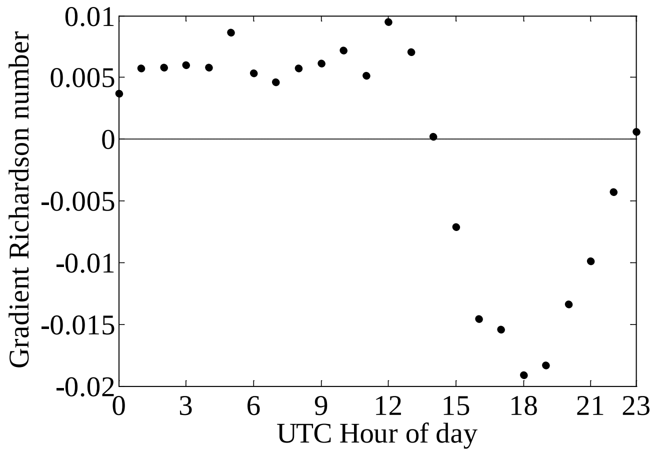

Figure 1.3.2.2. Average diurnal variation of gradient Richardson number.

The data suggest that the stability of the atmospheric boundary layer significantly affects the mean wind field in both wind speed and wind direction. As an illustration, Figure 1.3.2.2. depicts the evolution of the gradient Richardson number and the corresponding 10-minute mean temperature profile (in Celsius) over an example 24 hour time period. The contour plot of the temperature profile, as well as the other contour plots to be presented subsequently, is based on linear interpolation of adjacent 10-minute mean values and adjacent measurement heights. It can be seen that during the day time from late morning to early evening, the air temperature decreased with increasing height. During the time from early evening to early morning, however, temperature inversion was very pronounced. This change of temperature gradient is reflected in the corresponding evolution of the gradient Richardson number, thus the stability of the atmospheric boundary layer estimated based on the 10 levels of meteorological measurements.

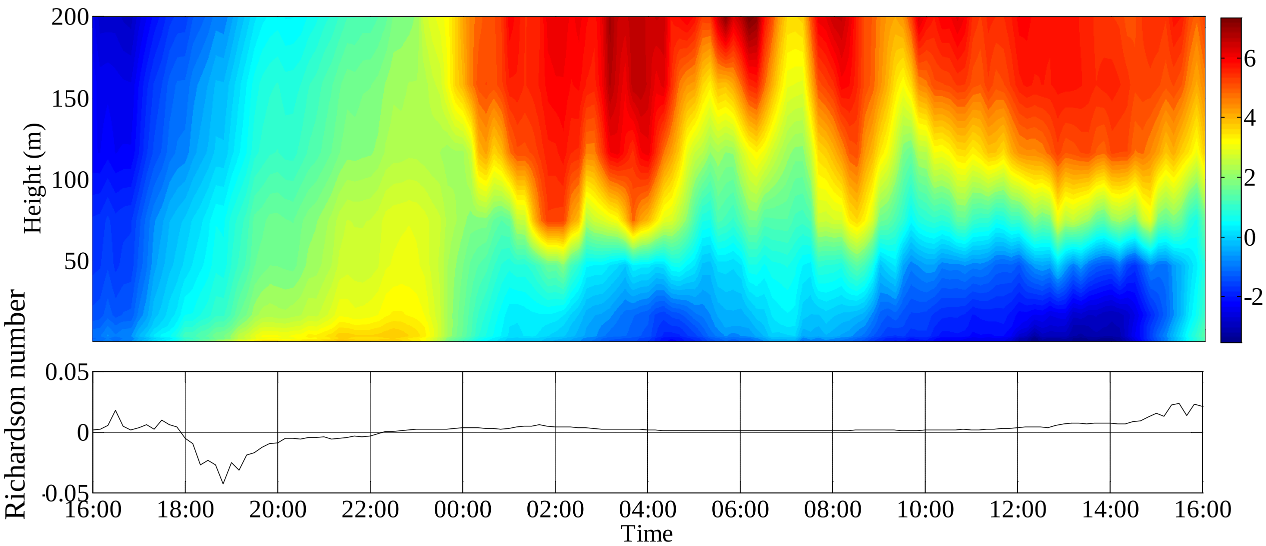

Figure 1.3.2.3. Variation of mean temperature (°C) profile and gradient Richardson number during a 24 hour period.

Figure 1.3.2.4 shows the evolution of the mean wind speed (in m/s) profile during the same 24 hours. It is evident that below the levels of maximum wind speed, the wind speed shear was markedly higher when the boundary layer was stable than when it was unstable. It also can be seen that during some periods of time (e.g., from 13:00 to 14:00), the maximum wind speed occurred at levels below 200 m, suggesting the occurrence of low level jets due to decoupling of flows from surface friction, resulting in the formation of a layer of strong wind (Banta et al. 2002).

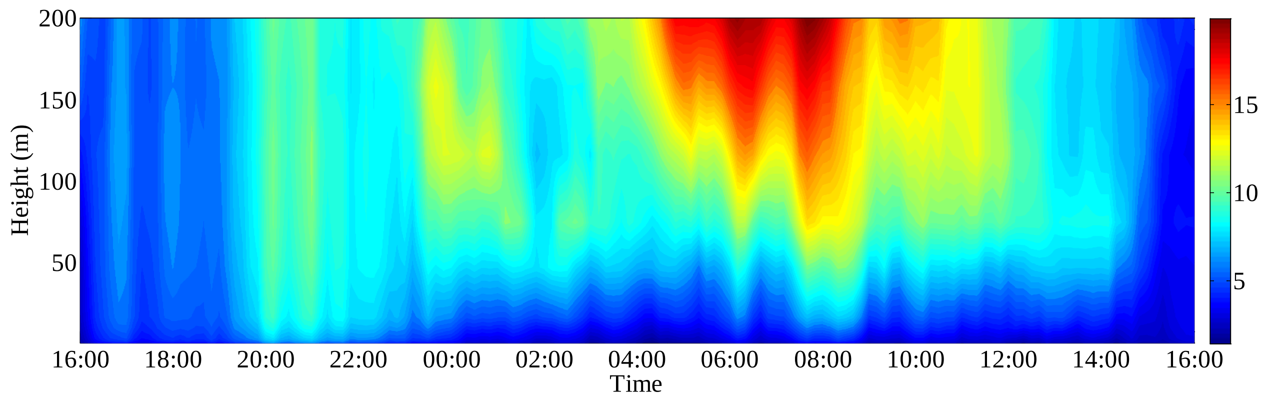

Figure 1.2.3.4. Variation of mean wind speed (m/s) profile during a 24 hour period.

Figure 1.3.2.5 shows the evolution of the mean wind direction (in degrees) profile. In this figure, the wind direction at 116 m level is taken as having a zero wind direction shear and the direction shear at other levels are relative to the wind direction at this level. Strong wind direction shear along the 200 m can be observed when the boundary layer was stable. The mechanism that generates the dramatic wind direction shear present in Figure 1.3.2.5 remains to be identified. It obviously cannot be accounted for by the Ekman spiral. Also, while some early studies have indicated the existence of significant (i.e., 30° to 60°) wind direction shear across stable boundary layers (Nieuwstadt 1984), direction shear close to that present in Figure 1.3.2.5 has seldom been reported (Walter et al. 2009).

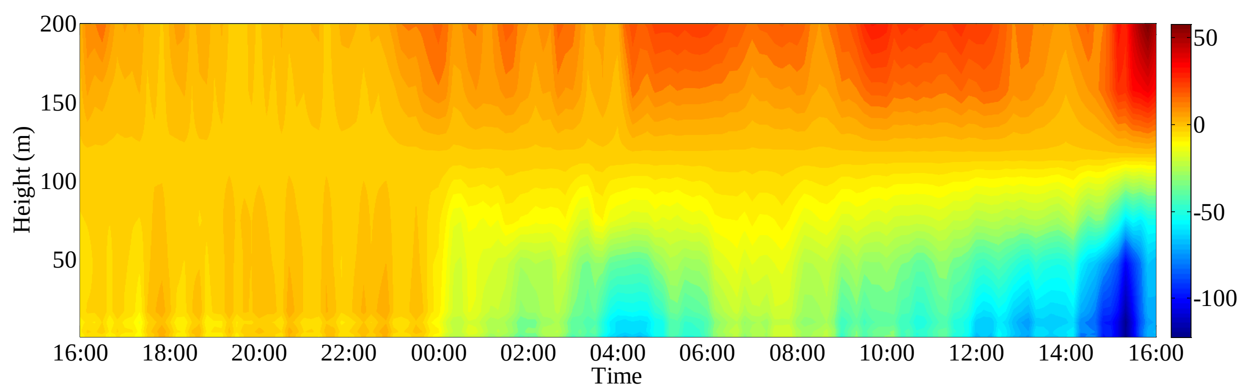

Figure 1.3.2.5. Variation of mean wind direction profile during a 24 hour period.

Diurnal variation of mean wind speed and direction profiles as illustrated in Figure 1.3.2.4 and Figure 1.3.2.5 are not uncommon at this site. Figure 1.3.2.6 illustrates statistically the diurnal variation of the stability of the atmospheric boundary layer represented by the gradient Richardson number. As expected, the atmospheric boundary layer was consistently stable during night-time and unstable during daytime.

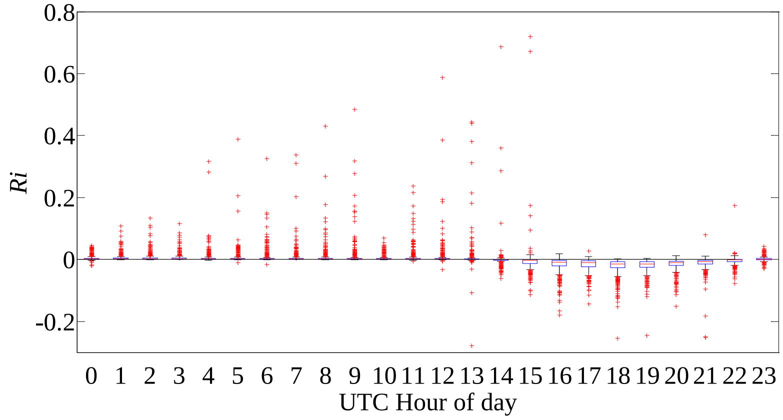

Figure 1.3.2.6. Diurnal variation of gradient Richardson number.

The consistent evolution of the atmospheric stability over the diurnal cycle also resulted in distinct characteristics of the wind in the atmospheric boundary layer during daytime and nighttime. Figure 1.3.2.6 shows the statistical diurnal variation of the wind speed shear of the boundary layer, represented by the roughness length value (z_0) estimated based on fitting the wind measurements up to the 46 m level with a logarithmic profile. The manner in which the roughness length is estimated is apparently not valid as the boundary layer is not logarithmic in either stable or unstable conditions. Nonetheless, the incorrectly estimated roughness length does imply the degree of wind speed shear. It is apparent in Figure 1.3.2.7 that statistically the boundary layer had strong wind speed shear, represented by large z_0 values, during night-time when the boundary layer was stable and low wind speed shear, represented by small z_0 values, during daytime when the boundary layer was unstable.

Figure 1.3.2.8 shows statistically the diurnal variation of the wind direction veer over a portion of the boundary layer, which is represented by the difference between the wind directions measured by the anemometers at the 46 m and 116 m levels on the 200 m tower. While the direction veer in unstable boundary layers during daytime was insignificant, the amount of direction veer in stable boundary layers during night-time could be remarkably large.

It is known that in stable boundary layers, the generation of turbulence is suppressed due to temperature inversion (e.g., Kelley et al. 2004, Wharton and Lundquist 2010), and it has been shown that the structure of wind turbulence in the surface layer can be different from that of the wind turbulence in neutral or unstable boundary layers (e.g., Caughey et al. 1979). However, little work has been done to investigate the wind turbulence beyond the surface boundary layer. In the following, an example will be used to illustrate the difference between wind turbulence in stable and unstable boundary layers.

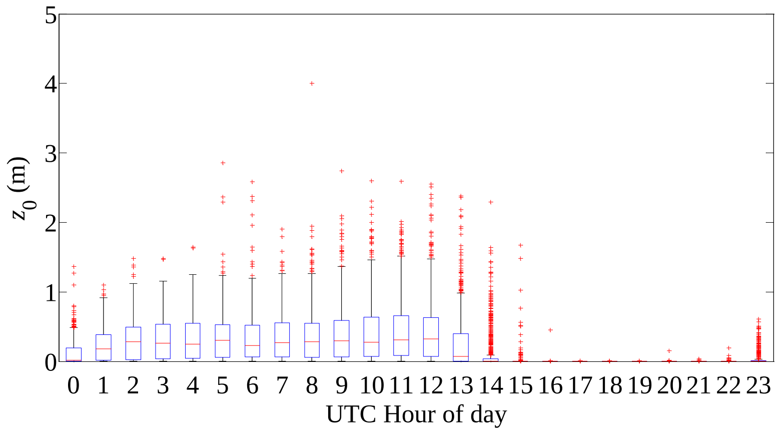

Figure 1.3.2.7. Diurnal variation of wind speed shear.

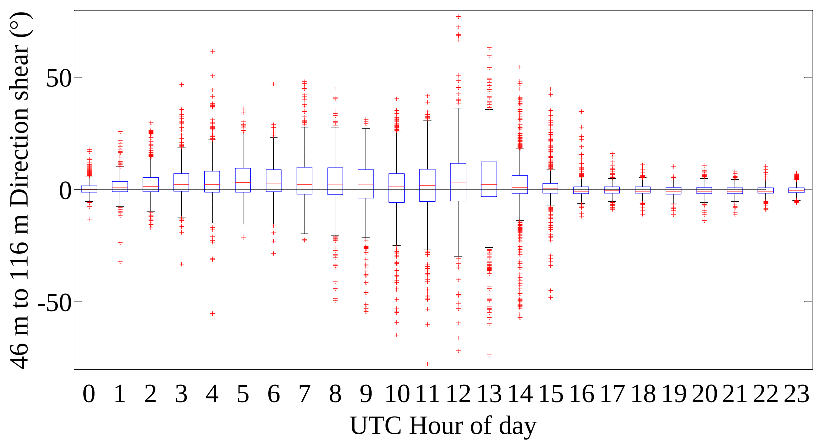

Figure 1.3.2.8. Diurnal variation of wind direction veer.

Figure 1.3.2.9 shows the diurnal variation of the longitudinal turbulence intensity of wind in the boundary layer whose mean characteristics are illustrated in Figure 1.3.2.3 to Figure 1.3.2.5. It is obvious that at the upper levels, the wind was much less turbulent when the boundary layer was stable than when it was unstable. Although not shown herein, the same observations have also been made for lateral and vertical turbulence.

Figure 1.3.2.10 shows the variation of the estimated longitudinal integral length scale (in meters) profile during the same period of time. It can be seen that when the boundary layer was stable, the longitudinal integral length scales were much larger than what would be expected in an unstable or neutral boundary layer, which is often on the order of hundreds of meters (e.g., Simiu and Scanlan 1996). Although not shown here, the integral length scale in the other two directions are also large at higher levels when the boundary layer was stable. This indicates the existence of large eddies in the wind at higher level in the stable boundary layer, where the wind is less affected by the friction at the surface of the earth.

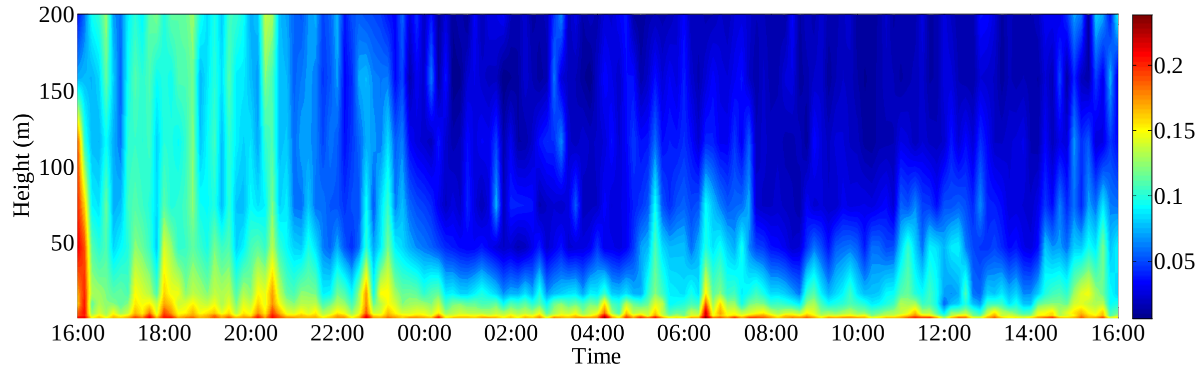

Figure 1.3.2.9. Variation of mean turbulence intensity profile during a 24 hour period.

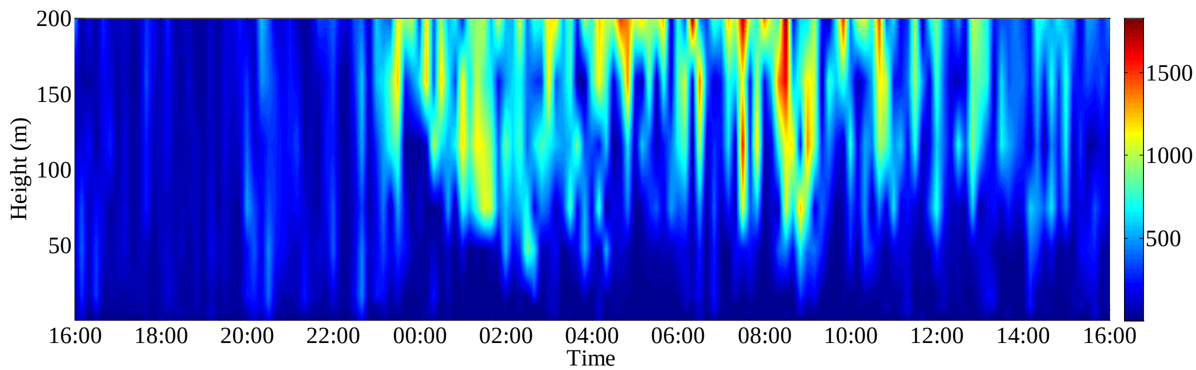

Figure 1.3.2.10. Variation of mean turbulence intensity profile during a 24 hour period.

Figure 1.3.2.11 illustrates the difference between the estimated spectrum of the longitudinal turbulence at two levels when the boundary layer was stable. n in this figure is frequency, S_{uu} and σ_u are the auto-spectral density function and the standard deviation of the longitudinal turbulence. The spectra shown were estimated based on measurements from 13:50 to 14:00 UTC. For reference purposes, the Kaimal spectrum and Von Kármán-Harris spectrum are also included in the graphs. These two forms of spectrum (instead of the models proposed in the literature for the spectrum of longitudinal turbulence in stable boundary layers (e.g., Moraes 1988)) are used to highlight the difference between the turbulence spectra in stable boundary layers and those in neutral and unstable boundary layers. It can be seen that, at the 10 m level, the estimated spectrum approximately resembles that of the Kaimal or Von Kármán-Harris form because friction effects dominates at this level. At the 116 m level, however, the estimated spectrum is completely different from the Kaimal or Von Kármán-Harris form because at this level, the generation and dissipation of the turbulent energy is affected less by friction but more by thermal effects.

In addition to the differences between the turbulence of wind in stable and unstable boundary layers as illustrated above, the measurements by the 200 m tower also revealed that the turbulence of wind in stable boundary layers can be highly non-Gaussian. As an illustration, Figure 1.3.2.12 shows the profiles of the skewness and kurtosis profiles of the along-wind turbulence for a collection of 10-minute wind events in stable boundary layers. It is evident that for many of these events, at heights above the surface layer (e.g., the first tens of meters), the skewness and kurtosis of the turbulence deviated from zero and

3, respectively, which are the values for a Gaussian process. As a contrast, at near the ground level, the skewness and kurtosis of the turbulence were close to zero, indicating that the along-wind turbulence was more close to Gaussian. This difference between the probability distribution of the wind at lower and higher levels in stable boundary layers is due to the fact that at lower heights, the turbulence is primarily generated by the friction between the flow and the ground, which results in small eddies, the sum of which resembles a Gaussian process according to the central limit theorem and that at higher heights, the effects of the friction becomes less significant and the thermal effects becomes pronounced, resulting in larger eddies (as illustrated in Figure 1.3.2.11) the combination of which can be significantly non-Gaussian.

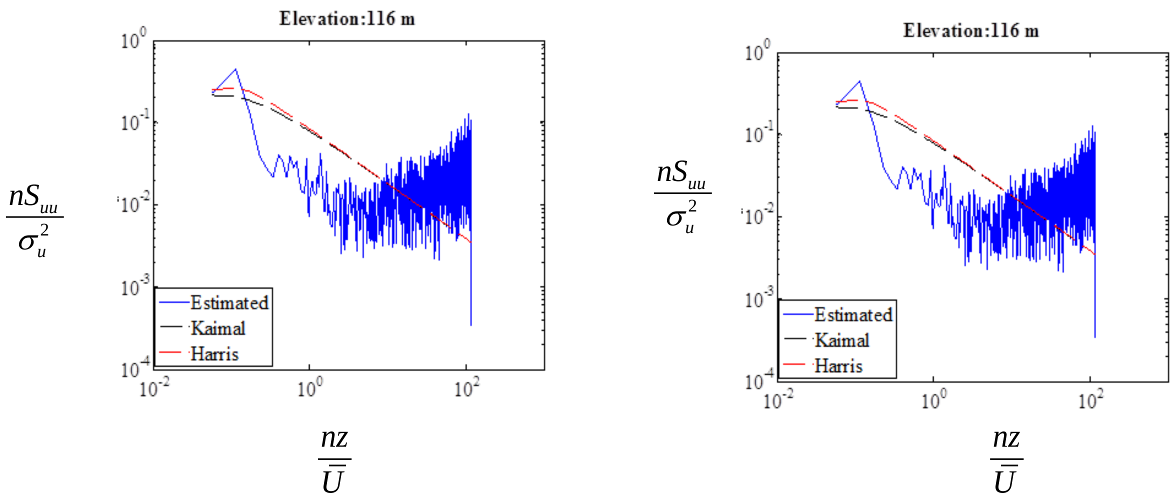

Figure 1.3.2.11. Comparison of the spectra of longitudinal turbulence at two levels in a stable boundary layer.

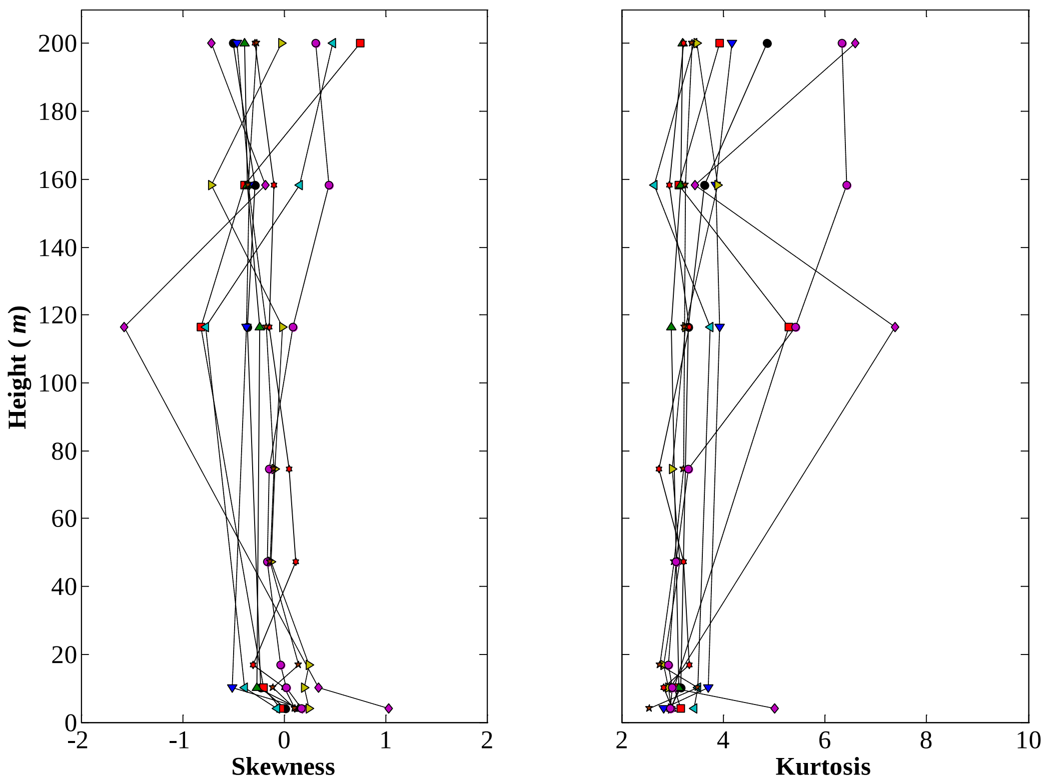

Figure 1.3.2.12. Skewness and kurtosis profiles for a collection of 10-minute wind events in stable boundary layers. Distinct symbols represent distinct events.

1.3.2.2.b. Characterization of Non-Stationary Thunderstorm Wind.

Only limited work has been done to study the loading by thunderstorm winds on operational wind turbines. In the limited studies, thunderstorm outflow turbulence has been treated as being both Gaussian and stationary (Nguken et al. 2011), despite the fact that many studies on thunderstorm winds have indicated the contrary (e.g., Chen and Letchford 2007). In this study, methodologies based on the wavelet transform were used to characterize the nature of thunderstorm winds. An example is used in the following to illustrate the application of these methodologies.

Thunderstorms are highly non-stationary events that have no meaningful, conventional mean wind speed profile. In this study, a thresholding method based on the wavelet transform (e.g., Addison 2002) is used to extract the wind component that varies slowly from the total wind speed time history. As an illustration, Figure 1.3.2.13 shows the time history of wind speed during a thunderstorm wind event and the time-varying mean wind speed extracted using a 10th level Daubechies wavelet of order 3. With this wavelet, the time-varying mean component is composed of wind turbulence with frequencies lower than 0.024 Hz. Such estimation of the time-varying mean wind components at different heights above the ground level can enable a further estimation of the evolution of the time-varying mean wind profile over the height of a wind turbine.

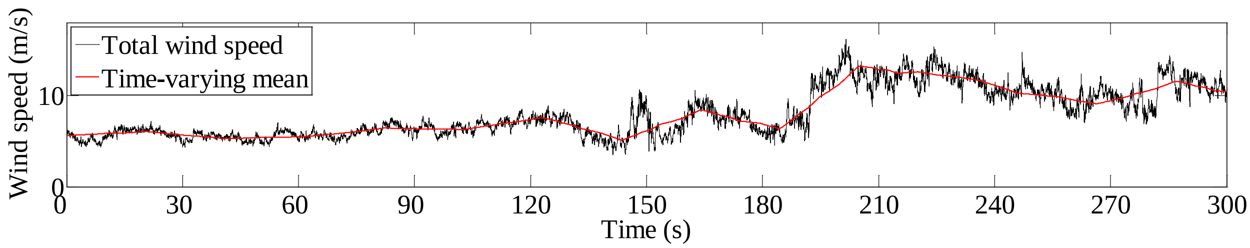

Figure 1.3.2.13. Extraction of time-varying mean component from a non-stationary thunderstorm wind speed record.

The time-varying mean component estimated based on wavelet thresholding can be subtracted from the total time history to yield the turbulence of higher frequency in thunderstorm winds. For example, Figure 1.3.2.14 shows the time history of the turbulence extracted in this manner from the total wind speed time history shown in Figure 1.3.2.13. It is apparent that the turbulence is highly non-stationary.

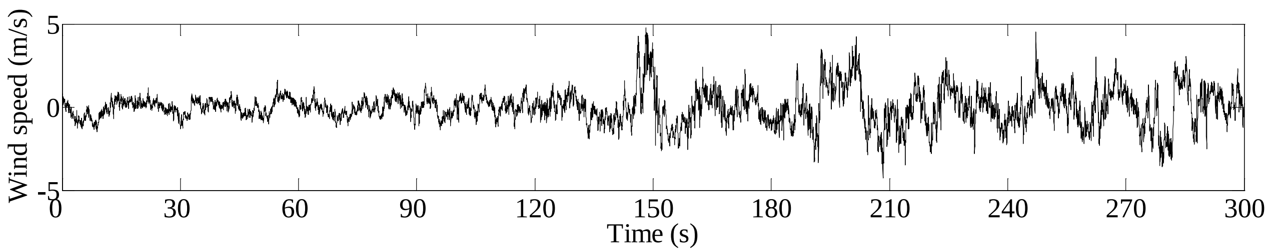

Figure 1.3.2.14. Turbulence of a thunderstorm wind record.

Since the turbulence of thunderstorm wind is non-stationary, the conventional auto-spectral density function does not exist for this turbulence. However, the so-called evolutionary power spectral density function (EPSD, Preistley 1965) can be used to enable a representation of the turbulence in the time-frequency domain. Figure 1.3.2.15 shows the evolutionary power spectral density function estimated based on the wind turbulence time history shown in Figure 1.3.2.14. It is apparent that both the intensity and frequency of the turbulence were evolving with time.

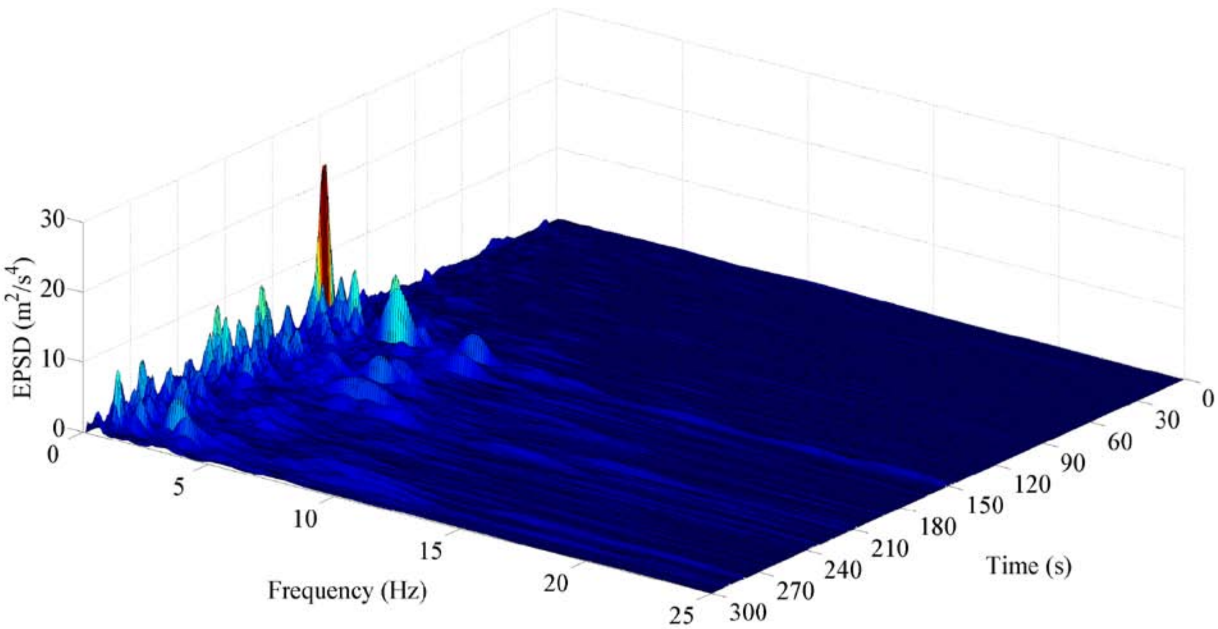

Figure 1.3.2.15. Evolution spectrum of non-stationary turbulence.

As illustrated using the data recorded based on the 200 m tower, a wind turbine can be subjected to inflow fields that are significantly different from what is prescribed in the current wind turbine design practice. To enable a realistic assessment of the wind loading on wind turbines, a methodology based on spectral representation (e.g., Sinozuka and Jan 1972) was used to conditionally simulate wind turbine inflow fields based on the wind measurements by the 200 m tower. The conditional simulation starts with translating the measured non-Gaussian turbulence into the underlying Gaussian processes (e.g., Winterstein 1988), the spectra of which are used to assemble the spectral matrix of the wind inflow field as

$$\mathbf{S}(f_m) = \begin{bmatrix} \mathbf{S}_{kk}(f_m) & \mathbf{S}_{ku}(f_m) \\ \mathbf{S}_{uk}(f_m) & \mathbf{S}_{uu}(f_m) \end{bmatrix} \quad (1)$$

in which $\mathbf{S}$ stands for power spectral density function, k stands for “known”, which means the quantity is estimated based on measurements, u stands for “unknown” which means that the quantity will be simulated based on the measurements. f_m in equation (1) is discrete frequency.

The spectral matrix expressed by equation (1) is decomposed using the Cholesky decomposition to represent in the form of

$$\mathbf{S}(f_m) = \mathbf{H}(f_m)\mathbf{H}^{\dagger}(f_m) \quad (2)$$

where $\mathbf{H}^{\dagger}(f_m)$ is the Hermitian transpose of $\mathbf{H}(f_m)$, which has the form

$$\mathbf{H}(f_m) = \begin{bmatrix} \mathbf{H}_{kk}(f_m) & 0 \\ \mathbf{H}_{uk}(f_m) & \mathbf{H}_{uu}(f_m) \end{bmatrix} \qquad (3)$$

Based on the result of the Cholesky decomposition, the Fourier coefficients of the random process at the point of simulation over the wind turbine blade swept area where measurements are not available is obtained using the the Kriging method (Hoshiya 1995) as

$$\begin{aligned} \mathbf{V}_u(f_m) &= \mathbf{H}_{uk}(f_m)\,\mathbf{\Phi}_k(f_m) + \mathbf{H}_{uu}(f_m)\,\mathbf{\Phi}_u(f_m) \\ &= \mathbf{H}_{uk}(f_m)\,\mathbf{H}_{kk}^{-1}(f_m)\,\mathbf{V}_k(f_m) + \mathbf{H}_{uu}(f_m)\,\mathbf{\Phi}_u(f_m) \end{aligned} \qquad (4)$$

Using the inverse Fourier transform, the Fourier coefficients expressed by equation (4) can be used to obtain the time history of the realizations of the underlying Gaussian process of the wind turbulence at the points where measurements are not available. These realizations of the Gaussian processes are then translated into realization of the non-Gaussian processes using the Hermite transform (Winterstein 1988).

In the procedure described above, the spectral distortion method is used to force the spectra of the simulated random processes to match those of the target processes.

Using an example, Figure 1.3.2.16 illustrates the result of the conditional simulation. The black time histories are measured by the 200 m tower, while the coloured time histories are simulated based on the measurements.

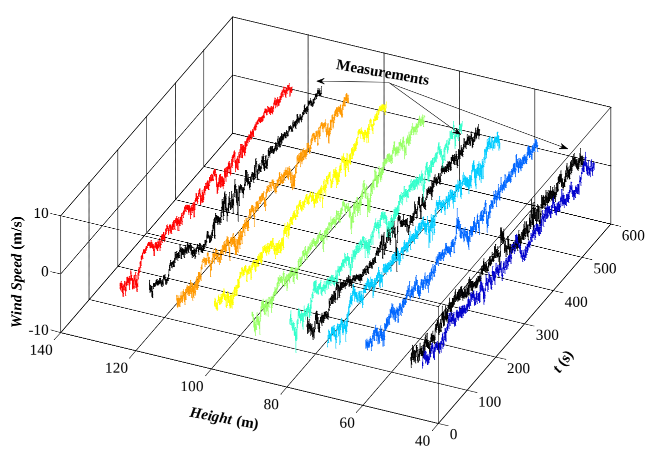

Figure 1.3.2.16. Example of conditional simulation of non-Gaussian time series.

1.3.2.2.c. Assessment of Wind Turbine Loading Based on Conditionally Simulated Inflow Fields.

The conditionally simulated inflow fields can be used to assess the loading on wind turbines subjected various types of wind. In this study, the FAST (short for Fatigue, Aerodynamics, Structures, Turbulence) developed by the National Renewable Energy Laboratory (NREL) in Golden, Colorado for modelling the dynamic response of horizontal axis wind turbines was used to evaluate the response of the 1.5 MW and 5 MW wind turbine models available from NREL. The following summarizes a number of representative results from this study.

The inflow fields used in this illustrative example have the mean and turbulence intensity profiles shown in Figure 1.3.2.17 and Figure 1.3.2.18 respectively, and Figure 1.3.2.19 shows the skewness and kurtosis profiles of the turbulence of the low-level-jet wind. The profiles for the low-level-jet event were estimated based on measurements by the 200 m tower, while those according to the IEC standard were generated by forcing the mean wind speed at the hub height of the turbine to be the same as that of the low-level-jet event. For reference purposes, a turbulence intensity profile is also generated based on the mean wind speed profile of the low-level-jet event and the specification by the IEC for the corresponding turbulence intensity profile, which mandates that the variance of the wind turbulence remains constant over the height of interest.

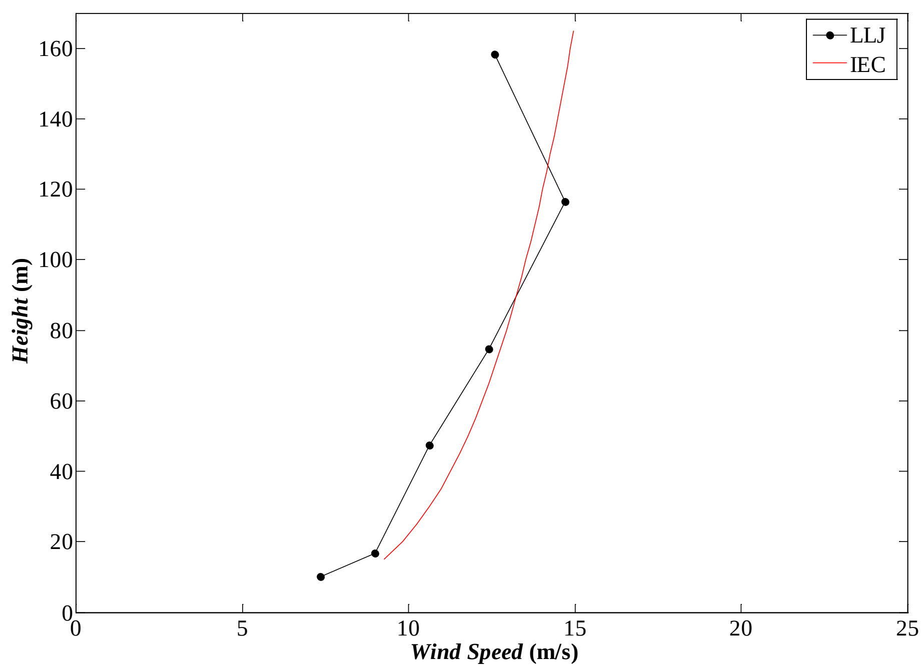

Figure 1.3.2.17. Measured mean wind speed profile for a low-level jet (LLJ) event and IEC normal wind profile with the same hub height wind speed used as targets for simulations.

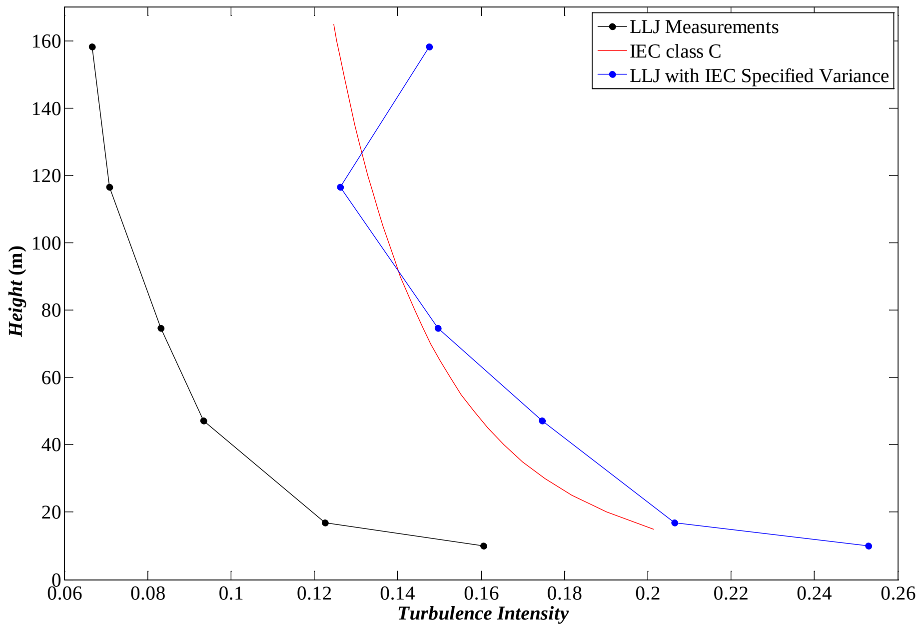

Figure 1.3.2.18. Target turbulence intensity profiles for the measured low-level jet event, the IEC class C specification, and the low-level jet using IEC class C specified variances.

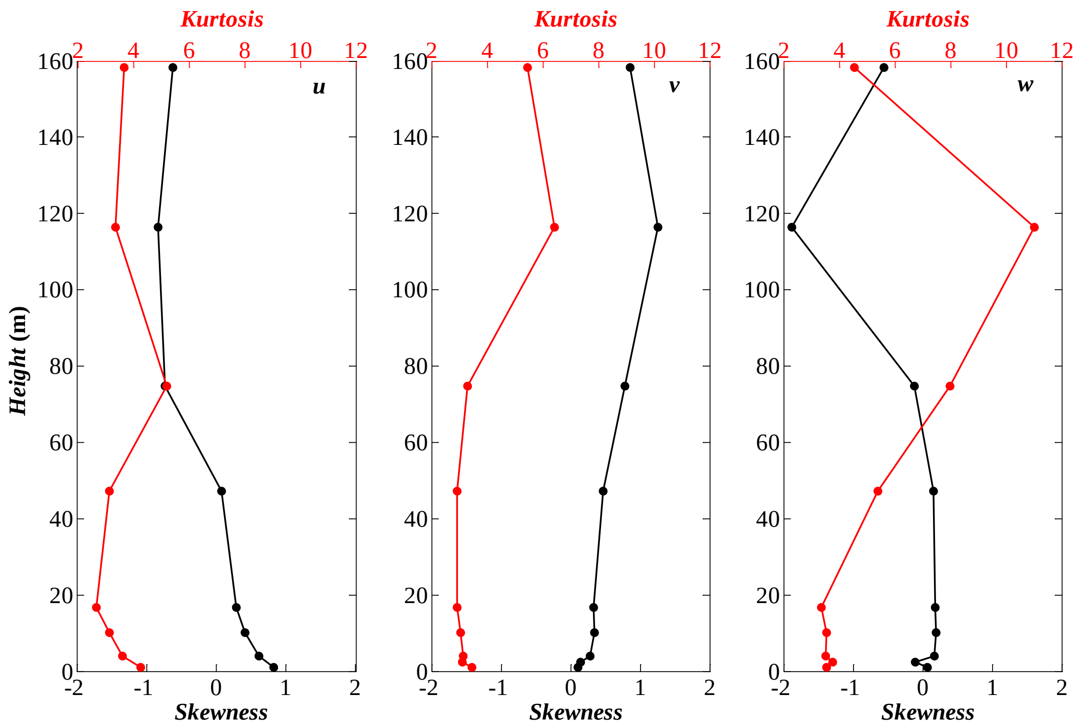

Figure 1.3.2.19. Skewness (black) and kurtosis (red) values for u (left), v (middle), and w (right) for the low-level jet event.

The turbulence intensity profile shown in Figure 1.3.2.18 of the low-level-jet event and the skewness and kurtosis profiles shown in Figure 1.3.2.19 were used in the conditional simulation that generated the turbulence field of the wind inflow field for the low-level-jet event. This turbulence field is superposed on the corresponding mean wind field obtained by interpolating the mean wind speed profiles shown in Figure 1.3.2.17 to obtain the total wind inflow wind field for this event for the two wind turbines. Combinations of the mean and turbulence profiles were also used to simulate other reference wind inflow fields.

Table 1.3.2.2 summarizes the cases of wind field simulation considered in this case study.

Table 1.3.2.2. Summary of the considered simulation sub-cases for case study.

Sub-case	**Wind Speed**	**Turbulence Intensity Type**	**Skewness and Kurtosis or Gaussian**
1	IEC profile	IEC class C specification	Gaussian
2	LLJ measured profile	Measured	Gaussian
3	LLJ measured profile	Measured	Measured, inhomogeneous
4	LLJ measured profile	Measured	Uniform (S, K) with $S > 0$
5	LLJ measured profile	Measured	Uniform (S, K) with $S < 0$
6	LLJ measured profile	IEC specified $\sigma_u, \sigma_v, \sigma_w$	Gaussian
7	LLJ measured profile	IEC specified $\sigma_u, \sigma_v, \sigma_w$	Measured, inhomogeneous
8	LLJ measured profile	IEC specified $\sigma_u, \sigma_v, \sigma_w$	Uniform (S, K) with $S > 0$
9	LLJ measured profile	IEC specified $\sigma_u, \sigma_v, \sigma_w$	Uniform (S, K) with $S < 0$

*S stands for skewness; K stands for kurtosis

Figure 1.3.2.20 and Figure 1.3.2.21 show the damage equivalent loads of the blades when the wind turbines were subjected to the simulated wind fields. It can be seen that due to the low turbulence intensities of the wind over the blade swept area in stable boundary layers, the loading on the blades are significantly lower than when the boundary layer is neutral, which is implied by the IEC standard. It also can be seen that if the turbulence intensities are artificially increased based on the IEC specification, the increased mean wind speed shear in stable boundary layers can result in increased loading on the blades.

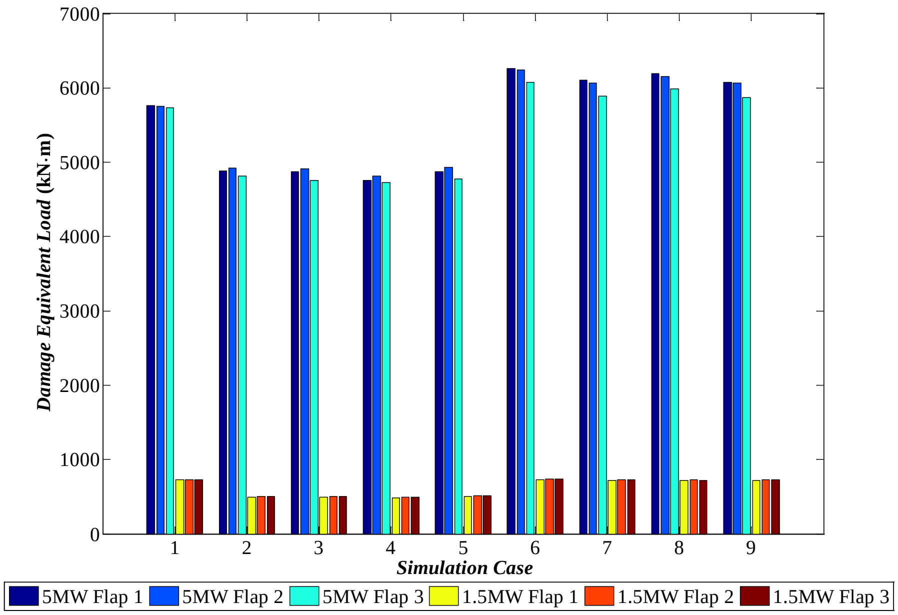

Figure 1.3.2.28. Damage equivalent flap-wise blade root moments obtained for the case study.

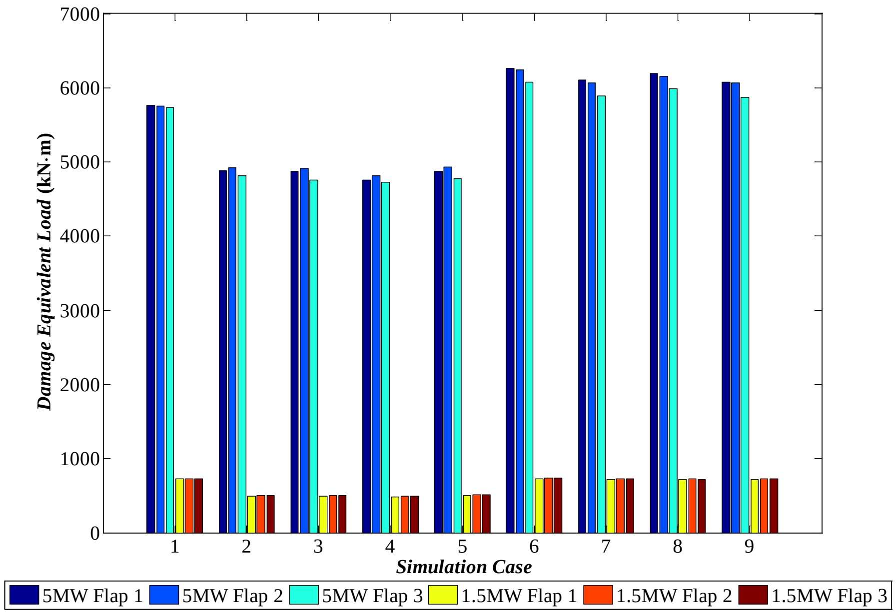

Figure 1.3.2.21. Damage equivalent flap-wise blade root moments obtained for the case study.

1.3.2.3. Conclusions.

The measurements by a 200 m meteorological tower were used to characterize wind in various conditions. It was revealed that the characteristics of wind in stable boundary layers can be significantly different from those of wind in unstable or neutral boundary layers. Specifically, winds in stable boundary layers can have pounced speed shear as well as significant direction veer over the height of utility-scale wind turbine. It is also found that the intensity, spectrum and probability distribution of the wind turbulence in stable boundary layers can also be significantly different from those of the turbulence in unstable or neutral boundary layers. In addition to characterization of stationary winds, the study also used methods based on the wavelet transform to characterize non-stationary thunderstorm winds. The evolutionary spectrum of the wind turbulence during thunderstorms can be used as a basis for simulation of this type of severe wind events.

Motivated by the observations made based on the measurements, a methodology was developed to conditionally simulate wind turbine inflow fields based on the measurements. The simulated wind fields were used as a basis for assessment of wind turbine loading. It is revealed that the loading of wind turbines in stable boundary layers is lower than in neutral boundary layers due to the comparatively low level of wind turbulence over the blade swept area of a wind turbine in stable boundary layers.

Subtask 1.4: Evaluate the Application of Asymmetric Spur Gears in Wind Turbine Designs.

1.4.1. Introduction.

The reliability evaluation of engineering systems occurs at two levels: individual performance criteria and overall system performance. These are referred to as component level and system-level reliability measures (Lewis 1983; Haldar and Mahadevan 2000). Accordingly, reliability of wind energy is highly dependent on the performance of all subsystems that constitute a wind turbine (WT), among them the gearbox, one of the heaviest and most expensive of the subsystems. It has been recorded that the wind industry has been suffering from early life gearbox failures since WT have been transformed from a backyard household size into utility scale energy generators. Musial et al. (2007) and Oyague (2009) indicated that for the same drivetrain architecture, the sector still faces the same gearbox problems as when the WT capacity was 500 to 1000kW. Ribrant and Bertling (2007) reported statistical data that show trends towards higher and even increasing failure frequency for larger turbines compared to small turbines, which have a decreasing failure rate over the operational years. Some reports by Puigcorbe and De-Beaumont (2010, Karpat and Ekware-Osire 2008, Lin and Kuang 2008) have indicated that WTG life is 3 to 7 years of operation as opposed to the expected 20 years. Moreover, several studies show that gearbox failure causes the highest down time of WTs and involves the most costly maintenance procedures (Oyague 2009; Ribrant and Bertling 2007; Puigcorde and De-Beaumont 2010).

Lately, there has been a lot of activity on the spur gears with asymmetric teeth. New gear designs are needed because of the increasing performance requirements, such as high load capacity, high endurance, low cost, long life, and high speed. For wind turbine gearboxes, the gears experience only uni-directional loading. In these instances, the geometry of the drive side does not have to be symmetric to the coast side. This allows for the designing of gears with asymmetric teeth. In previous studies related to bending stress and load capacity, high performance has been achieved for gears with asymmetric teeth. These gears provide flexibility to designers due to their non-standard design. If they are correctly designed, they can make important contributions to the improvement of designs of gears in the wind turbine industry (Karpat and Ekwaro-Osire 2008).

1.4.1.1. Technical Approach and Hypothesis.

Whereas there is literature on the theoretical studies on asymmetric gears, there are not experimental studies that are justified by theoretical results that the PI and co-PI are aware of. Thus, the research question for the proposed research is: Are gears with asymmetric teeth beneficial to wind turbines? To answer this research question, three specific aims are developed, namely, (1) design and construct a gear testbed, (2) conduct performance tests and analysis on asymmetric gears, and (3) conduct a dynamic theoretical analysis on asymmetric gears.

1.4.1.2. Experimental Methodology, Text Procedures and Characterization Methods.

A gear testbed was designed and constructed. Performance tests and analysis on asymmetric gears were conducted. A dynamic theoretical analysis on asymmetric gears was performed.

1.4.2. Discussion of Results.

After calculating and fine tuning the flex-to-flex contact parameters as presented above and applying them in the CPHS ADAMS 3D-contact MBD model, the tracks for steady state normal mesh force results in both R PP and SP PG contacts were searched in three different meshes of both R PP and SP PG pairs. The second sets of gears were preferred for relatively stable and smoother deterministic results. The normal force outputs of R PP2 and SP PG2 for nominal mean values of TISS = 37.539 kNm and NLSS = 21.457 rpm are presented in Figure 1.4.2.1. Figure 1.4.2.2 shows the variation of wear depths versus contact points during a mesh period for driving (pinion) and driven (gear) gears.

1.4.3. Conclusions.

For the presented compound planetary stage of the 1.5MW WTG, it has been demonstrated that system reliability to the tangential tooth-mesh-force is highly sensitive to loading conditions of the low speed shaft and the intermediate speed shaft. Hence, careful consideration of the variability of wind loading, and consequently the rotor speed and the generator torque, is critical for reliable system design.

A MATLAB-based virtual tool was constructed. This tool can be used to analyze wear behavior of asymmetric gears under dynamic load. Effects of gear parameters such as gear contact ratio, tooth height, mesh stiffness, pressure angles and temperature on tooth wear can also be examined. More experimental work has to be conducted after connection of two oscilloscopes.

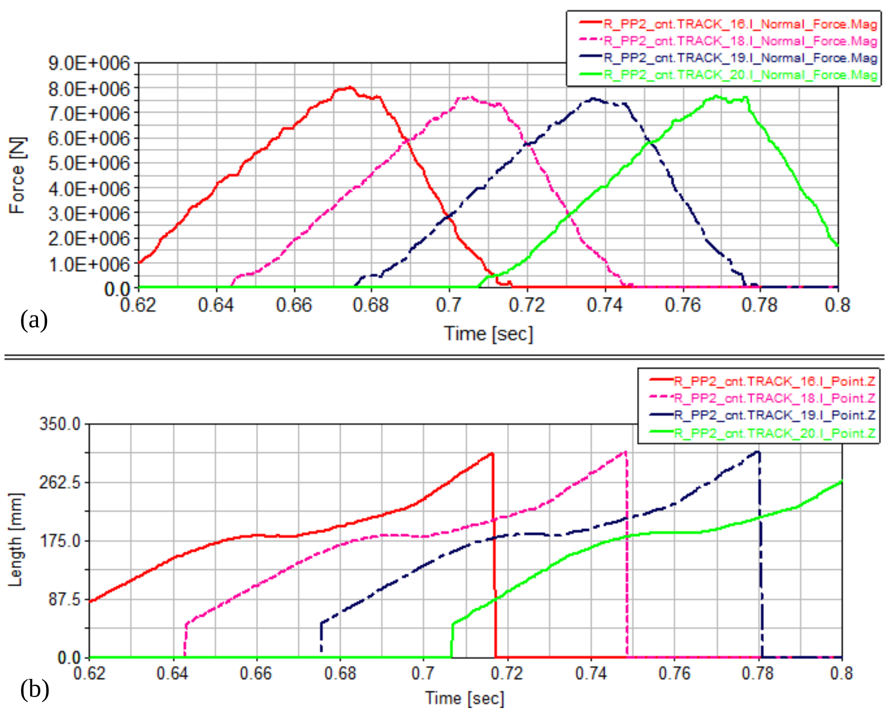

Figure 1.4.2.1. Second Ring vs. Planet-Pinion Tooth mesh: Tooth mesh force (b) Contact Incidence location along the face width.

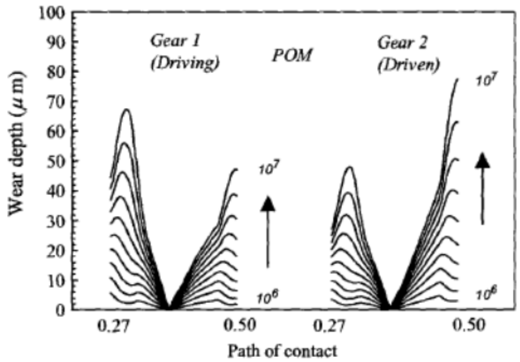

a)

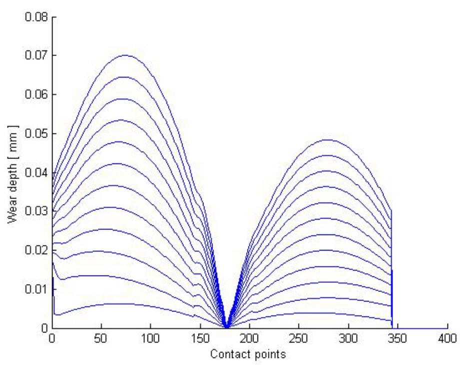

b)

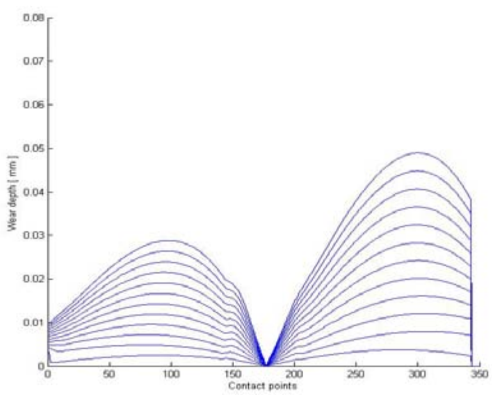

c)

Figure 1.4.2.2. Case 1-Variation of wear depth along a gear mesh with wear cycles for driving and driven gears: a) results obtained in Lin and Kuang (2008) b) driving gear c) driven gear (wear cycles $1x10^6$-$6x10^6$).

Subtask 1.5: Investigate the Stability of Turbines when they are connected to the Utility Grid.

1.5.1. Introduction.

Power demand has been increasing significantly over the past few years. Up until now, the major share of power has been supplied from conventional sources like nuclear, thermal, hydro etc, which are centralized. Most of the power coordination is also centralized through a SCADA system. The Northeastern blackout in 2003 is an example which exposes the sensitive nature of a centralized grid. An objective way for the conventional grid to move towards a smarter one is by decentralizing the grid, both in terms of supply as well as its control. The concept of microgrid (MG), where all the Distributed Generators (DGs) including the renewable energy sources can be operated and controlled at the distribution level itself, reduces the pressure on the main grid and hence the chance of a blackout is minimized. Some of the microsources are inverter interfaced, which makes the power control more flexible while others are directly connected. DC sources like PV's, SOFC's, storage etc are directly connected to the inverter while AC sources like Microturbine, flywheel etc are first rectified and then inverted to three-phase for grid connection. There are also some micro-sources like small hydro-power plants, fixed-speed wind turbine generators, diesel generators which are connected directly to the grid (Katiraei et al. 2008). MG's are interfaced to the main grid through a Point of Common Coupling (PCC) which consists of a Circuit-Breaker (CB). The CB is able to connect or disconnect the MG from the main grid by receiving trip signals from a local control unit. After islanding, reconnection of the microgrid with the main grid at the PCC is possible only when the voltage error is below 3%, frequency error is below 0.1Hz and phase angle error is below 100 (IEEE Application Guide Guide for IEEE Standard 1547). If these conditions are satisfied the resynchronization is possible with minimal transients. Figure 1.5.1.1 shows an example of a microgrid with various DGs along with loads connected within it.

The objective of the research was to develop a Low Voltage microgrid with various Distributed Energy Resources connected within it that would be connected to the main grid through a point of common coupling in Matlab/Simulink environment. The purpose of the research was to observe the transient operation of the microgrid during different modes. The project was completed 100% and defended as a thesis successfully. The complete research on the micro grid can be found in Manohar's thesis from TTU in 2011. A complete literature review was conducted for this research and the results are given in the list of references.

1.5.2. Results and Discussion.

The Department of Energy defines a microgrid as "a combined energy system consisting of organized loads as an integrated system with distributed energy resources which can operate in parallel as well as in islanded mode". When power is generated at huge power plants, the voltage is stepped up and transmitted through long distances to reach the distribution systems where the voltage is stepped down to meet the power demand at the load sites. The distribution system is a complex network hence its control becomes very difficult. This gave the idea of breaking down the distributed system into separate individual entities where management of these entities becomes much simpler. These separate entities or Microgrids are dedicated to a particular area and are able to separate themselves from the main grid and continue normal operation. The reason for disconnection could be due to a voltage collapse, faults or by purpose for maintenance (Lasseter 2005). This increases the local reliability due to sustained power supply (Lasseter and Paigi 2004). The control of the microsources within the microgrid depends upon the required functions and general setup of the AC system. The main control functions of a microgrid control are voltage and frequency control and/or Active Power/Reactive Power control. The categorization of the different control functions with their division into grid forming and grid following controls are shown in Table 1.5.1.1.

Table 1.5.1.1. Classification of control strategies for Inverter interfaced microsources.

Control Method	Grid-Following	Grid-Forming
Non-interactive	Power export (with/without MPPT)	Voltage and frequency control
Interactive	Power dispatch Real and reactive power support	Load sharing (droop control)

The controls are further divided into interactive and non-interactive strategies. The grid following control technique is utilized only when there is no reference voltage and frequency available at the PCC. Within the grid following control strategy, the grid non-interactive strategy is utilized to control the microsources that are independently controlled without the consideration of the other microsources or load. An example of this could be a PV array based on Maximum Power Point Tracking (MPPT) control where the MPPT dispatches the reference power settings based on the Maximum Power Point. Another kind is the grid interactive strategy where the setpoints are dispatched by a local control units based on the load demands and ratings of the microsource.

The grid-forming strategy is applied during the islanded mode. In the non-interactive strategy, there is a single microsource which covers up the power imbalance while simultaneously stabilizing the voltage and frequency, while in the interactive strategy, there are several microsources that share the load as well as its changes based on droop control by changing the voltage and frequency of the microsources.

Figure 1.5.2.1 shows the overall LV microgrid as developed in Matlab/Simulink. The microsources are located at different strategic locations separated by line impedances and transformers.

Two case studies were conducted on the micro grid. The first case study was done when the islanding condition is considered with the storage device acting as the reference voltage and frequency source. When the micro grid shifts from grid connected mode to islanded mode, the storage device moves from P-Q control to V/f control strategy. The storage device now acts like a power balancer by either producing more power or by absorbing the excess power from the other micro sources when certain load conditions are considered. When the power flows from the storage device to the rest of the micro grid the storage device discharges, while when power flows into the storage device it starts charging. The charging and discharging characters are not shown as the storage device is considered a DC voltage source at a constant voltage value. Also, for this case, it is assumed that the storage device has enough power capacity to be able to cover up the power imbalance for as long as the micro grid is in islanded mode. Figure 1.5.2.2 shows the active and reactive power flow between the main grid and the micro grid. Between time t=0 to t= 30 sec, the micro grid is in islanded mode and the power flow between the main grid and the micro grid reduces to zero.

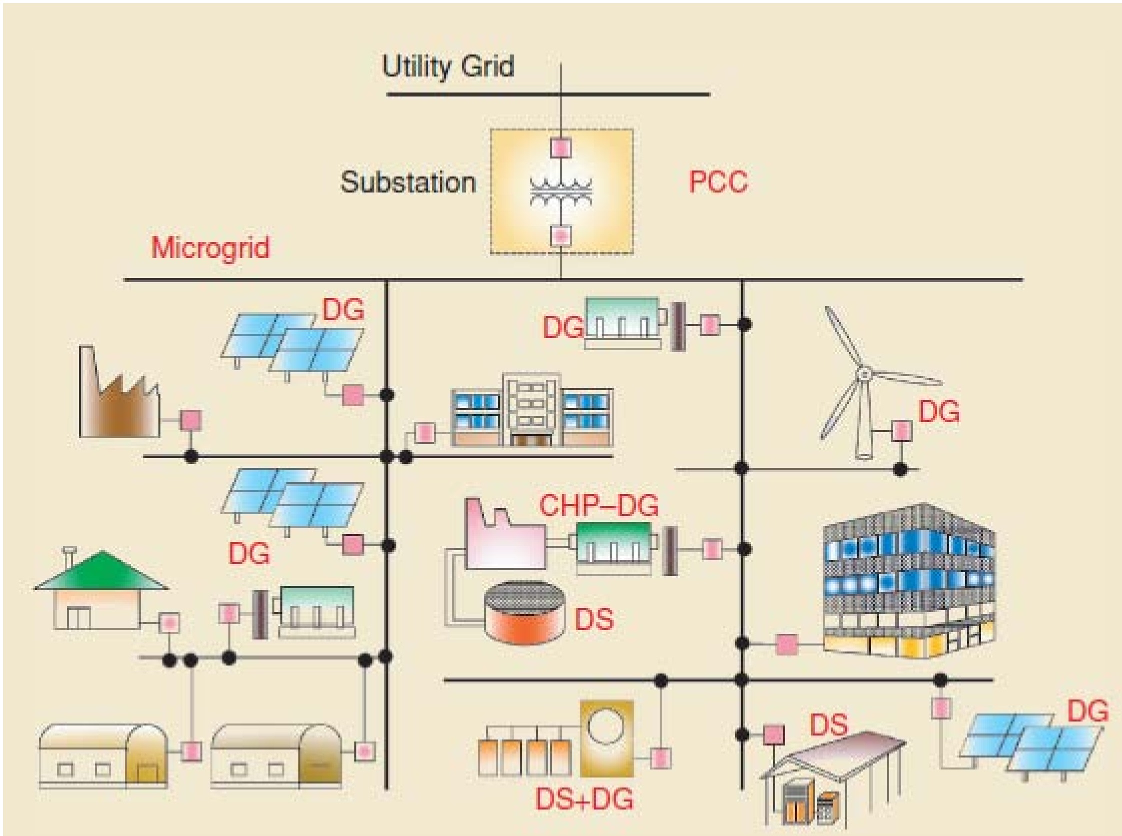

Figure 1.5.1.1. An example of a microgrid (Katiraei et al. 2008)

Case 2 is when the microgrid moves from grid connected to island mode -- there is a single power source which moves from PQ control to V/f control mode (which in this case is a single storage device). All other micro sources are PQ controlled while the storage device operating with V/f control meets the power imbalance. At times, the power to be drawn from the storage device exceeds its limits. Figure 1.5.2.3 shows the power flow from the inverter interfaced storage device. When the storage device is grid connected, the active and reactive flow is zero. When in islanded mode, the storage device picks up the excess load to be met while maintaining constant voltage and frequency. The limit for the active and reactive power to be transferred from the main storage device is known beforehand. If any of the limits are exceeded, the algorithm takes one sec to react so as to make sure the excess power demand is not due to any transients.

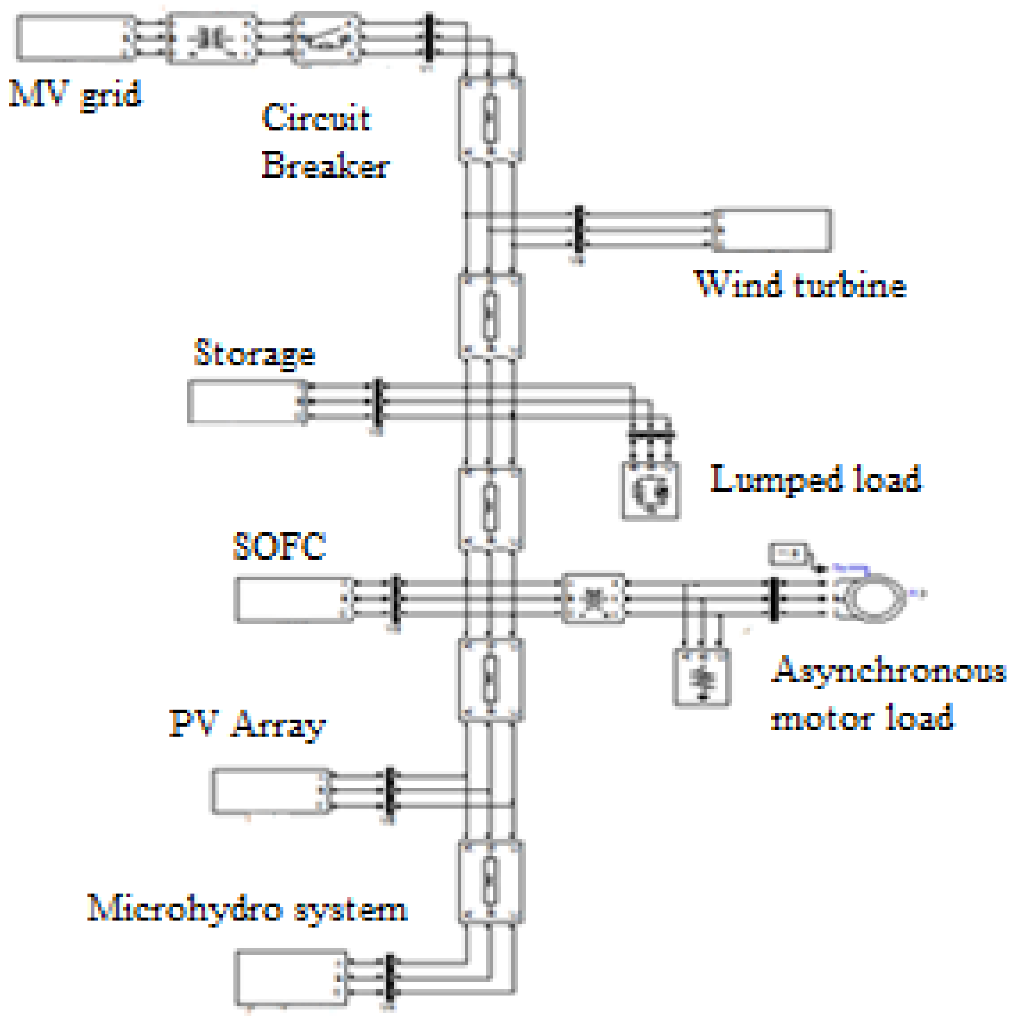

Figure 1.5.2.1. The Micro Grid network developed in Matlab/Simulink.

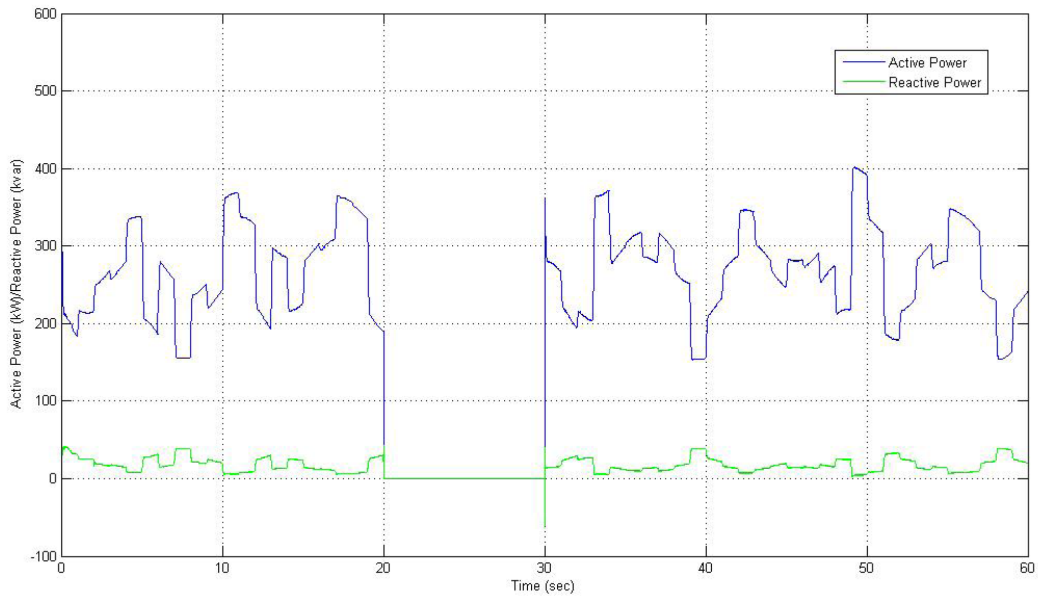

Figure 1.5.2.2. Main grid power flow (Manohar 2011).

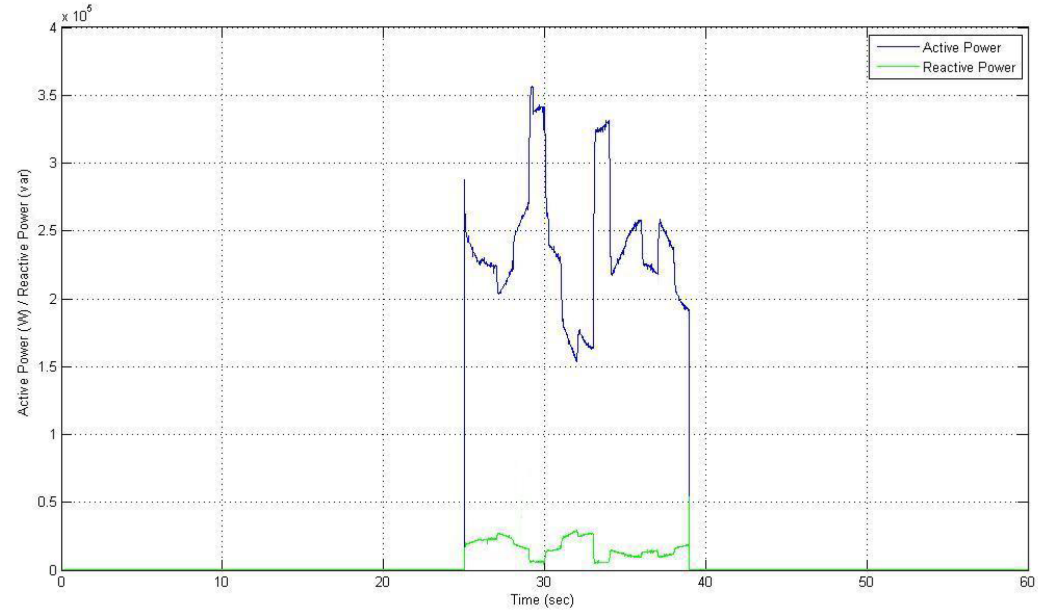

Figure 1.5.2.3. Main Power Device Power Flow (Manohar 2011).

1.5.3. Conclusion.

In the research conducted, a number of Distributed Generators were developed in a microgrid. Their dynamic and steady state behaviours were examined in a Matlab/Simulink simulation environment. Simulations were carried out to examine the transients when the microgrid changes from grid connected mode to islanded mode and then back to grid connected mode. The two control modes used in this paper were PQ control and V/f control. A dedicated storage device with enough power capacity was assumed, which helped to smooth out the power imbalance during the islanded mode of operation. Whenever the power rating for the main storage was exceeded during some conditions, the reserve storage device was set to produce power until the power rating for the main storage device was brought within limits. Results indicated that all DGs (apart from the storage device) operated in a regular way, while the storage device experienced a change in its operation during the islanding mode to maintain the pre-islanded voltage and frequency values.

Subtask 1.6: Investigate Pitch Control Technologies and their Ability to Impact Turbine Loading and Performance Optimization.

NWI Ph.D. student Richard P. Walker is close to completing his dissertation on this subtask. While initially targeting pitch related control and technologies, this work has evolved to focus on yaw errors and their impact on turbine efficiency. After some of the initial radar related complex flow measurements revealed the vast turbine to turbine interaction within a wind farm, researchers became interested in techniques to “steer” or deflect wakes away from downstream machines. While TTU continues to learn about this systems level control opportunity, this subtask evolved to examine the impact of yaw error (relative to the true inflow direction) on turbine efficiency.

1.6.1. Introduction.

Wind energy generation has grown rapidly in the United States over the last seven years, and in 2012 it was the largest source of new electric generation in the U.S. However, its primary competition in the electricity market, natural gas-fired generation, has benefited from low natural gas prices and significant efficiency improvements. In addition, owners of many wind projects are finding that actual energy production from projects now in operation is consistently below the Annual Energy Production (AEP) estimates made prior to the construction of the projects. Owners of underperforming projects are now trying to determine how best to improve the efficiency of existing projects and how to improve the accuracy of energy production estimates being made for planned wind projects.

The goal of this research project is to identify the most likely and logical areas or methods for improving the efficiency, reliability, and overall cost effectiveness of wind energy. Topics to be evaluated as part of this analysis include:

A. Identifying the key “drivers” or variables having the greatest impact on the economics of wind energy,
B. Improving the understanding of wind characteristics in the Great Plains region of the United States, particularly in regard to vertical and directional wind shear and their impact on the economics of wind generation,
C. Increasing the understanding of the effect of turbine misalignment (or yaw error) has on turbine performance,
D. Evaluating the use of state-of-the-art wind measurement technologies such as lidar for purposes including (1) obtaining data at higher elevations above groundline during the site assessment process and (2) obtaining anticipatory turbine inflow wind data that can be integrated with wind turbine control protocols for purposes of optimizing energy production and reducing unnecessary forces on operational wind turbines, including an assessment of whether such strategies can be cost effective.

1.6.1.1. The Potential Impact of Yaw Error on Energy Production.

Due to the highly stochastic nature of wind, the use of after-the-fact wind data to control yaw direction and pitch angle of a turbine will invariably result in some degree of error. As soon as the turbine controller orients the rotor in a direction perpendicular to the average wind direction for the previous averaging period, the wind direction will change. Sometimes, the degree of change is inconsequential, and at other times it can be significant. Most turbines have a range of averaging times and yaw error tolerance which determines how often the turbines will yaw as a result of changes in wind direction. Yaw error tolerance refers to the minimum differential between current turbine direction and optimum turbine direction before the controller instructs the turbine to yaw, and occurs when the turbine rotor is not perpendicular to the wind direction. This can result in a reduction to energy captured by the rotor, or reduced efficiency and larger fatigue loads on the turbine since the blades will have a tendency to bend back and forth with each turn of the rotor.

A survey of wind energy industry representatives was conducted as part of the research for this project, and one of the questions asked addressed averaging time and yaw error tolerance. Shown below are typical combinations of averaging time and tolerance bands mentioned in their responses. (See Table 1.6.1.1.)

Table 1.6.1.1. Combinations of Averaging Time and Minimum Yaw Error to Activate Turbine Yawing Mentioned in Survey of Wind Industry Representatives.

Data Averaging Period	Minimum Direction Change Before Turbine Yawing
10 minutes	± 3 degrees
10 minutes	± 3.5 degrees
10 minutes	± 5 degrees
5 minutes	± 2 degrees
5 minutes	± 3 degrees
5 minutes	± 3.5 degrees

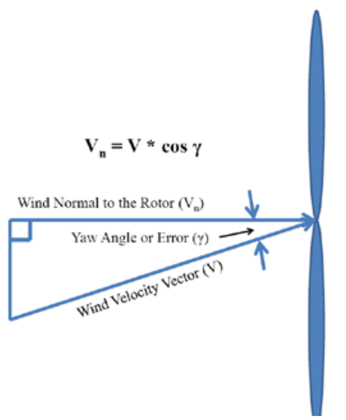

Figure 1.6.1.1. Illustration of Cosine Cubed Method for Estimating Yaw Error Effect.

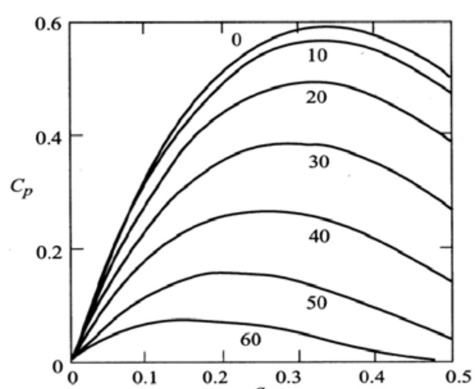

Figure 1.6.1.2. Estimated Reduction of Coefficient of Power as a Function of Increasing Yaw Error; (Source: Figure 3.48 from 'Wind Energy Handbook" by Burton et al. 2011.)

One of the most common methods of estimating yaw error's effect on turbine efficiency is referred to as the "cosine cubed" method. As seen in Figure 1.6.1.1, when wind is not perpendicular to the rotor, the vector normal to the rotor can be calculated by multiplying the wind speed times the cosine of the yaw angle or error. Since power output is a function of the cube of the wind speed, the expected power production is reduced by the cube of cosine γ. Note that yaw error would need to exceed 5 degrees before efficiency losses reach even 1% based on the Cosine Cubed methodology.

The "Wind Energy Handbook" (Burton et al. 2011) addresses the potential impact of yaw error on the efficiency of wind generation. Figure 1.6.1.2 shows Burton's estimated reduction to the power coefficient (Cp) at increasing amounts of yaw misalignment. While Burton notes that the "$\cos^3 \gamma$" rule is commonly adopted for power assessment in yawed flow, he also raises the valid question of "is it legitimate to apply the momentum theory in the above manner to the yawed rotor?" Burton goes on to state: "Transverse pressure gradients which cause the wake to skew sideways may well also contribute to the net force on the flow in the axial direction, influencing the axial induced velocity. The above analysis might be satisfactory for determining the average axial induced velocity but there is even less justification to apply the momentum theory to each blade element position than there is in the non-yawed case. If a theory is going to be of any use in design, it must be capable of determining the induced velocity at each blade element position to a satisfactory accuracy. The satisfactory calculation of blade forces is as important as the estimation of power."

As part of the research conducted for his dissertation, Andrew Swift evaluated the impact of yawed flow in his work entitled "The Effects of Yawed Flow on Wind Turbine Rotors" (Swift 1980). This included the following observations. Note that CT is the Rotor Thrust Coefficient and CQ is the Rotor Torque Coefficient.

A. "The near constant relation between C_T and C_Q with yaw angle suggests feasibility of a wind turbine system that limits power output to a constant value with a thrust limiting device that either yaws the rotor about a vertical axis or pitches the rotor about a horizontal axis, above rated thrust."

B. "Another interesting result is that the theory predicts that under certain conditions there may be more power available in yawed operation than in axial flow conditions."

C. "Although the phenomenon of increased power with yaw angle appears to be a moderate effect from the viewpoint of obtaining extra power from a given wind machine, and may not occur under certain operating conditions, the ability to predict and be aware of the effect is important in the consideration of yaw as a method of power control."

Another organization that has evaluated the effect of yaw misalignment, or skew airflow, on the efficiency of wind generation is Risø DTU, the Danish National Laboratory for Sustainable Energy at the Technical University of Denmark (DTU). A report titled "Wind Turbine Power Performance Verification in Complex Terrain and Wind Farms" (Pederson 2002) references a study by H. S. Madsen examining the effect that various degrees of yaw error had on power output of a 75 kW wind turbine compared to power reduction predicted by various aerodynamic codes. As shown in Figure 1.6.1.3, which came from

Pedersen's report, Madsen's work indicated that the square of the cosine of the yaw error ($\cos^2$) most closely predicted the decline in power output.

One interesting thing to note in Figure 1.6.1.3 is that Madsen's experimental results show a slight increase in power production at a yaw angle of about 2 to 3°, which supports Swift's finding that under certain conditions, there may be more power available in yawed operation than in axial flow conditions.

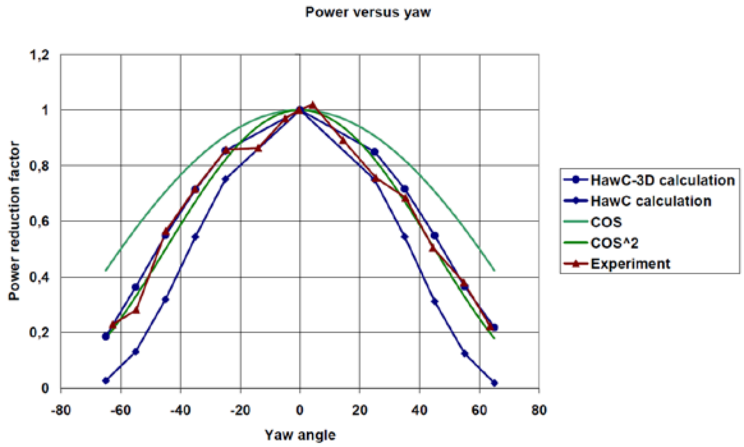

Figure 1.6.1.3. Comparing Calculated Power Losses as a Function of Yaw Angle to Experimental Results. (Source: Figure 6.1 from 'Wind Turbine Power Performance Verification in Complex Terrain and Wind Farms' (Pederson)).

Estimated efficiency losses associated with increasing degrees of yaw error were calculated using both the $\cos^3$ relationship and the $\cos^2$ relationship suggested by Madsen and Pedersen. Table 1.6.1.2 compares estimated efficiency reductions predicted by the $\cos^2$ and $\cos^3$ methods at various levels of yaw angle. Since the kinetic energy in the turbine's rotor should serve to reduce the impact of short-term gusts of differing direction, and given that Madsen's work using an actual turbine to compare the impact of yaw misalignment to various empirical methods of estimating the impact, it seems logical that the cosine² method is the best method for approximating losses due to yaw misalignment. This would also be the more conservative of the two when estimating the potential gain from using technologies such as lidar for anticipatory data acquisition and real-time turbine control.

Table 1.6.1.2. Comparing Estimated Efficiency Losses Based on the Square of the Cosine of Yaw Angle vs. the Cube of the Cosine of Yaw Angle.

Yaw Error	Losses Predicted by Cosine^2 Method	Losses Predicted by Cosine^3 Method
5^{o}	0.8%	1.1%
10^{o}	3.0%	4.5%
15^{o}	6.7%	9.9%
20^{o}	11.7%	17.0%

1.6.2. Results and Discussion.

1.6.2.1. Use of One Second Data to Evaluate the Impact of Averaging Period and Yaw Differential Toleration for Turbine Yaw Operations.

Since the frequency with which a wind turbine changes direction varies as a function of averaging times (typically either 5 minutes or 10 minutes) and the range of yaw error tolerance (such as ± 4°) which are used by the controller to determine if the yaw motors should be used to change the direction of the turbine rotor. These settings may depend upon the manufacturer and model of the turbine or upon the wind project operator's desired settings. Based on the prevailing assumption that yaw error leads to reduced efficiency of wind turbines, one could reasonably assume that a constantly-yawing turbine would be more efficient than one that only periodically yaws. One then should ask how much efficiency improvement justifies the additional costs of real-time turbine control, wear-and-tear on yaw motors, and increases in the cumulative gyroscopic loads that the turbine would be exposed to over its lifetime. Since the vast majority of meteorological towers used in the wind energy industry average and store data in 10-minute increments, data from such towers is of little use in determining the potential benefits of shorter averaging periods for yaw control. However, at Texas Tech's Great Plains Wind Test Facility, a 200-m tower is heavily instrumented at 10 different levels and collects and stores wind data at a frequency of 20 Hertz.

As part of the research for this project, data from this 200 m tower has been used to examine the potential benefits of more frequent yawing by comparing the average yaw error for the following combinations of averaging time and yaw differential tolerance, as well as the estimated efficiency loss assuming both the $\cos^2$ and $\cos^3$ relationships between yaw error and efficiency reduction. This exercise also helps with estimating the potential benefits of real-time turbine control using advanced wind measurement methods such as nacelle-mounted lidars integrated with the turbine controller. Essentially, a 1 second averaging period and a 0° tolerance band would represent a turbine that is always aligned with the wind, or constantly yawing. While a constantly-yawing turbine may improve overall efficiency, there are barriers to a constantly yawing turbine such as increased wear-and-tear on yaw motors and increased cumulative gyroscopic loading associated with yawing. Combinations of averaging period and yaw differential tolerance evaluate ranged from 10 minute averages with ± 4° of yaw differential tolerance to 1 second data with 0° of yaw differential tolerance, with the last essential representing a turbine that is always "perfectly aligned."

1.6.2.1.a. Effect of Different Yaw Differential Tolerance Ranges.

Analysis of data from a moderate wind day (August 26, 2011) indicated that use of an 8° tolerance band (i.e., ± 4°) and a 10-minute averaging period would result in an average yaw error of 10.7° throughout the course of the day, with an estimated 8.8% loss in efficiency based on the $\cos^3$ relationship, or only 6.3% based on the $\cos^2$ relationship. Reducing the tolerance band to 4° (i.e., ± 2°) reduces average yaw error to 10.2°, and estimated losses of 8.0% loss in efficiency based on the $\cos^3$ relationship, or only 5.7% based on the $\cos^2$ relationship. Reducing the tolerance band even further to 0° would essentially mean that the turbine yaws after every 10-minute averaging period, even when there is only a very small differential between the existing turbine direction and the wind direction for the previous 10-minute period. This again slightly reduces yaw error to an average of 9.6°, and estimated losses of 7.5% loss in efficiency based on the $\cos^3$ relationship, or only 5.3% based on the $\cos^2$ relationship. This would indicate that more frequent yawing associated with reductions to the tolerance band can have some beneficial effect, but not a huge impact.

1.6.2.1.b. Effect of Different Averaging Times for Turbine Yaw Operations.

In addition to evaluating the potential benefit of reducing the tolerance band, this research also considered the benefit of shortening the averaging time. Different averaging time periods considered included 10-minutes, 5-minutes, 2-minutes, 1-minute, 30-seconds, 10-seconds, and 1-second. A combination of 1-second averaging time period and a 0° tolerance band would approximate near-perfect alignment of the turbine at all times. This analysis indicated that use of an 8° tolerance band (i.e., ± 4°) and a 10-second averaging period would reduce average yaw error of 4.6° throughout the course of the day, with an estimated 2.4% loss in efficiency based on the $\cos^3$ relationship, or only 1.5% based on the $\cos^2$ relationship. Reducing the tolerance band to 4° (i.e., ± 2°) reduces average yaw error even further to 4.2°, with estimated losses of 2.3% loss in efficiency based on the $\cos^3$ relationship, or only 1.5% based on the $\cos^2$ relationship. Reducing the tolerance band even further to 0° and using a 10-second averaging period would essentially mean that the turbine is almost continuously yawing. This again slightly reduces yaw error to an average of 3.9°, and estimated losses of 2.1% loss in efficiency based on the $\cos^3$ relationship, or only 1.4% based on the $\cos^2$ relationship. This would indicate that more frequent yawing associated with use of shorting averaging periods may be more effective for improving efficiency than reductions to the tolerance band.

Of the days evaluated, August 26, 2011 was determined to be the day having the greatest amounted of average yaw error from among those days evaluated, and it was also the least windy day of those evaluated, with winds averaging about 9.01 meters per second for the day at 116 meters above ground. Data from other days, all with higher average wind speeds, showed much lower levels of average yaw error and efficiency reduction, suggesting that constantly yawing turbines would be most beneficial during periods of low wind speeds. In addition, turbines typically reach rated output at somewhere between 12 to 15 meters per second, and depending upon the mechanism used to limit output to rated power, reducing yaw error may not result in any additional power output at higher wind speeds. Furthermore, since turbines shut down in high wind speeds (typically somewhere around 25 mps), reducing yaw error in this range of wind speeds is meaningless unless future turbine designs incorporate concepts such as predictive wind measurement (using lidars or other advanced technologies) and advanced blade design.

1.6.2.1.c. Impact of Reducing Averaging Times and Differential Tolerance Range for Turbine Yaw Operations.

Table 1.6.2.1 provides a summary of the results from several days of this analysis. Of the days evaluated, the maximum potential improvement would appear to be 8.6% based on the cosine^3 method for estimating inefficiency due to yaw misalignment, or 6.1% based on the more conservative cosine^2 method. Also note that these results indicate a trend showing less benefit on days having higher average wind speeds.

Table1.6.2.1. Summary of Results Showing Maximum Potential Benefits of Constantly Yawing Turbines.

Date	Average Wind Speed (mps)	Averaging Period	Average Yaw Error (degrees)	Reduced Efficiency Based on $\cos^3$ of Yaw Error	Reduced Efficiency Based on $\cos^2$ of Yaw Error	Average Yaw Error (degrees)	Reduced Efficiency Based on $\cos^3$ of Yaw Error	Reduced Efficiency Based on $\cos^2$ of Yaw Error	Maximum Potential Improvement Based on $\cos^3$	Maximum Potential Improvement Based on $\cos^2$
			± 4° Differential to Activate Yaw			± 0° Differential to Activate Yaw				
26-Aug-11	9.01	10 min.	10.73	8.82%	6.31%	9.59	7.52%	5.31%		
	9.01	1 sec.	2.09	0.40%	0.27%	1.25	0.24%	0.16%	8.58%	6.14%
7-Aug-11	14.32	10 min.	6.55	4.59%	3.26%	6.20	4.34%	3.10%		
	14.32	1 sec.	1.82	0.27%	0.18%	0.92	0.12%	0.08%	4.47%	3.18%
28-Jul-11	16.64	10 min.	5.67	3.61%	2.53%	5.22	3.33%	2.35%		
	16.64	1 sec.	1.73	0.24%	0.16%	0.73	0.09%	0.06%	3.52%	2.47%
1-Jun-11	17.47	10 min.	6.24	3.68%	2.57%	5.97	3.49%	2.44%		
	17.47	1 sec.	1.88	0.28%	0.19%	1.03	0.13%	0.09%	3.55%	2.48%
9-May-11	20.07	10 min.	6.70	4.41%	3.18%	6.25	4.07%	2.95%		
	20.07	1 sec.	1.89	0.29%	0.19%	1.07	0.14%	0.09%	4.27%	3.08%

1.6.2.2. Analyzing the Impact of Yaw Error Based on Actual Turbine Data.

TTU is involved in the testing and certification of a utility-scale wind turbine at its Great Plains Wind Test Facility, and has installed a hub-height met mast complete with multiple level 3-cup anemometers and directional wind vanes. One-second data was collected from both the test turbine and the met mast, and this researcher was given access to data from 7 days within a three-month period of time. The researcher's analysis of the data focused upon determining if there was a noticeable impact of yaw error or turbine misalignment on energy production, particularly in Region II-a of the power curve where the turbine blades are oriented at the full angle of attack and the turbine is producing at less than rated power. Examination of data from the turbine and met mast indicates that Region II-a lies between a low of 4 meters per second wind speed and a high of 10 meters per second, so other wind speeds were excluded from the analysis focused on the effect of yaw error on energy production. The researcher has used a variable he calls "Coefficient of Performance Net of Losses" (or "CPNL" for purposes of this paper) as the indicator of turbine efficiency at various levels of yaw error as an indicator of the impact of yaw error on turbine performance. Thus, given the data available from the test turbine and the associated meteorological tower, one can determine an indicator of efficiency, CPNL, in the following manner:

$$CPNL = C_p \, \varepsilon_{Gen} \, \varepsilon_{GB} = Power \; / \; (0.5 \bullet \rho \bullet V^3 \bullet (\pi d^2/4)) \qquad (1)$$

where Cp = Coefficient of Performance, ε_{Gen} = generator efficiency, ε_{GB} = gearbox efficiency, ρ = air density in kg/m^3, V = wind speed in meters per second, and d = the turbine's rotor diameter in meters.

Since wind direction and turbine direction data are available, values for yaw error at the various time averaging periods can be calculated, and average values of CPNL can be associated with various amounts of yaw error to determine how yaw error affects turbine efficiency. Sea level equivalent wind speeds were calculated for each one-second measurement to remove the effect of varying air density on actual energy production, and values for average wind direction, average power generation, and average yaw error for each average time increment of interest (i.e., 10 seconds, 30 seconds, 1 minute, 2 minutes, 5 minutes, and 10 minutes) were also calculated.

Following Figure 1.6.2.1 is an example of a plot of CPNL vs. yaw error for one-minute rolling averages of the wind data. Note that the vast majority of observations occurred within the range of ± 10° of yaw error, so inferences based on results outside of that range are based on very limited data and thus may not be valid. However, within the range of ± 10° of yaw error, it appears that yaw error has little impact on the efficiency of the turbine. Note that some additional field verification of the directional information from the test turbine and the meteorological tower is needed to ensure that both sets of information are being reported consistently.

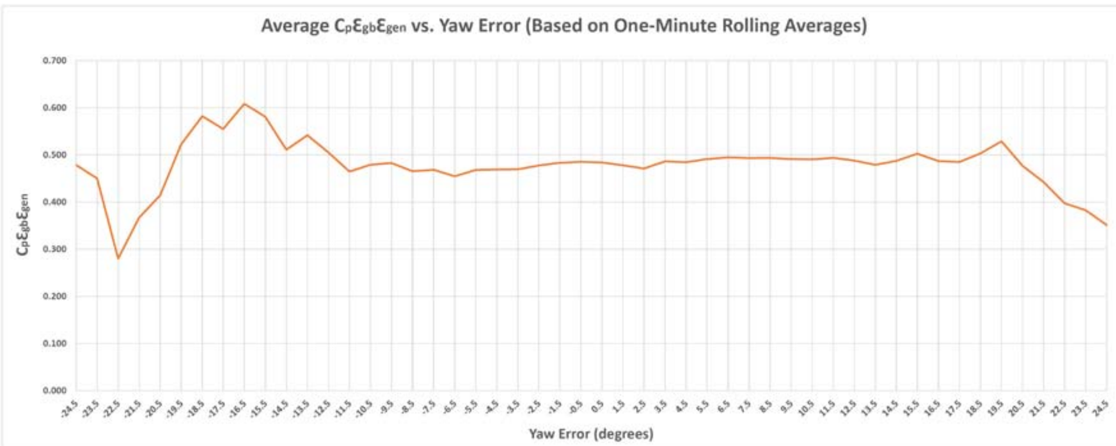

Figure 1.6.2.1. Average CPNL vs. Yaw Error Based on One-Minute Rolling Averages.

Another method used to evaluate the impact of yaw error on energy production was to plot the predicted energy production at various wind speeds against actual production for various levels of yaw error. Following Figure 1.6.2.3 are examples of such plots, with the first showing the predicted production versus individual data points and the second showing predicted production versus a trendline determined for actual production. As one can see in Figure 1.6.2.2, for the yaw error in the range of +6° to +10°, yaw error seems to have little effect on energy production.

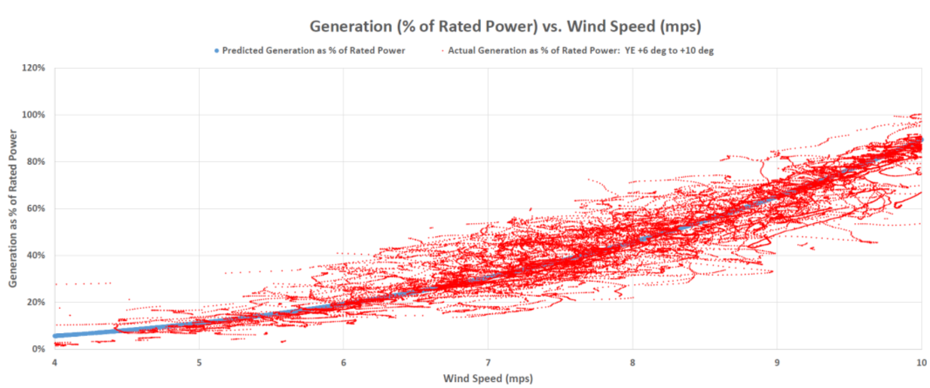

Figure 1.6.2.2. Predicted Generation vs. Actual Generation for One-Minute Rolling Average Data With Yaw Error Between +6° and +10°.

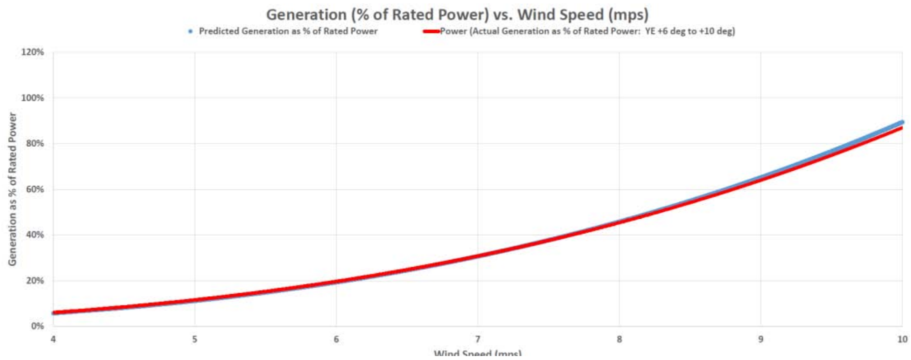

Figure 1.6.2.3. Predicted Generation vs. Actual Generation Trendline for One-Minute Rolling Average Data With Yaw Error Between +6° and +10°.

1.6.3. Conclusions.

While the analysis of the data from the test turbine and its associated meteorological tower is ongoing, the review of the results obtained to date indicate that justifying the cost of anticipatory wind data collection via the use of lidar cannot be justified solely upon additional energy production resulting from a reduction in yaw error. Perhaps a simpler way to achieve a reduction in average yaw error would be to reduce the averaging time and yaw differential tolerance used to control turbines. It is also likely that instrumentation error (in anemometers and wind vanes) may contribute to yaw error if the instruments are not well maintained and calibrated. The increasing use of sonic anemometers on wind turbine models may help reduce some of these issues.

Subtask 1.7: Investigate Turbine Wakes using Analytical Models.

1.7.1. Introduction.

Wind turbines may lose 20-30% of their power due to wake effects (Mechali et al. 2006, Herbert et al. 2007). The aerodynamics of wind turbines are yet to be fully understood, at least to the extent which would enable reliable prediction of power output (Hansen et al. 2006). When one adds the complexity and evolution of the inflow, the challenge becomes even more difficult. In 2003, Vermeer et al. reviewed experimental and numerical studies on wind turbine aerodynamics in both near- and far-wakes. Sanderse followed this study with his review of the numerical modeling of wakes (2009) and in 2010, Sumner et al. reviewed the development of computational fluid dynamics (CFD) in wind energy. CFD methods based on the Navier-Stokes equations can yield accurate results, although these methods can be computationally expensive when used to numerically study far-wakes since the wakes can be unsteady and have unpredictable turbulence (Sanderse 2009, Sumner et al. 2010).

To further understand the behavior of the far-wake behind a wind turbine with/without swirl (especially wake width predictions), TTU researchers have proposed a numerical model of the far-wake development using the boundary layer theory and similarity assumptions. To solve turbulent quantities, two turbulence options (the standard k-ε and Reynolds Stress (RS) transport models) were used. The computational code EXPRESS (which was originally composed for two-dimensional turbulent boundary layer flows) was revised and used to perform the simulations. In EXPRESS, self-similarity is assumed in the far wake region and computation is advanced cross-section by cross-section. The CFD software package, FLUENT (ANSYS Inc., USA), was also used for developing comparison data. The results about wake width, velocity profiles, pressure profiles, and added turbulence intensity will be discussed in the far-wake with and without swirl. Discussion will also include the efficiency of the far-wake model.

1.7.2. Results and Discussion.

1.7.2.1. Verification of far-wake development model.

The far wake velocity profile is obtained using the self-similarity assumption. According to this assumption, the half-width wake radius increases in proportion with the distance downwind raised to the power "n". This constant "n" was found out to be statistically 0.386 when the ratio of the velocity at the center of the wake to the velocity at the edge of the wake is greater than or equal to 0.9. Compared to theory (Pope, 2000), there is a 16% error, because of the limitation of the finite radial dimension for calculation in EXPRESS compared to radial infinity theory.

1.7.2.2. Wake Width and half radius.

Both the wake width and the half radius increase with wake development in the axial direction, except the wake expands more in the radial direction at low Reynolds numbers. At the same axial position, both wake width and half radius decrease with the Reynolds number which indicates that high wind speed (usually linked with a high Reynolds number) may suppress wake expansion, compared with low wind speed. The suppressing effect of high wind speed on the radial wake expansion is gradually weakened as the Reynolds number changes. Results suggest that the radial dimension of the wake increases with the swirl strength.

1.7.2.3. Velocity and pressure.

With no swirl, low wind speeds cause increase in wake velocity at the axis. The swirl velocity decreases with axial growth of the wake, while the radial velocity always remains insignificant. As predicted, a low pressure region occurs at the center of the wake in the near wake region, and pressure increases with radius. In the far wake region, pressure variation is insignificant.

1.7.2.4. Added turbulence intensity.

The turbulence created by wind turbine intensifies the turbulence intensity in the wake region. The results of the turbulence intensity computed by EXPRESS at various wake cross-sections are in good agreement with experiments (Vermeer 2003).

1.7.2.5. Comparison of Results.

The two turbulence models (in EXPRESS, k-ε and RS transport) are similar in development of both the wake width and the half radius. It is generally regarded that the RS model is more accurate for the simulation of turbulence than the k-ε model; however, the two models show similar results. The boundary layer theory simplifies basic equations by neglecting some axial gradients and effects of the radial velocity, which can affect the accuracy of the RS transport model (more so than the k- ε model). Assumptions of self-similarity and axisymmetry in the far-wake also introduce inaccuracy.

Comparison between two CFD codes EXPRESS and FLUENT show that the RS model compares well for the two codes than the k-ε model. Some discrepancies between EXPRESS and FLUENT are a result of the simplification of the boundary layer theory and similarity assumptions. Also, an expanding grid was not used in FLUENT unlike EXPRESS.

1.7.3. Conclusions.

The far-wake model herein proposed is based on the boundary layer theory and self-similarity assumption and can predict far-wake development in large axial distances and still allow small radial dimensions. The far-wake radially expands less at higher Reynolds numbers and expands more when swirl exists. Both the axial velocity and the swirl velocity (when swirl exists) are two dominant velocity components, but the radial velocity plays a negligible role. Swirl helps to accelerate velocity at the axis, and pressure is insignificant regardless of whether the wake has swirl or not. The added turbulence intensity declines rapidly with the far-wake downstream development.

The model uncovered the following features:

- The boundary layer theory simplifies the general Navier-Stokes equations, continuity equation, and turbulence model equations,
- Simplicity of the basic equations compromises the accuracy,
- The RS transport model does not show obvious advantages over the k-ε model,
- The numerical algorithm to solve the flow fields is simple, whereas very fine meshes are needed in the radial direction.

Subtask 1.8: Investigate a Distributed Wind Turbine Response and Condition Monitoring System and Associated Compact Energy Harvesting Circuits.

1.8.1. Condition Monitoring System

1.8.1.1. Introduction.

Structural health monitoring (SHM) has been a research area that has recently been experiencing fast growth. This is happening because wired sensor networks are very costly to maintain and install. To alleviate this issue, a new monitoring system was developed. Subtask 1.8 was the design and implementation of condition monitoring devices for wind turbines (referred to as "Remote Wireless Sensors") to have the capability to monitor wind turbines infrastructure health status remotely, without human physical intervention. Additionally, the developed tool needed to be very low maintenance and self sufficient.

The system consists of two parts: multiple distributed data collection agents and a data collector where all the data arrives for further processing. To achieve the task at hand, a number of battery powered, wirelessly networked data collection agents, referred to as "nodes", were equipped with accelerometers and temperature sensors. The accelerometer is of the three axis variety which enables the node to measure three dimensional acceleration experienced at the point where the node is installed. Temperature could be determined by using the equipped temperature sensor to aid in the health diagnosis process. Other components located in the nodes, shown in Figure 1.8.1.1, is a 2.4GHz radio transceiver, external random access memory, permanent flash memory and of course, a microcontroller that controls all operations within the nodes.

Figure 1.8.1.1. Sensor node circuit board with enclosure, lid contains a Li-Ion battery, and neodymium magnetic mounts.

The wireless sensor nodes are capable of sampling acceleration and temperature data at a rate of up to 1.5kHz which amounts to a large amount of data if the sampling time exceeds more than a few seconds. To overcome this, data compression was implemented to reduce the data size. By reducing the data size, the nodes would transmit less data which allows the node to conserve power.

Once data has been sampled at the nodes, it is transferred to a data collector at a central location where the data is processed and permanently logged (referred to in the literature as "The Base Station"). The base station was designed by Davis Hoover with a number of ways to output the data gathered by the nodes. The first way is to simply log this data into an SDCARD which can be read using a standard computer with an SDCARD reader and FAT16 support. It also supports an Ethernet connection, a GPRS connection and a USB connection. For time stamping the log files, the base station uses a GPS module to read time and date information from GPS satellites. Figure 1.8.1.2 shows the base station hardware.

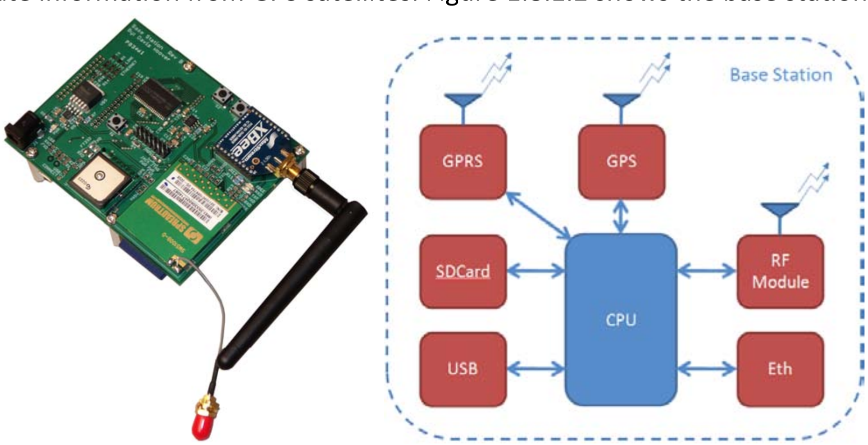

Figure 1.8.1.2. Base station (left) and block diagram (right).

1.8.1.1.a. Instrumentation.

Additional to the data collection nodes and the base station hardware, other instrumentation was used to aid the validation of the data collected by the new system. A scale model truss bridge was constructed to use as a test bed for the system. To simulate the loads applied to a real full scale bridge, a magnetic shaker attached to the middle of the structure was used as a load source.

A set of PCB333B50 conventional wired accelerometers were installed in the structure to use as reference to validate the new hardware design. All the accelerometers were wired to a National Instruments Compact RIO chassis for data acquisition into a computer. The testbed can be seen in Figure 1.8.1.3.

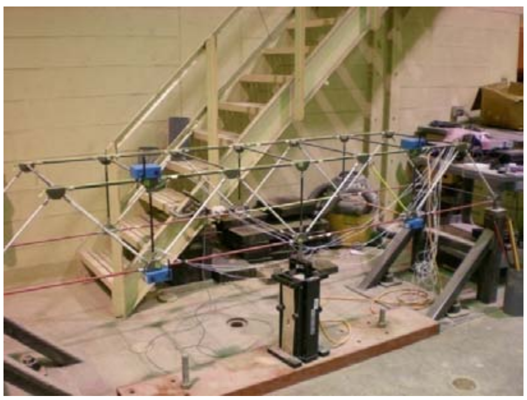

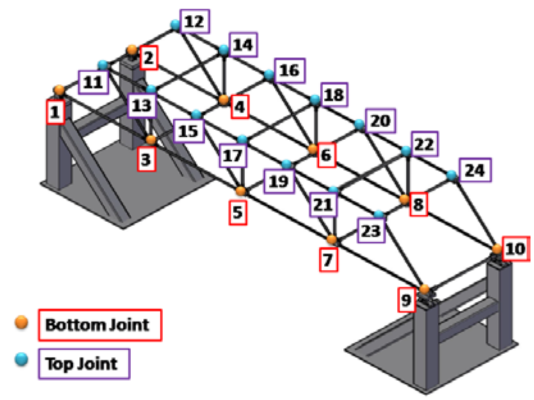

Figure 1.8.1.3. Truss bridge network validation test setup with four nodes (left) and rendering of truss bridge with joint IDs used for network validation (right).

1.8.1.1.b. Dataset Validation.

In order to determine if the wireless sensing system's collected data was valid, data was collected from all nodes simultaneously at 250Hz. During this time the bridge was exited using the shaker with a 40Hz low pass filtered white noise signal.

After the data was sampled, no processing was done at the nodes. Instead, this data was transferred to the computer and the auto power spectral density was computed. The same was done to the data collected by the wired accelerometers. A portion of the collected data is shown in Figure 1.8.1.4 and the auto power spectral density is shown in Figure 1.8.1.5.

1.8.1.2. Power Consumption.

The wireless sensor nodes achieved impressively low power consumption numbers. This allowed a maintenance free operation for a period of three months using only three D size alkaline batteries with an active operating duty cycle of 1%. The data sampling period and the data transmission period is what for the most part determines the node's battery life. This is because when the node is sampling the analog circuitry, external RAM and the CPU have to be powered up. During the data transmission time, the radio has to be on, which constitutes for a large percentage the total power consumption of the node.

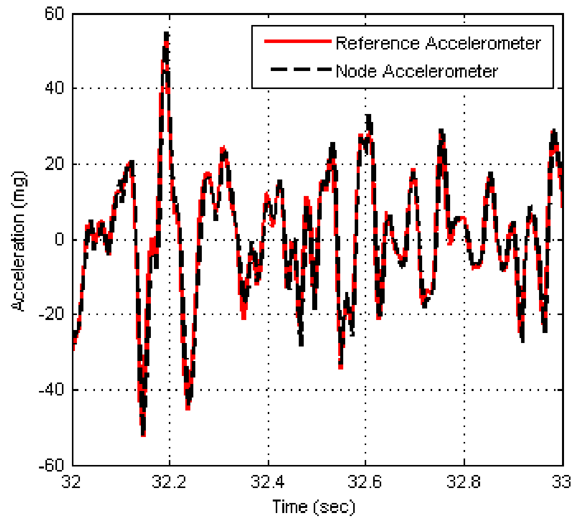

Figure 1.8.1.4. Sampled acceleration-time data from node and reference accelerometer.

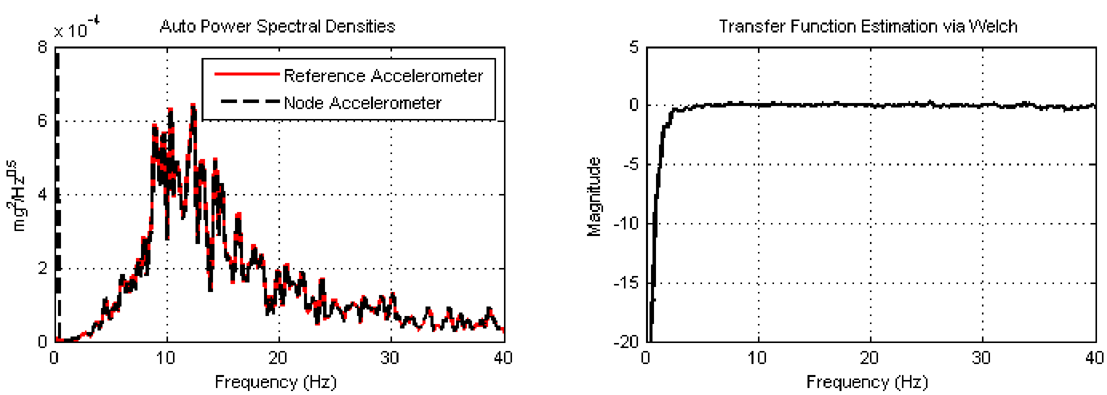

Figure 1.8.1.5. Auto power spectral densities and transfer function of simultaneously sampled acceleration data from node and reference accelerometer.

As it can be seen in Table 1.8.1.1, minimizing the data transmission and reception time is what saves the most power. Optimizing these stages was critical.

Table 1.8.1.1. Node Measured Current Consumption.

State	Current	Active Blocks
Idle	150μA	None
Sampling @ 20 Hz	3.68 mA	Analog front-end, SRAM, CPU
Sampling @ 40 Hz	3.69 mA	Analog front-end, SRAM, CPU
Sampling @ 100 Hz	3.82 mA	Analog front-end, SRAM, CPU
Sampling @ 250 Hz	4.13 mA	Analog front-end, SRAM, CPU
Sampling @ 400 Hz	4.44 mA	Analog front-end, SRAM, CPU
Sampling @ 500 Hz	4.55 mA	Analog front-end, SRAM, CPU
Compressing Data	8.93 mA	SRAM, CPU
Transmitting Data	45 mA	SRAM, CPU, Radio
Receiving Data (Commands)	50 mA	CPU, Radio

1.8.1.3. Conclusions.

During the length of the project, a remote wireless sensor network was developed and designed to overcome limitations imposed by similar systems available at the time. The developed system met all the expectations set during the planning stage, and battery life of three months with only three type D battery cells was achieved. Gravity measurement resolution in the µG range was obtained.

A system validation test bed was developed with a truss bridge, a magnetic shaker and multiple reference accelerometers. The data collected from the nodes and the reference accelerometers was analyzed and an auto power spectral density was calculated for both. Comparing the two computed power spectral densities validated the data collected by the nodes.

1.8.2. Energy Harvesting.

1.8.2.1. Introduction.

The research objective for the project was to design an ultra low power multi-energy scavenging system capable of collecting energy from ambient vibrations and RF electromagnetic waves and then to transfer the collected energy in an efficient manner to an energy storage bank consisting of thin film battery for later use.

Since the available energy from the antenna and piezoelectric generator is less, the major challenge in this project was to design efficient power electronic circuits capable of converting this ambient energy into usable energy levels. AC-DC Charge pump, DC-DC Charge pump, linear drop-out regulators and rectifier are part of the energy harvesting IC electronics.

In this work, each energy harvester was evaluated and characterized to maximize the efficiency. The power electronic circuits involved in the energy harvesting were designed in 0.6um CMOS technology and the analytical models and simulation results were presented. A regulated output was provided which is intended for low-voltage and low-power applications.

The multi-energy scavenging system should be able to recharge a battery that supplies energy to the sensors that are intended to transmit information only from time to time and at low power. For example, consider a sensor module with its battery pack placed under a bridge to monitor the mechanical properties of the bridge. The sensor sends data during any emergency to a distantly located control room. As there may be several months between someone repowering the batteries, energy harvesting from the environment finds its application.

Energy harvesting technology has already been commercialized in different ways by many companies like Texas Instruments, Micro Strain, Advanced Cerametrics, Linear Technologies, etc., to name a few.
A block diagram of the system is shown below in Figure 1.8.2.1. The green area shows the two transducers used to harvest energy: Piezoelectric generator and the antenna. These transducers convert different types of energy (vibration and wave energy) into electrical energy. Upon conversion, there are several signal conditioning circuits to transfer the collected energy to the storage bank (red area). The signal conditioning circuits (blue area) are rectifiers and charge pumps for AC signals, and DC-DC converters and linear regulators for DC signals. The storage bank consists of thin film battery. The battery is typically charged slowly and supplies most loads that draw low currents (in µA). A complete literature review was conducted for this research and the results are given in the list of references.

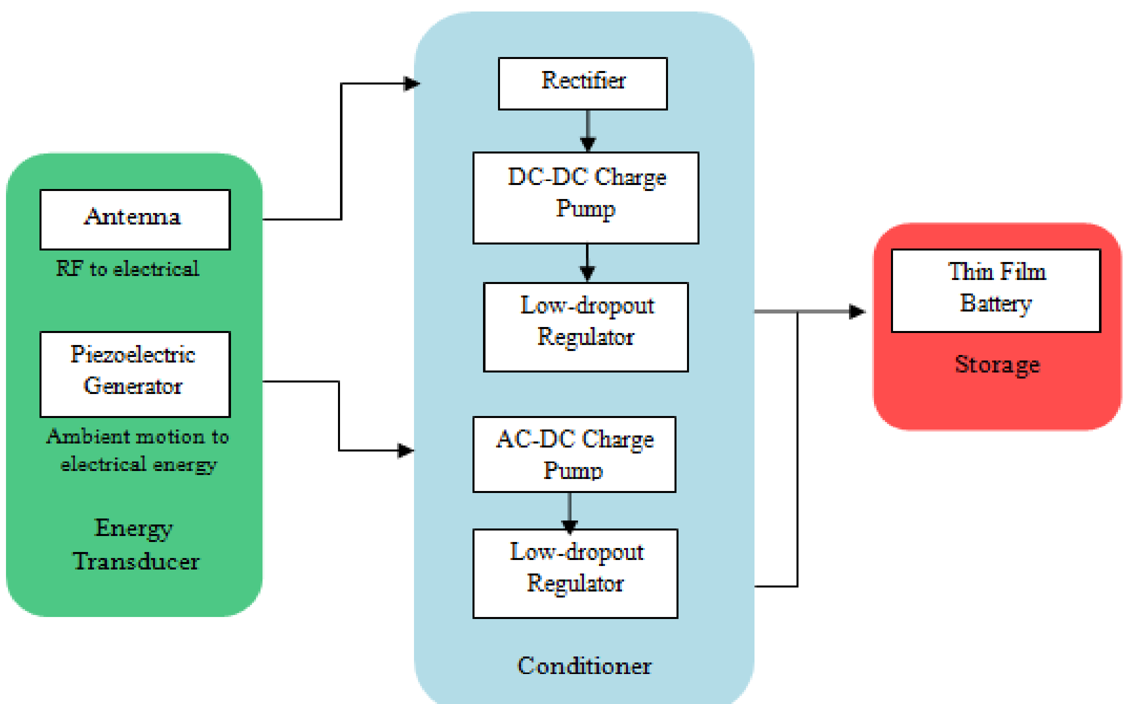

Figure 1.8.2.1. System overview of the smart energy harvester (Divya 2011).

The above system was modelled and simulated in Pspice and Cadence. The initial design was done in Pspice to optimize the outputs. Then the optimized design was transferred to Cadence for development of the chip design. Dickson charge pump was designed and simulated in Pspice with BAT54ST schottky diodes whose forward voltage drop is around 240mV. The schematic of a 16 stage Dickson charge pump with input and clock amplitudes of 1V is shown in Figure 1.8.2.2 along with the output voltage waveform. Because of the lower forward voltage drop across the diodes, higher output voltage is obtained when compared to cadence design. The results shown in Figure 1.8.2.2 are a representation of the results from this research.

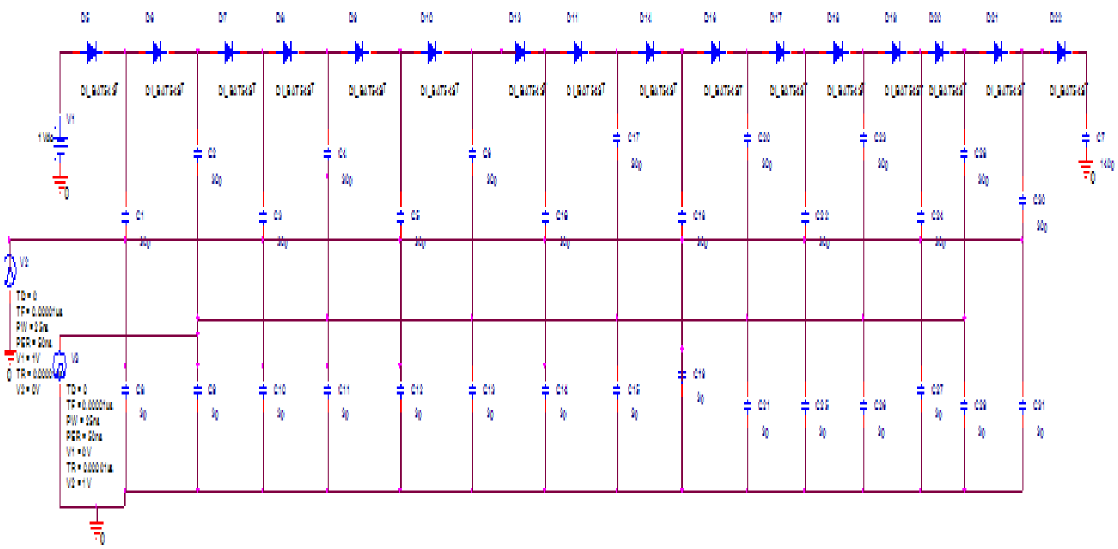

(a)

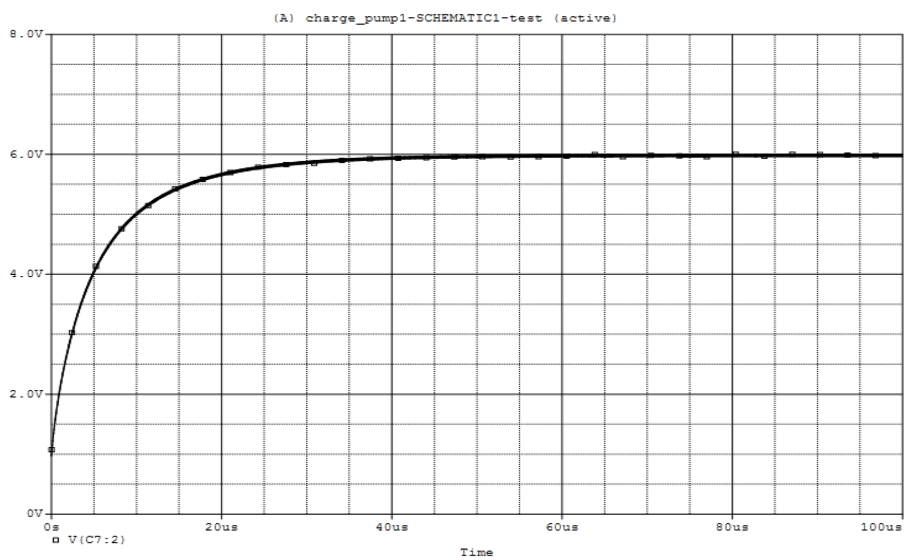

Figure 1.8.2.2. Charge Pump system (Divya 2011).

1.8.2.2. Results and Discussion.

After the circuit was designed and the output validated, an ASCI chip was designed and sent out for fabrication.

The layout for this system was created using a 0.6 µm CMOS technology. Several basic transistor layout techniques were implemented to preserve the signal integrity of this system. One of these techniques is splitting the large transistors into smaller transistors connected in parallel by using multipliers; for example, each NMOS of the charge pump was split into 10 individual NMOS having a width of 6 µm and a length of 0.6 µm instead of having one big NMOS with a width of 60 µm.

Another technique implemented in this circuit is that all the PMOS transistors in the system layout had their bulk terminal connected to the source 'S' terminal of the PMOS transistor to reduce body effect, and the bulk terminal for all the NMOS transistors in the design were tied to the p substrate which is tied to Vss. To reduce the noise produced by each sub-section of this layout, the NMOS and PMOS sections of each individual circuit layout were isolated from each other by using guard rings.

A guard ring is a continuous ring made of substrate ties that surrounds the circuit thereby proving a low-impedance path to ground for the charge carriers produced in the substrate. The guard ring for the NMOS transistors were formed using several M1_P (metal one to p substrate) contacts while those for the PMOS transistors were formed using several M1_N (metal one to n substrate) contacts.

The charge pump layout for this design is shown in Figure 1.8.2.3 and Figure 1.8.2.4. This layout has a dimension of 126.6 µm by 32.4 µm. The bulk of the NMOS transistors served as the guard ring for the NMOS transistors and was also connected to Vss. The capacitors for the charge pump are off-chip components because they were too large to be laid out in the chip.

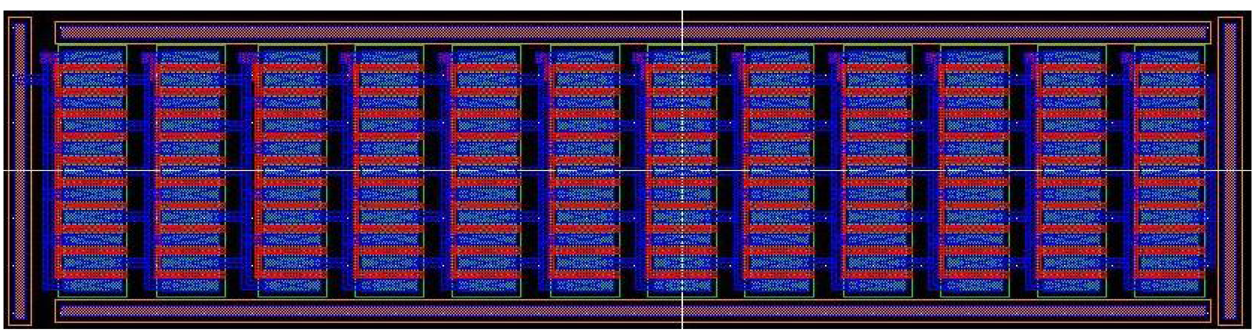

Figure 1.8.2.3. Layout of the AC-DC charge pump.

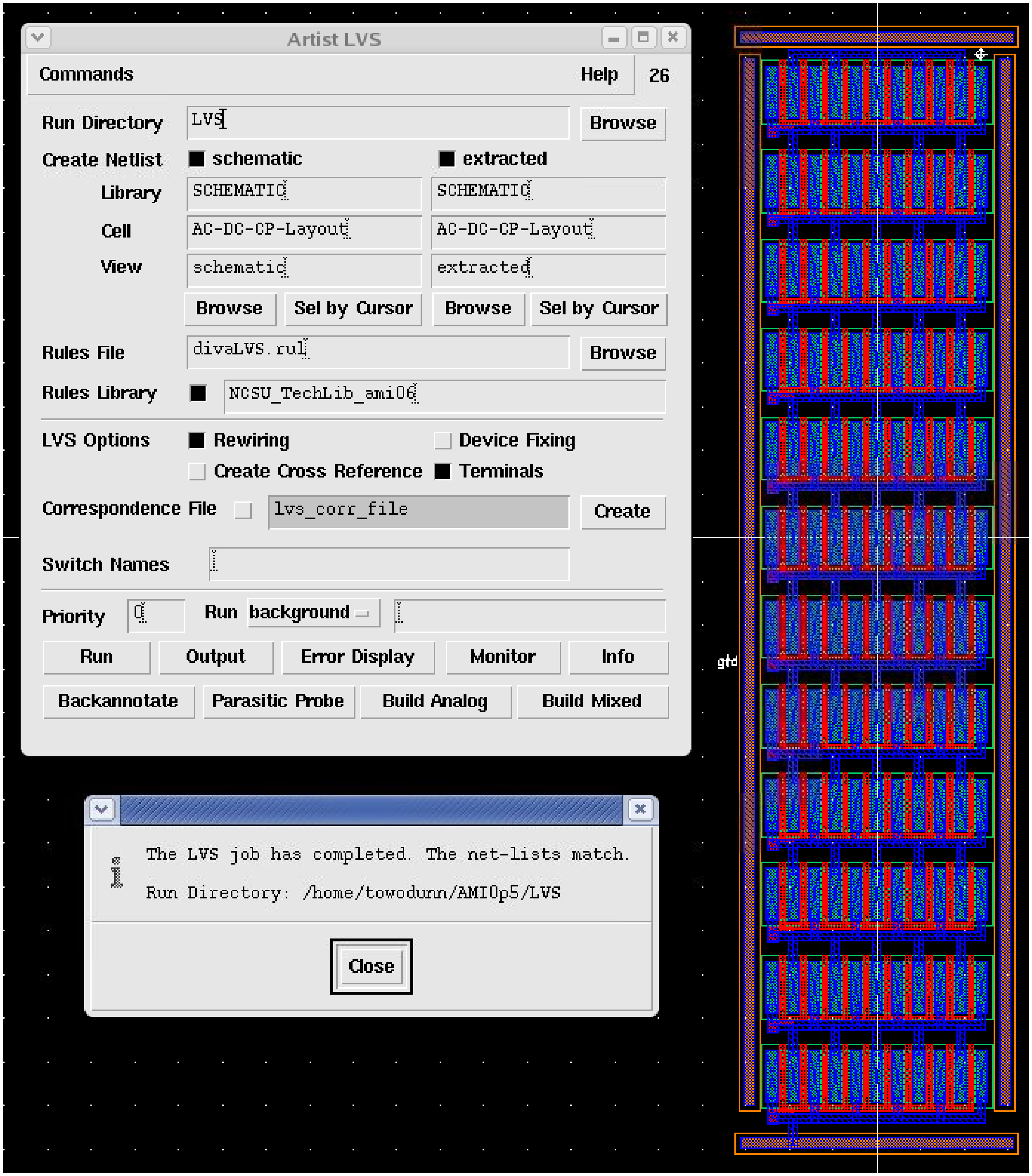

Figure 1.8.2.4. AC-DC charge pump layout matches the schematic.

The dimension of the voltage reference layout for this system is 110.25 μm by 67.35 μm and the layout design techniques discussed in section 3.3 of this paper were implemented in this layout. This layout has some on-chip resistors and capacitors. Figure 1.8.2.5 shows the layout of the voltage reference circuit and Figure 1.8.2.6.

The layout of the resistor was implemented using an ELEC and Highres layer.

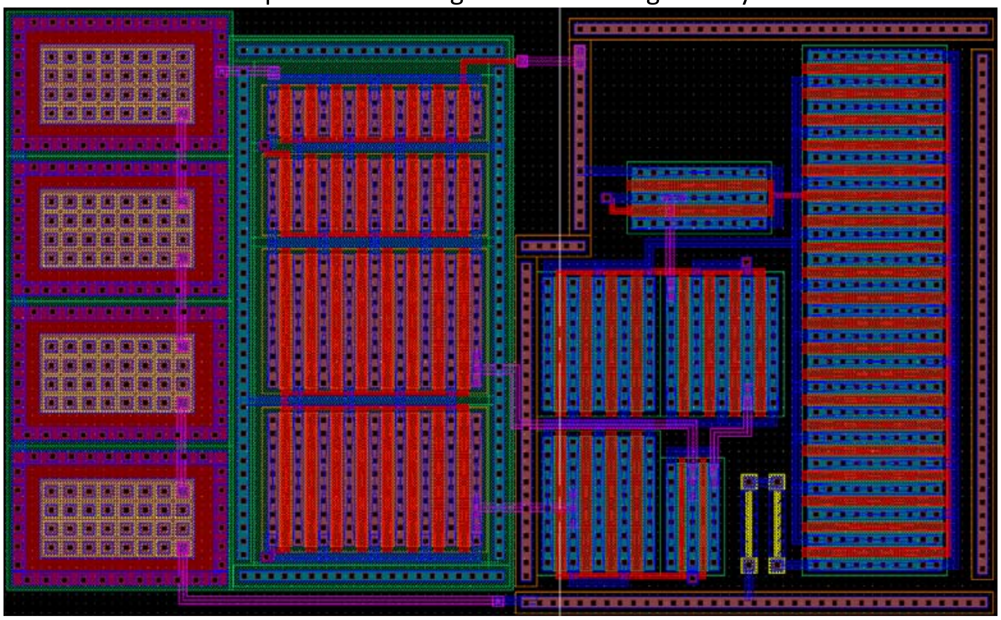

Figure 1.8.2.5. Voltage Reference Layout.

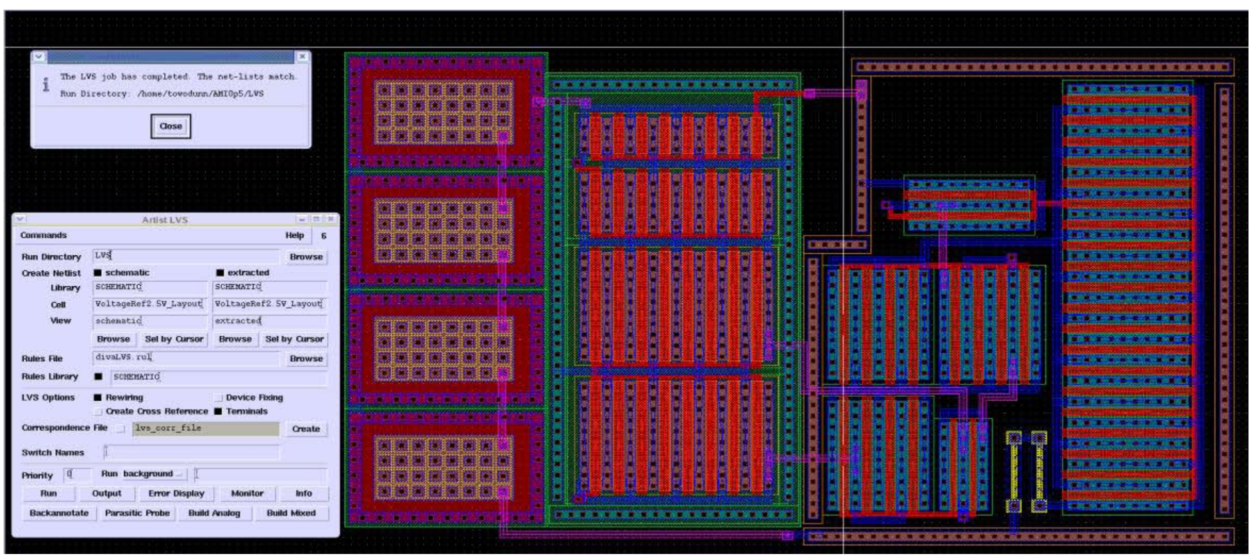

Figure 1.8.2.6. Evidence that the Voltage reference layout matches the schematic.

1.8.2.3. Conclusions.

The purpose of this research is to design an integrated energy harvesting system that converts both vibrations and radio frequencies into electrical energy. The design of the integrated system has been separated into two designs – vibration energy harvesting design and radio frequency energy harvesting design. A piezoelectric energy harvester was designed as the vibration harvester because they have a wider operating range than other transductors.

As indicated by the results in the previous section of this research paper, the initial design for the piezoelectric energy harvesting portion of this integrated system has been completed. This piezoelectric system has an output voltage range of 3.58 V – 4.45 V from the test-bench simulation for the design schematic while the layout test-bench has an output voltage range of 3.60 V – 4.47 V.

The minimum and maximum values from these two test benches fall outside the allowed range for the thin-film battery (4.0 V – 4.2 V) but these are allowable ranges for the initial system design. This range will be tightened in subsequent designs to align with the allowed range for the thin-film battery. The ASIC for this system was designed using a 0.6 µm CMOS technology and has been completed and will be sent out to the factory for fabrication.

Subtask 1.9: Investigate the Structure of the Tropical Cyclone Boundary Layer Wind Structure over Offshore Waters.

1.9.1. Introduction.

In order to support the economical deployment of offshore wind farms in the southeast and Gulf coast regions of the US, design level events, such as those generated by tropical cyclones, must be documented and accommodated with proper design. This study seeks to understand the characteristics of tropical cyclone vertical wind profiles. Emphasis was placed on understanding changes in the lowest 1.5 km, including the hurricane boundary layer (HBL).

The deployment of GPS dropwindsondes (GPS sondes), beginning in 1997, has provided a wealth of information regarding the kinematic and thermodynamic structure of the HBL (Hock and Franklin 1999, hereafter HF1999). The current study employs vertical wind profiles from GPS sondes released in deep water conditions to examine changes in the mean vertical wind profile with storm-relative position, and uses a modified velocity azimuth display (VAD) technique to produce a large number of vertical wind profiles at landfall. The characteristics of low-level wind speed maxima within vertical wind profiles were also investigated through their associated statistics. Through the compositing of profiles, a conceptual understanding of the evolution of the vertical wind profile with changing radius in the open ocean and at landfall was developed.

Historical studies have documented the presence of jet-like features within tropical cyclone vertical wind profiles prior to the implementation of GPS sondes (Wilson 1979). The GPS sonde archive has provided a large number of high-resolution profiles which include data from the lowest 500 m of the HBL. Franklin et al. (2003, hereafter FBV2003) and Powell et al. (2003, hereafter PVR2003) used a large number of GPS sondes to produce composite wind profiles; both found a wind speed maximum near

500 m with a logarithmic decrease below. Radial and storm-relative position asymmetries were observed by FBV2003, but were attributed to influences from individual sonde trajectories rather than dynamical processes. PVR2003 used the mean boundary layer (MBL) wind, which is a layer mean below 500 m, to scale a single composite profile for all observations and to group GPS sonde profiles into different mean wind environments. Although the focus was on air-sea interaction, PVR2003 showed a decrease in the height of the mean wind speed maximum with increasing MBL wind and a jet-like profile became evident as the MBL wind increased above 50 m s-1. Vickery et al. (2009) used similar composite profiles to show that the wind profile was logarithmic through the depth of the wind speed maximum, while Amano et al. (1999) used Doppler sodar observations to illustrate the validity of power law wind profiles during several landfalling typhoons.

Although the observational studies of FBV2003 and PVR2003 provided evidence to support the mean presence of a broad jet-like wind profile, individual GPS sonde wind profiles often departed from the mean structure (FBV2003). The individual profiles are subjected to a variety of scales of motion during descent, while also moving several kilometers azimuthally and several hundred meters radially. Profiles often contain several local wind speed maxima and minima. Although the motion of the instrument is well understood, it remains unclear what the specific scales of motion the perturbations within individual profiles represent.

1.9.2. Results and Discussion.

1.9.2.1. Analysis Methodologies and Techniques.

Composite wind profiles were produced for both GPS sondes and VAD wind profiles. The use of composite profiles allowed for the comparison between open-ocean and landfall conditions and additionally provided information regarding the mean structure of the vertical wind profile. Individual profiles from each platform are vastly different in measurement characteristics. The profiles were normalized by the MBL wind to produce a composite using all available GPS sonde or VAD observations. Profiles were also grouped using the MBL wind similar to PVR2003. This layer mean was selected to normalize the wind speed observations since it typically contains the wind maximum and is not significantly influenced by local wind speed maxima and minima within the layer. GPS sondes were grouped according to MBL wind speed using 5 m s^{-1} bin sizes, which is smaller than the 10 m s^{-1} size used by PVR2003 and Vickery et al. (2009). The larger number of GPS sondes used in the current study allowed for the smaller bin size. A 10 m s^{-1} bin size was applied to VAD profiles due to the relatively smaller total number of available profiles. Composite profiles were generated for each group according to PVR2003 through the application of the Ergodic assumption. Individual profiles were also stratified by radius, radius scaled by an estimate of the surface RMW $(\frac{R}{R_{\max}})$, and storm-relative azimuthal sector. Storm-relative azimuth sectors were: Right 20-150º, Rear 151-240º, and Left-front 241-19º. The sectors are based on differences in the underlying wave characteristics of each described by Wright et al. (2001).

The following radial (scaled radius) groupings for GPS sondes were used: less than 30 km (<1.0), 30-60 km (1.0-1.34), 60-112 km (1.34-2.10), and greater than 112 km (2.10). The values represent the quartiles of the splash radii (scaled radii) distribution for GPS sondes used in the current study. The quartiles of the VAD radius (scaled radii) distribution were slightly different for smaller radii, with groups of less than 40 km (1.0), 40-60 km (1-1.53), 60-112 km (1.53-2.65), and greater than 112 km (> 2.65). The surface radius of maximum winds was estimated using historical, gridded H*Wind operational wind field analyses (Powell et al. 1998). The analyzed, gridded wind field was rotated into a storm-relative coordinate system and the maximum 1-minute marine exposure wind speed was found in each storm-relative sector. The associated radial distance was assigned as the surface RMW for the given sector at the time of the analysis. A linear interpolation was used to provide a continuous estimate of the surface RMW between operational analyses. The RMW for the sector in which the GPS sonde landed was assigned to the individual profile.

1.9.2.2. Open-Ocean Wind Profile Characteristics.

1.9.2.2.a. GPS Sonde Composite Profiles.

Mean profiles were generated for each MBL wind group (Fig. 1.9.2.1) and showed a broad wind speed maximum. As expected, the profiles exhibited a logarithmic increase up to the wind speed maximum. The height of the total and tangential wind speed maxima decreased with increasing MBL wind speed, for MBL≥ 60 m s -1 but the number of sondes available for analysis decreased substantially (Figure 1.9.2.1). The standard deviations for each profile decreased with height through the wind maximum and then increased above. The decrease in variance was expected as mechanical production of turbulence is expected to dominate and turbulence intensities should decrease with height.

1.9.2.2.b. Mean Structure and Radial Dependencies.

A reduction in the height of the wind maximum with decreasing splash radii and scaled radius was observed after the GPS sondes were composited (Figure 1.9.2.2A, Figure 1.9.2.3A). When normalized by MBL wind speed the magnitude of the wind maximum decreased with decreasing radius. The result was inherently tied to the decrease in the wind maximum height with increasing MBL wind speed, and larger speeds would be expected to be found at smaller radii. The composite profiles, grouped by scaled radius, exhibited slight differences from that observed using an un-scaled radius (Figure 1.9.2.2A, Figure 1.9.2.3A). The altitude of the wind maximum descended with decreasing scaled radius to a minimum near 400 m radially inward from the surface RMW. The composite profile at the RMW and slightly outward (1-1.34 group) exhibited a wind maximum near 500 m. Unfortunately the number of GPS sondes did not allow for stratification by both MBL wind and radial distance.

1.9.2.2.c. Mean Structure and Azimuthal Dependencies.

Differences were also observed between composite profiles generated following segregation of sondes into storm-relative azimuthal sectors (Figures 1.9.2.4A and B). Although not as striking as those found within the radial groupings, a 500 m scaled wind maximum was found in the rear sector composite profile, with the right and left-front sectors exhibiting similar profiles but with a maximum near 600 m. This coincided with a change in the slope of the total wind profile, and suggested a possible reduction in surface roughness in this region. The rear sector was characterized by Wright et al. (2001) as having relatively small wavelength waves (150-200 m) which are less developed than those typically found in the right and left-front sectors. The orientation of the wave field is along the mean flow which may contribute to a smoother effective roughness and the differences between the composite profiles of the rear sector compared to the other regions (Wright et al. 2001).

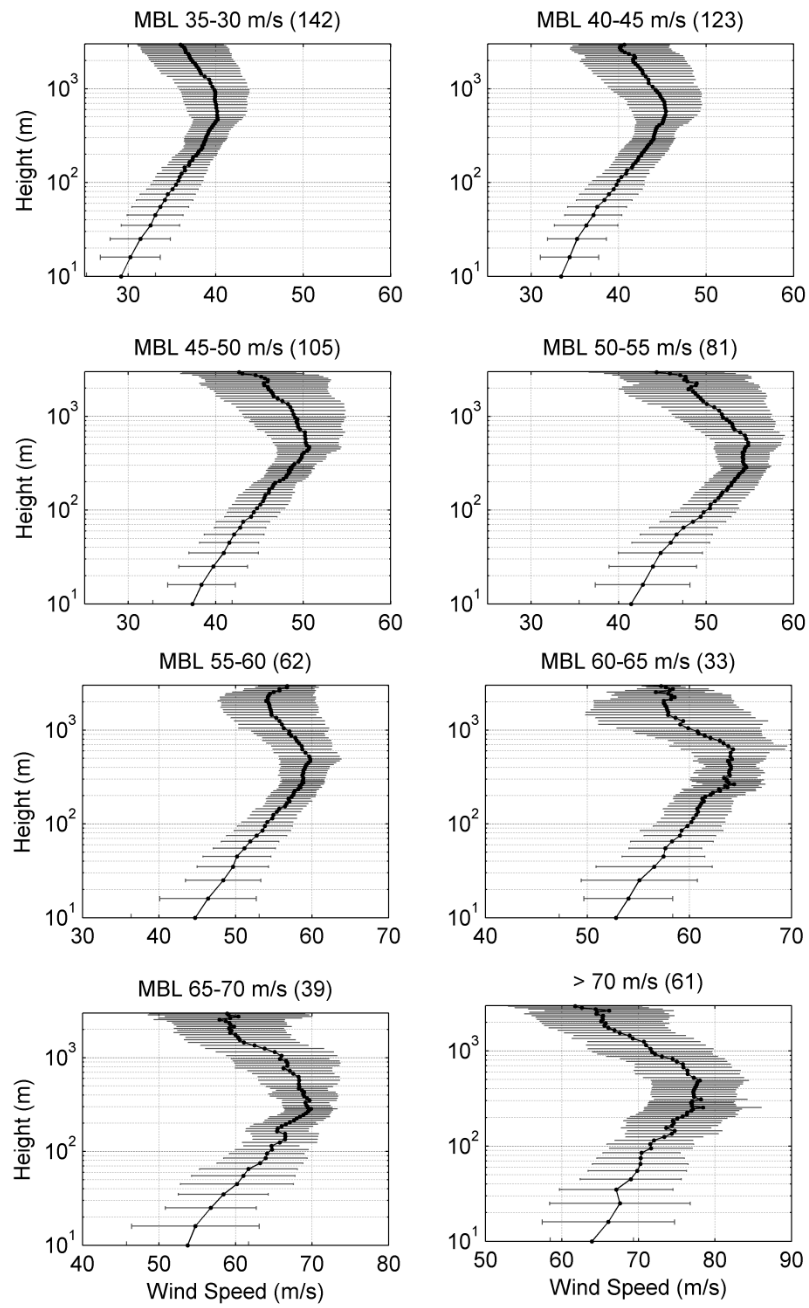

Figure 1.9.2.1. Composite wind profiles for MBL wind speed groups. Error bars represent ±1 standard deviation from the mean. The total number of GPS sondes included in each composite is provided in parentheses.

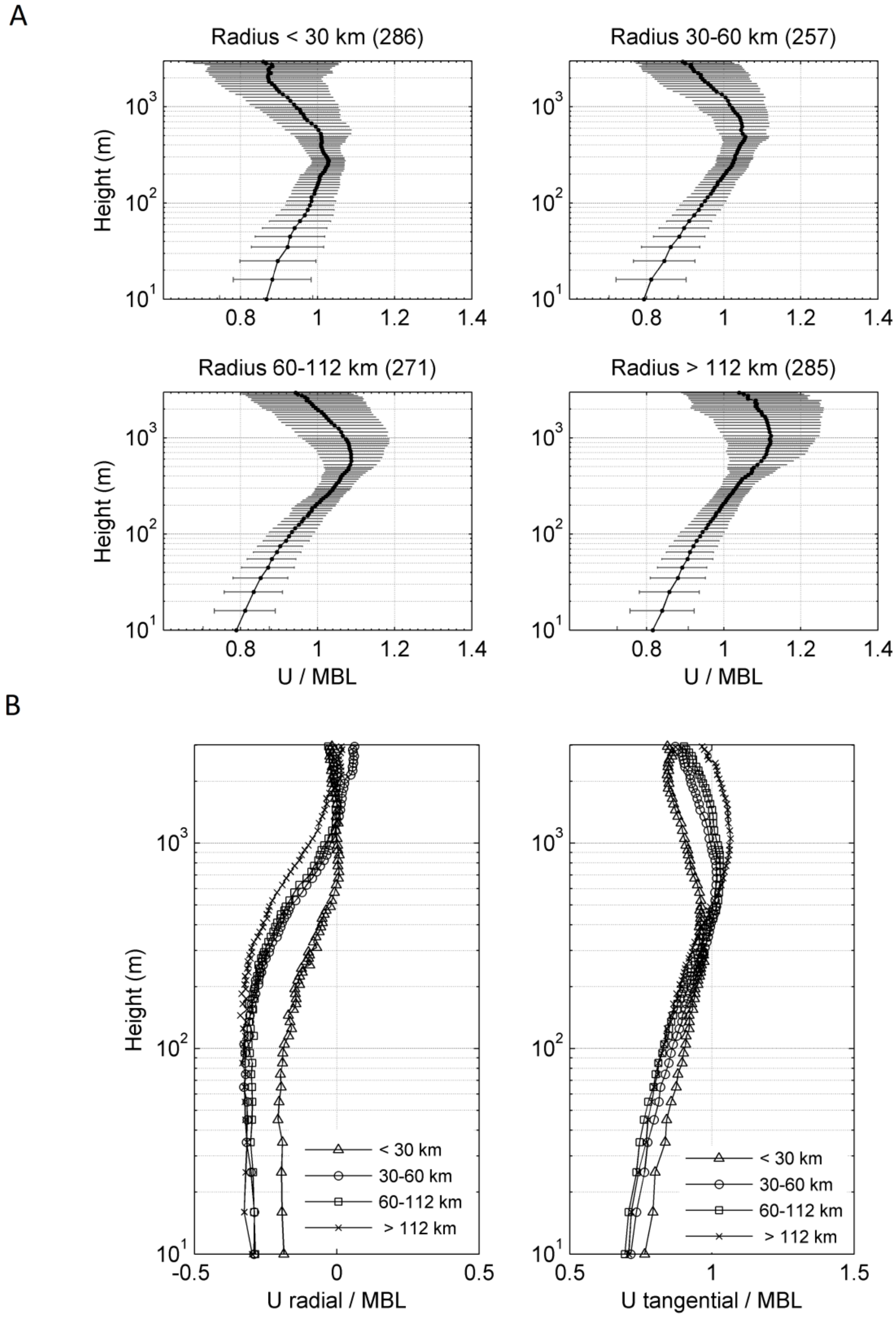

Figure 1.9.2.2. GPS sonde composite of (A) total wind, (B) tangential and radial component profiles for splash radii stratifications of: < 30 km, 30-60 km, 60-112 km, and > 112 km. Error bars represent ±1 standard deviation from the mean. The total number of GPS sondes included in each composite is provided in parentheses.

A

B

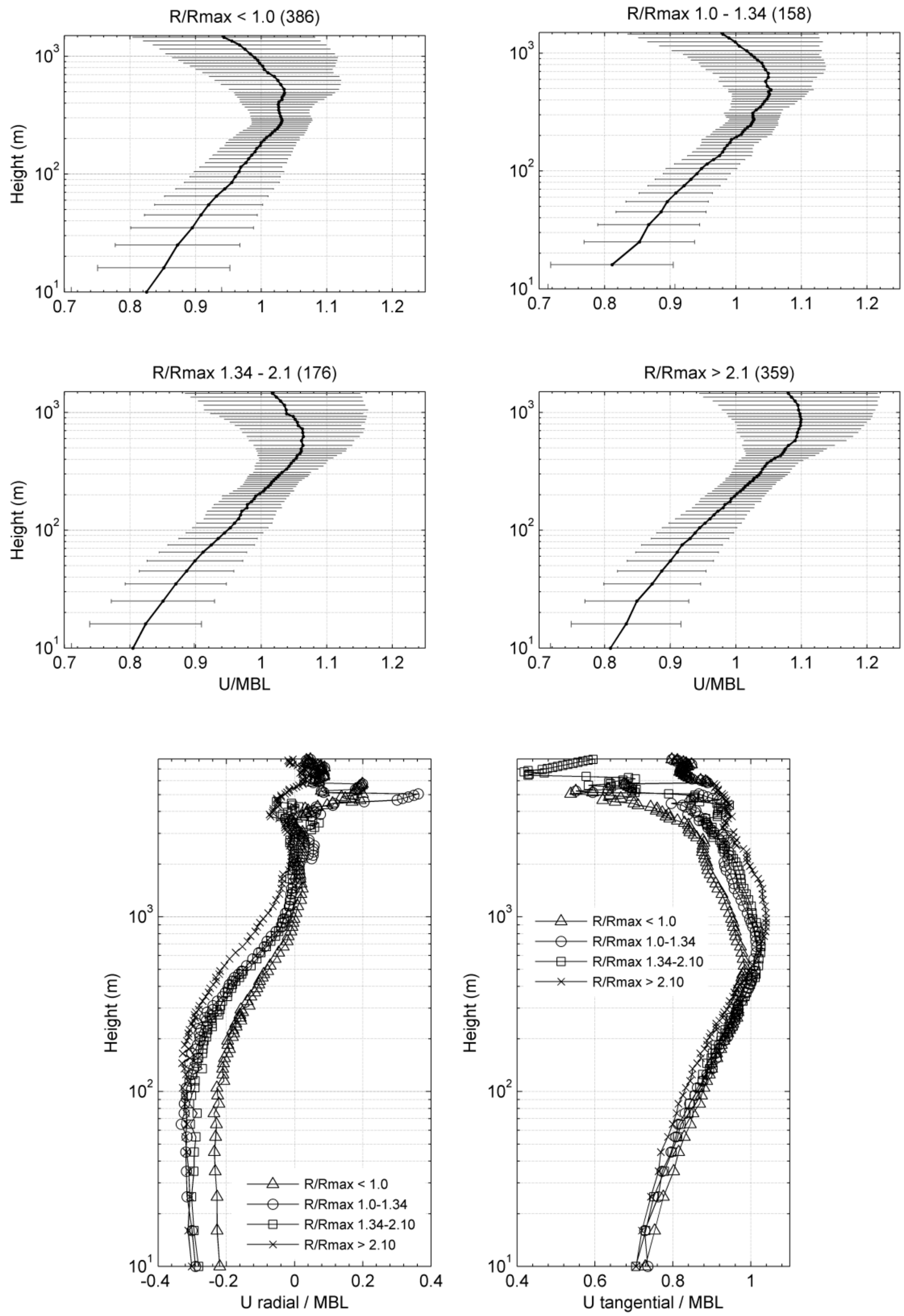

Figure 1.9.2.3. GPS sonde composite of (A) total wind, (B) tangential (right) and radial (left) component profiles for splash radius scaled by the surface radius of maximum winds of: < 1.0, 1.0-1.34, 1.34-2.10, and > 2.10. Error bars represent ±1 standard deviation from the mean. The total number of GPS sondes included in each composite is provided in parentheses.

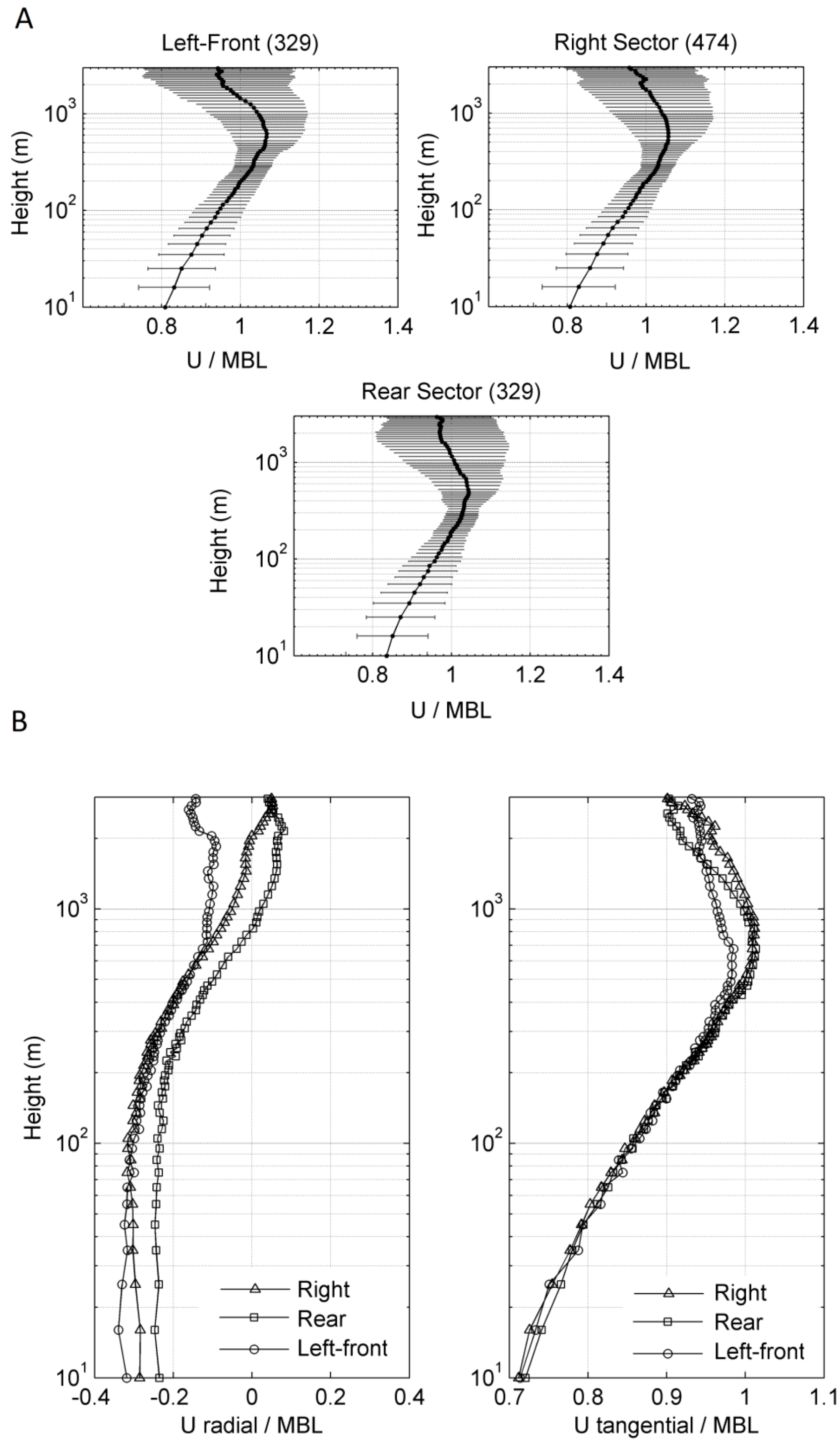

Figure 1.9.2.4. GPS sonde composite of (A) total wind, and (B) tangential (right) and radial (left) component profiles for storm-relative sectors. The number of GPS sondes included in each composite is provided in parentheses.

1.9.2.2.d. GPS Sonde Wind Speed Maxima.

The underlying GPS sonde profiles were examined in an effort to understand the characteristics of low-level wind maxima which have been observed in individual profiles (Franklin et al. 2003). Absolute wind speed maxima within the HBL of individual profiles were prevalent within the dataset as nearly 40% of all GPS sondes contained a peak wind speed below 500 m. The height of the absolute wind speed maximum exhibited a radial dependence; profiles with a maximum below 200 m were typically confined to small radii, near and radially inward from the surface RMW (Fig. 1.9.2.5A and B). Maxima which occurred between 200-500 m altitudes were typically confined to within 100 km radius whereas maxima found above 500 m were well distributed radially. The peak wind speed observed in each profile was scaled by the MBL wind speed as well as the layer mean of the lowest 150 m of the profile (WL150; Franklin et al. 2003). The scaled wind maxima exhibited a radial dependence as large values were typically confined to large radii with a decrease in magnitude found toward the center. Extreme low-level wind maxima (< 200 m altitude) appear to be confined to the eyewall region with a large percentage (68%) located radially inward from the surface RMW. Maxima in this region only deviated from the MBL wind speed by 10% or the WL150 layer mean by 15%. The departures from the layer mean were similar to that observed in near-surface gust factors by Schroeder et al. (2009) within high-resolution observations of landfalling tropical cyclones. Mean gust factor values were found to decrease with no change in upstream roughness as the radial distance from the tropical cyclone center decreased.

1.9.2.3. Characteristics of Hurricane Vertical Wind Profiles at Landfall.

1.9.2.3.a. Overland Composite Profiles.

The derived VAD profiles were grouped by MBL wind speed using 10 m s^{-1} bin sizes. The relatively small number of profiles (compared to GPS sondes) warranted a larger bin size. Differing from the composite technique for GPS sondes, wind speeds were scaled by the MBL wind in order to mitigate the influence of differing surface roughness conditions between radar sites. Below 30 m s^{-1} the composite profiles increased throughout the depth of the profiles, while the higher mean wind speed profiles exhibited a relatively constant magnitude above 300 m. A pronounced low-level wind speed maximum was not evident in any of the composite profiles (Fig. 1.9.2.6A).

1.9.2.3.b. Mean Structure and Radial Dependence.

The VAD profiles were stratified according to radius (scaled radius), with the smaller number of VAD profiles allowed for a subjective eyewall or outer-vortex classification. Similar to the GPS sonde composite profiles, a clear low-level wind speed maximum was evident within the total wind speed and tangential wind component for the representative composite VAD profile within 40 km radius (Figure 1.9.2.7A and B). The composite profiles provide insight into the evolution of the vertical wind profile, as it transitioned from a well-mixed shape at large radius to a more pronounced low-level wind speed maximum with the approach of the eyewall and the surface RMW. When examined within a scaled radial framework, the jet-like feature was far less evident within total and tangential wind speed profiles. The differences were to be expected given that K2001 and Kepert (2006a, b) have shown that the wind profile has some dependence upon storm-size through the shape of the radial wind profile. The radial stratification likely includes this influence whereas it is removed when scaled by the surface RMW.

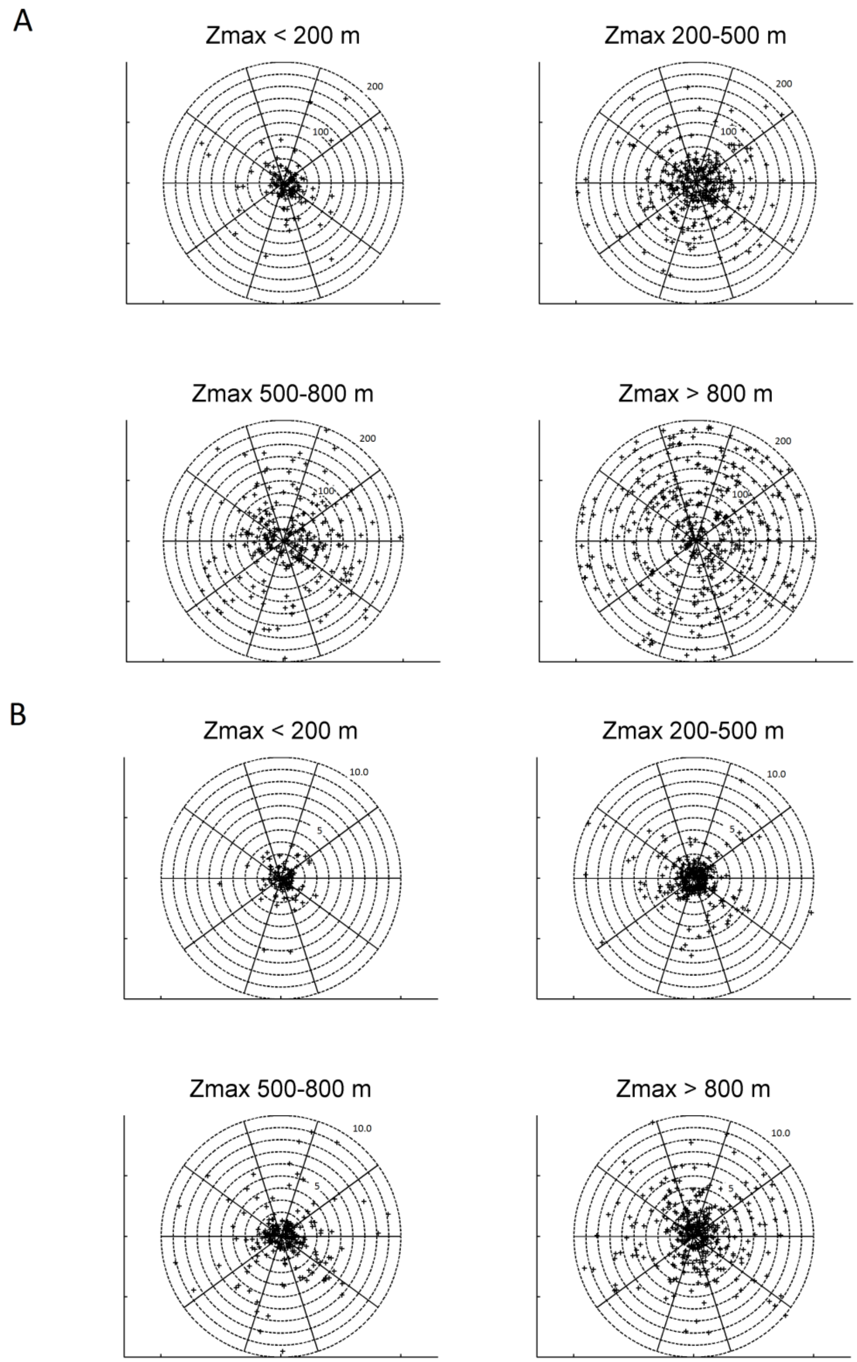

Figure 1.9.2.5. Plan / storm-relative view of GPS sondes and the altitude of their associated wind speed maximum (Z_{max}) for (A) un-scaled radius with range rings (dashed) representing intervals of 20 km and (B) radius scaled by the estimate of the surface RMW with range rings (dashed) representing intervals of 1.0. Azimuthal sectors (solid) are denoted in 30˚ intervals.

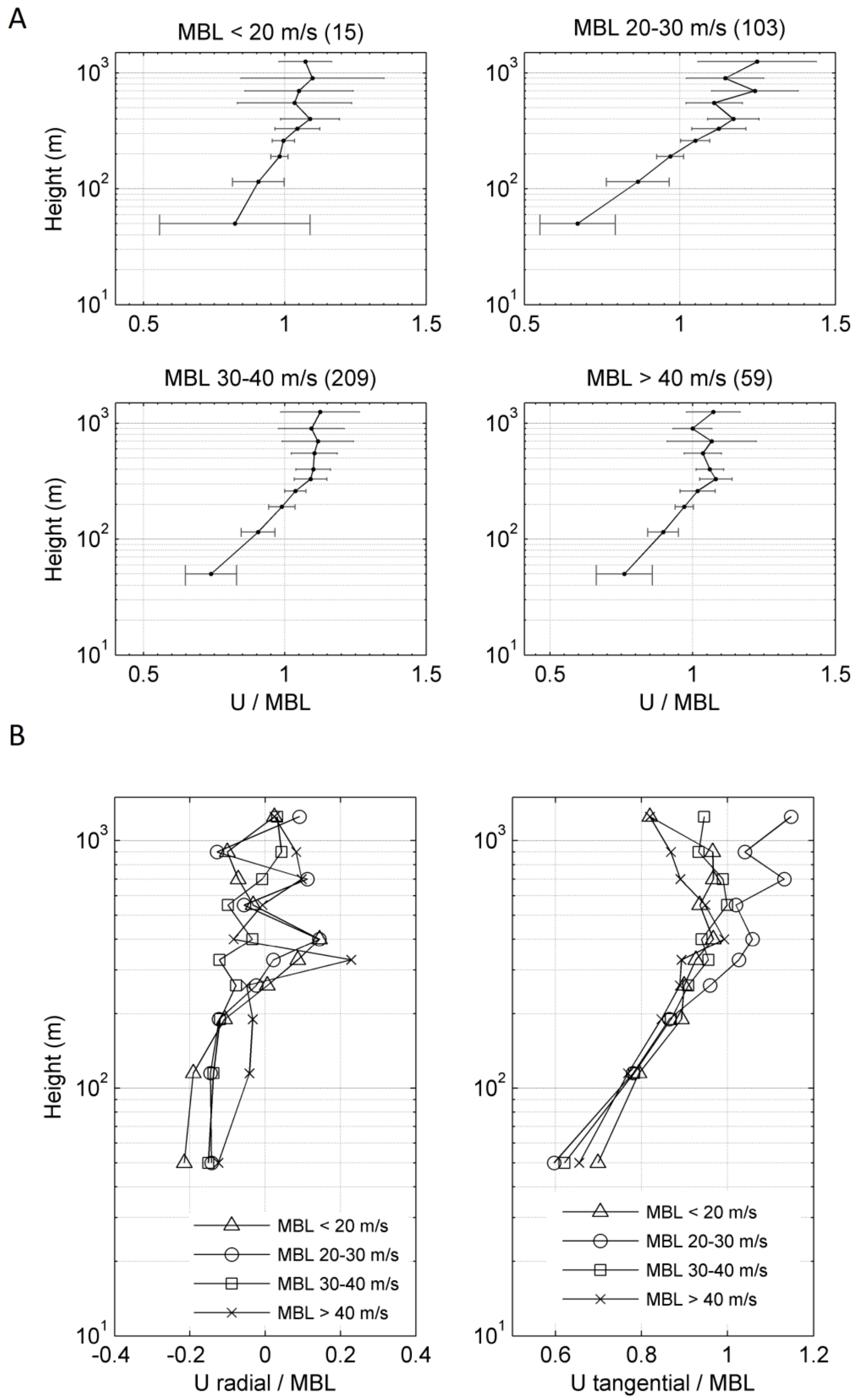

Figure 1.9.2.6. VAD composited profiles for (A) total wind profiles , (B) tangential and radial wind profiles for MBL wind speed groups. Error bars represent ± 1 standard deviation from the mean. The number of VAD profiles included in each composite is provided in parentheses.

1.9.2.3.c. Eyewall/Outer Vortex Structure.

Eyewall profiles for on and offshore flow contained a low-level wind speed maxima near 350 m altitude, whereas the outer-vortex profiles showed a nearly logarithmic increase in wind speed through the depth. Interestingly, the eyewall/offshore regime yielded a slightly stronger scaled wind speed maximum relative to the eyewall/onshore grouping. The eyewall/offshore flow regime also maintained a higher slope in the lowest portion of the profile, which is likely due to frictional effects associated with a large overland fetch. The result differed from that observed using the scaled radial stratification to produce the composites. This was driven by a large number of eyewall profiles from Hurricane Ike (2008), in which the surface RMW was located radially outward from the eyewall reflectivity maximum. The two outer-vortex profiles were similar above 200 m but with differences in the slope of the lower portion of the profile. Once again, this was likely a result of the differences in overland fetch between the two flow regimes.

1.9.2.3.d. VAD Wind Speed Maxima.

Absolute wind maxima within the VAD profiles were examined to determine if a similar relationship was found between the maxima and radial distance. As was found within GPS sondes, the scaled magnitude of the absolute wind speed maximum typically increased with larger radial distance (Figure 1.9.2.8A and B) with a simple linear trend explaining 60% of the variance. A similar relationship was also present when the absolute maxima were presented as a function of a scaled radius. The relationship between the height of the wind speed maximum and radial distance was influenced by the relative coarse resolution of the VAD wind profiles compared to that of GPS sondes. The lowest absolute maxima were typically found near and radially inward from the surface RMW. However, the passage of rainband features at relatively large radii (well removed from the RMW) produced low-level wind maxima as low as 300 m.

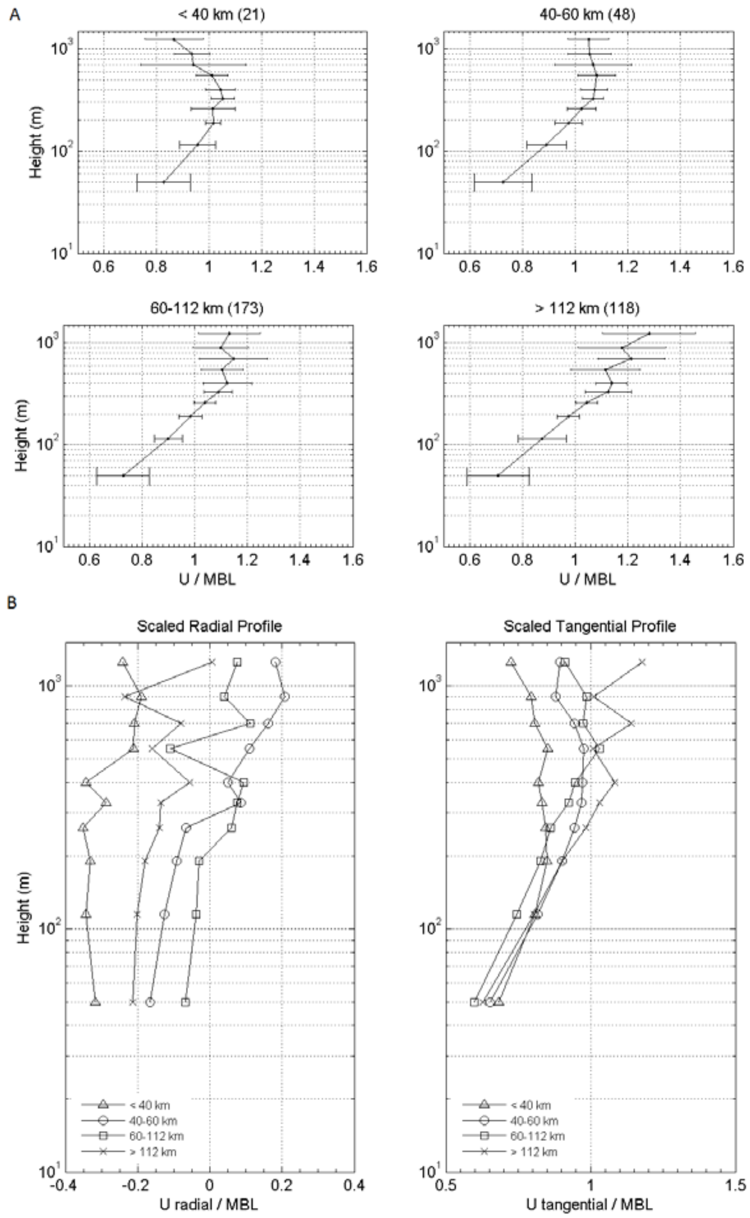

Figure 1.9.2.7. VAD composite profile for (A) total wind, (B) tangential, and radial components for VAD profiles stratified by radius. Error bars represent ± 1 standard deviation from the mean. The total number of VAD profiles used in the composite is provided in parentheses.

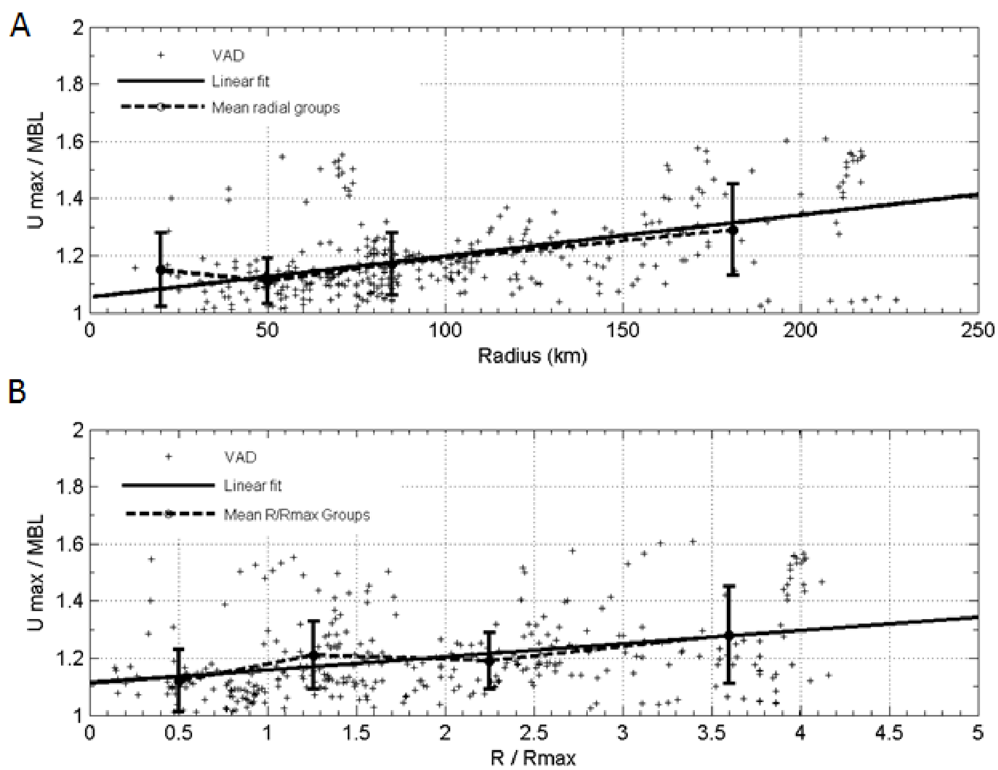

Figure 1.9.2.8. VAD profile absolute wind speed maxima (U_{max}) normalized by MBL wind speed shown as a function of radius (A) and radius scaled by the surface radius of maximum winds (B). The respective least-squares linear fits are shown (solid) and the mean for the VAD profiles grouped by radius and scaled radius (dashed). Error bars represent ±1 standard deviation from the mean.

1.9.3. Conclusions.

A large dataset of vertical wind profiles from tropical cyclones was assembled in an effort to understand the general characteristics and evolution of the wind profile. More than 1000 GPS sondes and 330 VAD wind profiles were included in the analysis. The information obtained from this study provides insight into the change in the vertical wind profile with radial distance and storm-relative azimuth. The diagram shown in Figure 1.9.3.1 describes the general evolution of the vertical wind profile over water moving toward the cyclone center.

The VAD derived landfall composite profiles are similar to the composite GPS sonde profiles and showed a transition from a well-mixed profile to a defined low-level wind speed maximum near the eyewall and radius of maximum winds. The lowest absolute wind speed maxima at landfall are typically found radially inward from the surface RMW. The similar results from two vastly different roughness regimes argue that tropical cyclone dynamics govern the general reduction in boundary layer depth and the height of the mean wind speed maximum.

Upon investigation of individual GPS sonde and VAD profiles and their scaled wind speed maximum, an interesting relationship was found. The magnitude of the scaled wind maxima exhibited a decrease with decreasing radial distance. The largest departures from the MBL wind speed were found at large radii, well removed from the surface RMW. Below 500 m, the wind speed maximum is captured within the layer below 500 m; however, a more steeply sloped profile would still result in a large perturbation from the scaled maximum. The result provides a link to the results of Schroeder et al. 2009 which found extreme near-surface gust factors (> 2.0) were confined to large radii (where mean wind speeds were minimal), with a reduction in magnitude toward the tropical cyclone center. Applying the hypothesis put forth by PVR2003 that the wind speed maximum aloft represents the upper bound of surface gust magnitudes, the reduction in the relative momentum available for vertical transport at small radii near the RMW may contribute to the reduction in gust factors. Well outside the RMW at large radii, the available relative momentum associated with the wind maximum is much larger; therefore, larger surface gust factors are found. These are of little importance within the engineering community as they occur within a relatively low wind speed environment.

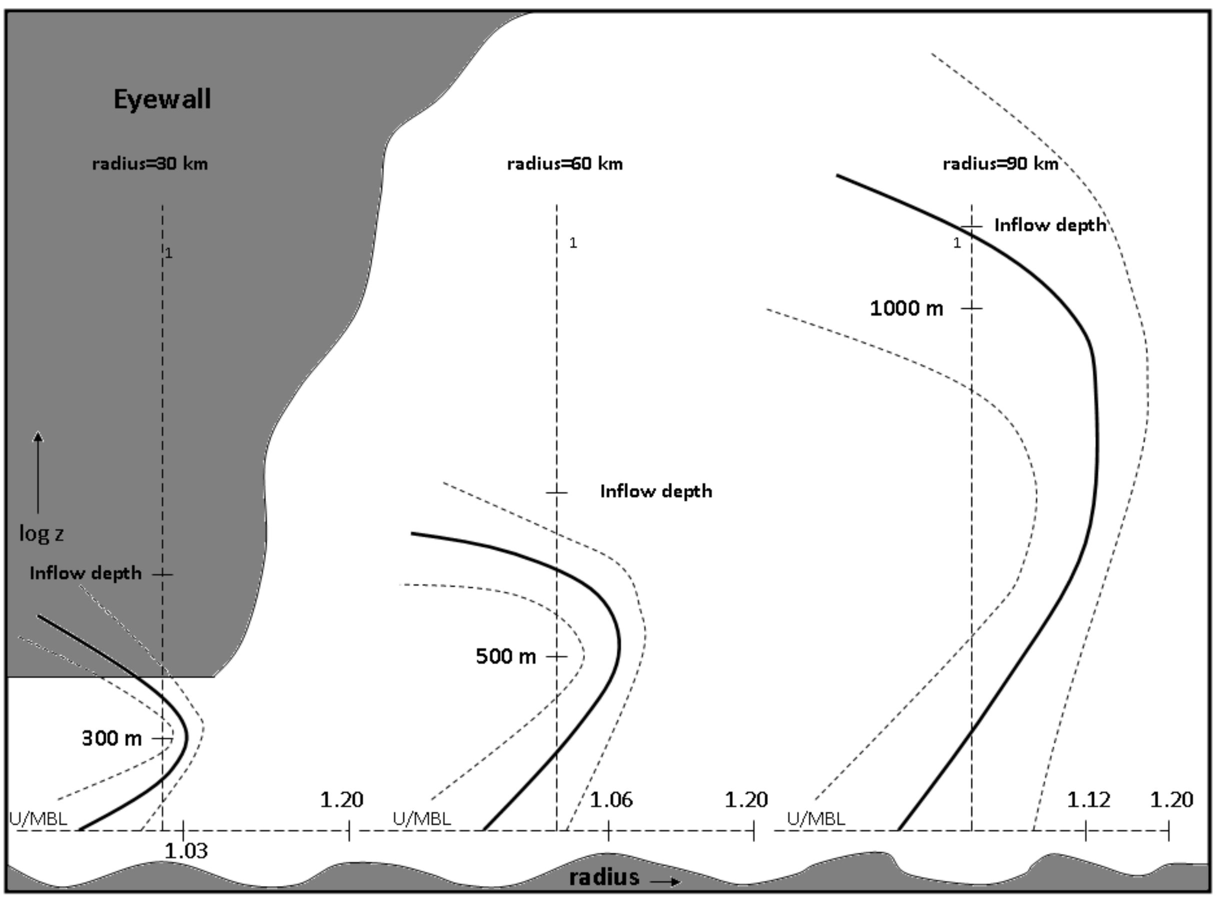

Figure 1.9.3.1. Schematic summarizing the general change in the mean vertical wind profile and the ± 1 standard deviation envelope with respect to radial distance for a typical tropical cyclone. The eye is on the left with increasing radial distance to the right. The mean wind profile is scaled by MBL wind speed. Also denoted is the typical inflow layer depth observed by GPS sondes.

Subtask 1.10: Investigate the Augmentation of Wind Power Systems with Solar Energy.

1.10.1. Introduction.

Over the past few years, there has been minimal research in collocating wind and solar on a utility scale. Previous work has concentrated on small, off-grid structures and homes that are located in remote settings where placement of electric lines become cost prohibitive. By employing small DC wind turbine(s) near the residence and including several photovoltaic panels on the roof and walls along with energy efficient appliances, a small building can operate indefinitely off-grid. Data on these types of studies can be at small time intervals and therefore are robust in their PV energy estimations. However, the wind turbines are small and only a few meters above the surface so the wind data at current utility scale hub-heights is not available. Other wind and solar PV studies that have been done on a utility scale are individual studies that are either wind or solar, but not both at a single site. Only recently have two studies been compiled and released: one by the National Renewable Energy Labs (NREL) called, “How do Wind and Solar Power Affect Grid Operations: The Western Wind and Solar Integration Study,” and one by Clean Energy Associates titled, “Assessment of Wind/Solar Co-located Generation in Texas.” While these studies did address collocating wind and solar generation, they were performed at low resolution, using hourly or daily wind speed and solar insolation averages. This method does not follow the load accurately.

The software written for these models could be easily adapted to any location given collocated wind and solar data. Sun azimuth angles would also need to be accounted for at the new location to obtain accurate solar production estimations. To account for the altitude-adjusted power curve, temperature, humidity, and pressure data would need to be recorded at the same time-scale as the wind data. In the absence of actually building a utility-scale project, short time scale (5 minutes) estimates of combined power production are difficult to simulate due to the lack of hub-height wind data combined with on-site solar insolation data available in similar time scales. This study employed hub-height, high-fidelity, wind data from TTU’s 200-meter meteorological tower combined with a co-located solar pyranometer to estimate short-term (5-minute) power production data. This analysis addresses fixed-plate, single- and dual-axis PV arrays.

This study also includes an economic analysis of the wind-only, solar-only, and combined wind-solar plants. Over the past few years, renewable energy has entered the electrical grid at an exponential rate. To reduce the uncertainties for the grid operator, wind power plants “firm” their production under power purchase agreements (PPA’s) paying penalties when the “firm” production is not met. This puts more risk on the wind power provider in order to secure a higher sale price. Since wind power is best at night and solar power is only during the day, by combining their synergies, uncertainty is reduced and higher PPA’s are possible. This analysis will present economic estimates of the ability of plant operators to secure higher purchase prices for power by raising the “firm” production level and reducing the uncertainties.

1.10.2. Results and Discussion.

This study examines the performance and economics of combining wind and solar photovoltaics into a single renewable power plant. Wind only, solar only, and combined plant models were the basis of comparison. Given the high-fidelity data afforded by the WTM and the TTU's 200-meter tower, highly accurate wind and solar energy production can be estimated. By using the 200-meter tower to accurately estimate air density and wind speeds at wind turbine hub-height, and determining energy production from density and air velocity, highly accurate wind energy production was estimated for the year 2009. Based on data and estimations, a wind-only power plant consisting of 1 MW turbines would have produced approximately 3,564 MWh per turbine after taking into consideration the associated losses. Costs were valued at $2,211 per kW installed, $2.2 million per MW. A pro-forma analysis was also done as a comparison tool for other models. The estimated PPA used was $57 per MWh. Solar production was estimated utilizing five-minute averaged data from the West Texas Mesonet's global-horizontal solar insolation data from the Reese Mesonet site located just south of the 200-meter tower. One MW of AC power was estimated using fixed solar panels. Single- and dual-axis models were also estimated. For each analysis, panel costs were calculated using $2.25 per Watt while non-module costs varied by arrangement. For fixed PV, this was $2.90 per Watt, single-axis PV non-module costs were $2.95 for the added hardware and software, and dual-axis PV used $3.01 for nonmodule costs. In each instance, the currently active Treasure Bill 1630's 30% cash-back incentive would lower costs considerably.

For the combined wind-solar plant, several design options were investigated. The Supplementary Option one, limited exportable production to 1 MW as the two power sources shared the pad-mount transformer. For Supplementary Option two, each power source was then estimated with its own transformer but functioned on an under-designed collection system. Supplementary option three also functioned on under-designed collection but shared a 2 MW transformer. Lastly, an Integrated Design option was utilized and a properly sized collection system and optimized costs were used as well as allowing the two technologies to share a 2 MW transformer. This proved to be the better choice as their increased production and summary costs are shown in Table 1.10.1.1.

Table 1.10.1.1.. Summary table of each model's estimated production, installed costs, and first year ICC/AEP.

1 Year Compare	MWh Prod.	Cap Factor	Est. Cost w/o T-1603	cost/Watt AC w/o T-1603	One-year ICC/AEP	Est. Cost with T-1603	cost/Watt AC with T-1603	First-year ICC/AEP	Wind-Normalized ICC/AEP
Wind	3,564	40.7%	$2,120,000	$2.12	$0.60			$0.60	1.00
Fixed Solar	1,687	19.3%	$5,303,750	$5.15	$3.14	$3,712,600	$3.61	$2.20	3.70
Single-Axis	2,235	25.5%	$4,809,090	$4.94	$2.15	$3,366,363	$3.46	$1.51	2.53
Dual-Axis	2,341	26.7%	$4,665,830	$4.95	$1.99	$3,266,081	$3.47	$1.40	2.35
Wind/Fixed	4,836	55.2%	$7,393,715	$3.64	$1.53	$5,832,600	$2.87	$1.21	2.03
Wind/Single	5,122	58.5%	$6,899,090	$3.50	$1.35	$5,486,363	$2.78	$1.07	1.80
Wind/Dual	5,182	59.2%	$6,755,830	$3.48	$1.30	$5,386,081	$2.77	$1.04	1.75

It was determined that the wind and dual-axis combined systems was the best selection for both the Supplemental and Integrated Design options and a pro-forma financial analysis was completed for this case.

Adding storage to the combined systems in order to increase revenue was the last step in this study. Battery storage was only applied when the 1 MW transformer was the limiting factor. Utilizing solar-specific storage batteries and adjusting the output values at which the storage would be used, allowed several possibilities. Setting the minimum power output at a low level reduced the number and duration of night time periods of zero-power output. However, instead of setting the storage output power value at a minimum, setting it at a higher level would provide added support at a time when outgoing power began to drop. This would provide additional time for the plant operator to make applicable adjustments.

The final possibility is operating under a merchant plan, where a plant operates without a PPA contract and supplies power at the current market clearing price of energy rate. This creates considerable risk for the plant operator, but can reap substantial rewards for short periods of time. By applying the marginal clearing price of energy (MCPE) of the northern region of ERCOT to each model, the estimated annual revenue was calculated. Due to there being so many possibilities of varying systems and transformer sizes, only a few were compiled in chart form and can be seen in Table 1.10.1.2.

Table 1.10.1.2. Summary of energy models operating under a merchant plan and the associated average cost of energy.

1 Year Compare	MWh Delivered	$57/MWh	$99/MWh	$165/MWh	Merchant Plan	Average MCPE/MWh
Wind	3,564	$ 203,148			$ 97,767	$ 27.43
Fixed Solar	1,687	$ 96,159		$ 278,355	$ 58,447	$ 34.65
Single-Axis	2,235	$ 127,395		$ 368,775	$ 76,299	$ 34.14
Dual-Axis	2,341	$ 133,437		$ 386,265	$ 79,254	$ 33.85
Wind/Fixed	4,836	$ 275,652	$ 478,764		$ 148,017	$ 30.61
Wind/Single	5,122	$ 291,954	$ 507,078		$ 153,508	$ 29.97
Wind/Dual	5,182	$ 295,374	$ 513,018		$ 155,283	$ 29.97
W/DA Storage	5,198	$ 296,286	$ 514,602		$ 155,775	$ 29.97
Early Use	5,262	$ 299,934	$ 520,938		$ 157,992	$ 30.02

2.0 MW Trans	MWh	$57/MWh	$99/MWh	$165/MWh	Merchant	Average MCPE/MWh
Wind/Fixed	5363		$530,937		$ 159,925	$ 29.82
Wind/Single	5904		$584,496		$ 177,183	$ 30.01
Wind/Dual	6005		$594,495		$ 180,125	$ 29.99

Selling power under a merchant plan is a difficult process as price agreements must be made every fifteen minutes. Under the “smart grid” and the nodal system, this could increase to every five minutes making it an arduous process. If storage were used under a merchant plan, significant amounts of stored power could be made available during the evening or early morning. When prices escalate for short time periods, the stored energy could be released at a significantly higher price. One thousand $400 batteries could be set aside and used specifically for this purpose, storing 2.9 MWh of energy. When demand increases causing prices to jump to $500 or more per MWh, the batteries could release their energy at substantial revenue to the power plant, paying for themselves at a faster rate than under any of the combined systems mentioned above.

1.10.3. Conclusions.

Based on all options and models above, the best hybrid power production plant is to combine wind with dual-axis PV on a shared 2 MW transformer. This can be implemented in currently operating wind farms (Supplementary option) as the solar panels and hardware are placed to the south of each turbine. Each array would have its own inverter and then tied into the existing collection system. The dual-axis system would be most beneficial in higher latitudes as the sun rises earlier and sets much later during the summer months, creating more opportunities for power production. A plant operator using the Supplemental Option would need to carefully curtail wind power output when the combined power production exceeds the carrying capacity of the collection system or sub-station. Unless specific software is developed allowing significant discharge when prices are high, storage has a high cost-to-benefit value. At the 2009 pricing, the Merchant Plan is not a viable option. It is recommended that a PPA is established. For a currently active wind plant adding solar to firm its delivery of power, it must be able to renegotiate its current PPA at a higher price or the added solar will become a detriment financially to the plant instead of an asset. If plans are being prepared for new wind power facility, early changes in the collection system and sub-station could substantially increase revenue far beyond just the addition of solar to an existing wind farm. Estimated revenue for the Integrated Design increased 16% over Supplemental Option one.

Task 2: Research & Development: Integrated Wind-Water Desalination Systems.

Task 2 was dedicated to research and development of coupling wind power with water treatment technologies to lower the energy costs associated with desalination.

Subtask 2.1: Complete, Maintain and Monitor a 50-kW Wind Turbine and RO Equipment for Demonstration of an Integrated Wind-Water Desalination System.

2.1.1. Introduction.

Municipalities in the Texas High Plains (THP) face ongoing challenges as they plan for long-term water supplies for their citizens. All of these municipalities depend on the relatively shallow and typically fresh Ogallala aquifer for all or part of their potable water. Long-term irrigation withdrawals in excess of recharge in the THP have led to steady depletion of the Ogallala aquifer. Based on local water level declines observed from 1990 to 2004, researchers at TTU Center for Geospatial Technology (CGST) applied geographic information system tools to estimate and map the time until the local saturated thicknesses get too thin (< 30 ft) to allow sufficient pumping rates to supply center pivot systems (CGST 2006). For much of the Southern High Plains (SHP) of Texas, south of Amarillo, only 30 to 50 years remained after 2004 for traditional irrigated agriculture, and municipalities may have to expand or relocate their well fields.

More recently, many public water supply systems in the THP have been reminded by the Environmental Protection Agency (EPA) and the Texas Commission for Environmental Quality (TCEQ) that their groundwater-based supplies are out of compliance with federal standards. Typically, Ogallala groundwater has received only disinfection prior to distribution. In the SHP, many local well waters exceed primary or secondary drinking water maximum contaminant levels (MCLs) for fluoride, arsenic, total dissolved solids (TDS), and other chemicals. We previously collected information on 40 cities from the TCEQ and the New Mexico Environment Department (NMED) files to check the exceedances in at least their worst water supply well (Swift et al. 2009). Most of these communities used Ogallala water, but some used other local shallow aquifers. Overall, 39 of the 40 cities had one or more exceedances (Table 2.1.1.1). These results indicated that, even with their existing groundwater, these cities are likely to require more involved treatment processes beyond disinfection to reduce the target constituents below the MCLs. Added treatment capability will require new infrastructure and operation and maintenance costs, including electricity.

As these issues of decreasing freshwater supply and water quality compliance were being noted, the Texas Water Development Board (TWDB) started the Brackish Groundwater Desalination Initiative in 2004 to facilitate use of brackish groundwater across the state, such as the Dockum or Santa Rosa aquifer beneath the Ogallala in the THP (Arroyo 2011). The TWDB's Innovative Water Technologies program cooperates with the U.S. Bureau of Reclamation's Desalination and Water Purification Program, originally authorized by the Water Desalination Act of 1996. In 2005, researchers from the TTU NWI and Water Resources Center (WRC) began to explore the potential for connecting locally-owned renewable wind energy systems with the electrical needs for pumping and treating brackish groundwater. Electricity can be 30 to 50 percent of the total cost of RO treatment, and renewable wind energy is readily accessible in the THP, so we began to investigate the potential for combining locally owned community wind systems with rural municipalities' water production, treatment, and distribution infrastructure requirements.

The intent was for behind-the-meter application of the renewable energy to reduce the community's grid electricity needs when the wind is sufficient, with the possibility of shifting a significant portion of the electrical needs associated with drinking water delivery to that same time window, essentially storing lower cost energy in the produced water (Swift et al. 2009). Figure 2.1.1.1 provides a conceptual sketch of the addition of a brackish water production and treatment system to an existing municipal water system. It should be noted that concentrate management is another significant issue with any RO or desalination system, especially at inland sites that cannot just discharge to the ocean.

Table 2.1.1.1. Summary of Municipal Supply Exceedances.

Parameter	Number of Cities
TDS	33
Fluoride	29
Arsenic	24
Sulfate	14
Chloride	10
Nitrate	10
Gross	8
Iron	2

Through public outreach workshops, the research team was approached by officials of the City of Seminole, Texas, whose 6,300 residents depended on a declining Ogallala well field impacted by arsenic and fluoride. The Seminole area is known for its irrigated agriculture and oil and gas production, so the City officials were comfortable with drilling deeper wells into the Dockum group to tap the interbedded sandstones and gravels known locally as the Santa Rosa aquifer. The depth(s) to the producing zone(s), water quality, and potential well flow rates were not well known locally, but recent expansions of wind turbine installations in the region were encouraging. The NWI and WRC research team partnered with the City to develop and deploy a field-scale demonstration project. It was necessary to leverage multiple sources of funds, and municipalities in Texas have access to some federal pass-through funds and state funds through different state agencies. The City purchased the project site and provided the electrical connection to the grid. The City will retain the infrastructure at the site and be responsible for its day-to-day operation. The Renewable Energy Demonstration Pilot Program in the Texas Department of Agriculture (TDA) provided a large portion of the project funding. The TWDB provided most of the funds for the Dockum well, with the balance coming from the TDA grant and the Llano Estacado Underground Water Conservation District (LEUWCD). The State Energy Conservation Office (SECO) and TDA provided the funds for the wind turbine purchase. The NWI and WRC partners contributed funds from this multi-year Department of Energy (DOE) project for consultant services, the RO system, and TTU personnel. AJ Howco Services provided overall coordination for contractual and financial requirements.

At the inception of the project in 2005, the primary reference describing the Dockum aquifer was by Bradley and Kalaswad (2003), who had collected all the previous reports and data held by the TWDB and others. Ewing et al. (2008) built on that work and others to generate a map of the areal extent and TDS distribution of the Dockum aquifer in Texas. Of course, when the fresher Ogallala aquifer, which overlies the Dockum, was available, the landowners and industrial water consumers had no reason to tap the lower aquifer, so much less is known about the Dockum aquifer locally. The map did indicate that the Dockum TDS was above the 5000 mg/L level near Seminole, according to a few historical data points near the project site from the water-based literature. The state database also had little lithological information to go with the historical water samples, so the number and position of water-bearing zones in the Dockum was unclear. Anecdotal information from local well drillers indicated that at least two different water-bearing layers might be encountered, one at less than 1000 ft of depth below ground surface (bgs) and a second near the bottom of the Dockum at about 2000 ft bgs.

2.1.1.1. Technical Approach and Hypothesis.

The project objectives included obtaining funding from various agencies and grants, planning and installation of a new well in the Dockum aquifer, selection and installation of an appropriate RO system, selection and installation of a 50-kW wind turbine, design and construction of other site infrastructure, and initiating appropriate operations to collect and report useful data from the demonstration project. The project hypothesis was that the existing technologies for wind energy generation, deep well pumping of brackish groundwater, and RO treatment could be integrated into a system to provide potable drinking water. The entire demonstration project was constructed during the DOE funding duration, and the demonstration continues into 2014.

2.1.1.2 Methodology.

The location for the brackish groundwater well, referred to as SR-1, was set by the City at latitude 32º 41' 06.415"N, longitude 102º 40' 0.727"W, at the local elevation of approximately 3300 ft above mean sea level. This site is located within 510 ac on the south side of Seminole recently purchased for installation of additional Ogallala water supply wells. Cirrus Associates (Cirrus 2009) evaluated available nearby geophysical logs and constructed north-south and east-west cross sections to describe the subsurface conditions and project potentially productive zones in the Dockum aquifer prior to the procurement of the drilling contract. Cirrus (2009) identified two possible productive zones, from 450 to 580 ft bgs in the upper Dockum (Trujillo Formation) and from 1440 to 1840 ft bgs in the lower Dockum (Santa Rosa horizon).

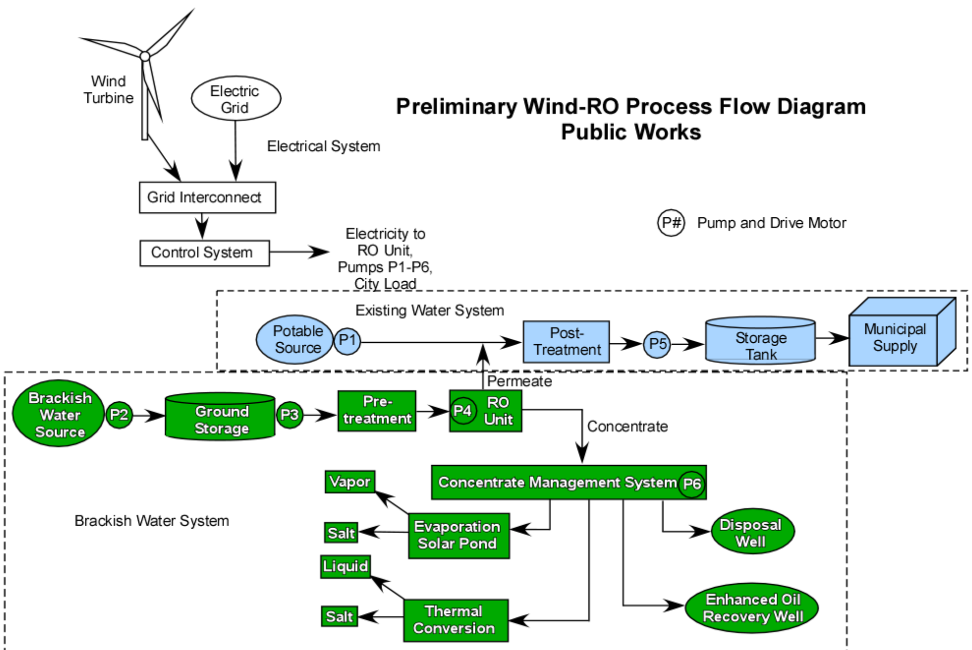

Figure 2.1.1.1. Integrated wind-RO layout for an inland municipality (Swift et al. 2009).

The drilling contract was awarded to West Texas Water Well Service (WTWWS) for an 1800-ft well, and the drilling was completed in July 2011. To protect the shallow Ogallala aquifer, 12.25-in steel surface casing was placed and cemented in a 17.5-in hole to a depth of approximately 274 ft, terminating about 100 ft below the base of the Ogallala and the underlying Cretaceous layer. An 11-in hole was advanced below to a total depth of 1808 ft, and a 7-in steel casing was installed and cemented. Cirrus (2011) collected samples for the geologic log. Geophysical gamma and neutron porosity logs were run by E-P Wireline/Schlumberger. The most promising zones were noted from 540-650 ft, 890-920 ft, and 1610-1770 ft. The three zones were perforated with two perforations shot per ft.

WTWWS performed well development and pump testing in early August. The initial depth to water was 743 ft which was below the uppermost perforated interval. A 36-hr pump test was performed with the pump intake set at 1600 ft. The drawdown stabilized at approximately 180 ft in less than 30 min with a flow rate of 150 gpm. The pump was then turned off, and the depth to water recovered 746 ft within 30 min. The stable pumping rate of 150 gpm was three times the target of at least 50 gpm planned for the demonstration project. The position of the water column in the well allowed the pump intake to be set less than 1000 ft from the ground surface, within the range of commercially available water well pumps. The pump selected was a Grundfos Model 85S200-18, 20-hp pump to deliver 50 gpm at 900 ft of total dynamic head. An unofficial water sample was found to have TDS of 7130 mg/L, and it was unclear how waters from one or more producing zones might be mixing. An In-Situ Data Troll® was installed downhole just above the pump to monitor water level (as proportional to pressure head), temperature, and electrical conductivity (which can be converted to TDS) over time. The datalogger was set to record data on 15-min time intervals.

Engineers from Parkhill Smith and Cooper, Inc. (PSC) were retained to produce the well specifications according to TCEQ requirements and assist in the procurement process. The specifications required a complete operational skid-mounted RO system to treat an inflow of at least 50 gpm of brackish water to meet the TCEQ's primary drinking water standards, with pretreatment capability for cartridge filtration, pH adjustment, and antiscalant addition. The target recovery factor was at least 70 percent with a salt rejection rate of 95 percent and minimum membrane life of two years. The system was purchased from Crane Environmental in December 2010 with TTU DOE funds. Concentrate management alternatives considered included an evaporation pond, additional RO for the concentrate flow, and discharge into the City's wastewater collection system. After discussion with PSC and the City staff, the choice was to simply blend permeate and concentrate flows in a lift station and pump the mixture into the City's sewer system for simple dilution. The lift station and associated sewer line were designed by West Texas Consultants (WTC), as well as a 30 ft by 30 ft metal building to house and the infrastructure between the well and the RO system, and all construction was done in 2012. Electricity from the local grid was also included, so that the well and RO system could operate continuously. A data acquisition system will be installed in the near future.

The 50-kW wind turbine was purchased from Entegrity Wind Systems (EWS). EWS partnered with WTC and construction contractors for the site engineering and installation. The turbine's nacelle and blades were supported by a 100-ft galvanized steel lattice tower, and the blades were 23.7 ft long, resulting in a rotor diameter of 49.2 ft at a centerline hub height of 102 ft. Both the wind turbine and the local electrical grid were connected to the RO building with two separate meters so that the contributions of both sources can be tracked. During the demonstration period, the well and RO system will be run continuously, using renewable wind energy when available and grid electricity otherwise. The seasonal variations in wind energy generation are of primary interest. The wind turbine became operational in March 2013.

2.1.2. Results and Discussion.

Surprisingly, the static water level in SR-1 rose from its initial 740 ft bgs after drilling and development to about 96 ft bgs over several months. The certified cementing of the surface casing must prevent any inflow to SR-1 from the shallower Ogallala aquifer, so the higher water level must have been caused by the pressure in one of the three perforated zones. It was unknown whether the static water level would persist during continuous operation or drop back to the 740 ft bgs noted after development. Hydraulically, the water level in SR-1 typically dropped about 200 ft or more when the pump was on, then returned within an hour or so to the 96 ft bgs. Under these conditions, the intake side of the well pump experienced much greater pressure than expected, such that the discharge flow rate and pressure were much higher than the 50 gpm and 10-15 psi expected by the variable speed booster pump between the well pump and the RO system. The response to this unexpected condition was installation of a variable speed drive and pressure transducer to control the well pump, reducing the motor speed from 60 Hz to 35 Hz for proper flow and pressure of 40 to 60 psi to the RO system.

Continuous operation of the complete system began on April 18, 2013, starting with a 24-hr test period with the direct assistance of the Crane Environmental field representative overseeing the City of Seminole water utilities staff. The team monitored system performance on the RO system's touch-screen monitor, which reported permeate and concentrate flows, pressures, conductivities, and pH values, as well as the incoming raw water conductivity, pH, pressure, and temperature. A hand-held Myron L™ water quality instrument provided an alternate means of checking conductivities and pH values with grab samples from various sample valves around the system. As the system ran over the first 24 hours, the team noted that the incoming raw water TDS slowly rose from 2300 to 8000 mg/L as the water from the different zones mixed within the well. The permeate and concentrate flow rates settled at 40 and 14 gpm, respectively, for a recovery rate of 74 percent, and permeate TDS stabilized at about 450 ppm.

The system ran continuously until May 2, when the well pump motor failed due to an electrical ground fault. The pump and motor were pulled by a local pump contractor, who then ordered a replacement 20-hp motor. The new motor and pump were reinstalled on June 14, and the complete well and RO system were restarted on June 17. Even after being idle for six weeks, the RO system's operating conditions stabilized to the same flow and parameter values established previously. Table 2.1.2.1 compares feed and permeate water qualities from samples collected on June 24, 2013, as determined in an EPA-certified laboratory. The combined electrical loads for the RO system, well, and building were typically less than 15 kW, less than 20 kW generated by the wind turbine under normal wind conditions. The complete system ran smoothly until August 7, when a nearby lightning strike interrupted all the site's devices. The City staff got the system running again, but the outage apparently caused some operational difficulties in water quality and flow meters on the RO system, so the operational data were questionable. At the time of this report, a repair visit from technicians affiliated with Crane was just completed, with most of the problems repaired but some details remaining. The TTU research team and City staff are working to get all remaining problems resolved and then will perform the official 12-mo demonstration while collecting operational data on the amount of water pumped and treated, electrical usage from both wind turbine and grid sources, and the performance of the RO system. A final report for the other funding will be prepared in 2014.

2.1.3. Conclusions.

This project demonstrates a new approach to municipal water supply and treatment for west Texas and other inland locations with access to brackish groundwater and wind energy. Multiple sources of grant funds were aggregated from state agencies and local sources, as well as TTU NWI and WRC research funds. This cooperative team was able to provide the well, wind turbine, RO system, and other associated items to produce and treat local brackish groundwater for potential municipal supply. The remote location did lead to significant delays, especially the recent lightning strike, as technical expertise for repairs had to be procured from other locations. It is our intention that this demonstration project will encourage more local business opportunities for advanced water treatment and renewable energy services.

Table 2.1.2.1. Comparison of Feed and Raw Water Qualities.

Analyte	Concentration		Units	Reporting Limit
	Feed Water	Permeate		
Bicarbonate	184	<12.2	mg/L	12.2
Carbonate	<12.0	<12.0	mg/L	12
Chloride	2910	178	mg/L	2.5
Fluoride	<5	<0.5	mg/L	0.5
Nitrite-N	<0.4	<0.04	mg/L	0.04
Nitrate-N	<0.4	0.0718	mg/L	0.04
Sulfate	1780	3.97	mg/L	2.5
Dissolved Calcium	117	<1	mg/L	1
Dissolved Magnesium	49.4	<1	mg/L	1
Dissolved Potassium	14	5.94	mg/L	1
Dissolved Sodium	2830	121	mg/L	1
Total Dissolved Solids	8235	436	mg/L	2.5
pH	7.67	6.35	s.u.	2
Total Silica	8.72	<0.5	mg/L	0.5
Total Aluminum	<0.05	<0.05	mg/L	0.05
Total Arsenic	<0.01	<0.01	mg/L	0.01
Total Copper	<0.005	<0.005	mg/L	0.005
Total Iron	0.571	1.25	mg/L	0.01
Total Manganese	0.402	<0.005	mg/L	0.005
Total Uranium	<0.03	<0.03	mg/L	0.03
Total Zinc	<0.01	<0.01	mg/L	0.01

The DOE and other related agencies should continue their promotion of community-based renewable energy systems. Water production, treatment, and distribution can all be seen as electrical loads that can be scheduled for or supplemented by intermittent renewable energy sources. Local energy storage systems could also be incorporated to reduce grid dependence.

Subtask 2.2: Investigate New Reverse Osmosis Configurations, Energy Storage and Power Electronics to Extend the Development, Application and Demonstration of Integrated Wind Turbine-RO Systems to Purify Brackish Groundwater.

2.2.1. Introduction.

Reverse osmosis (RO) is becoming an important means for sustainable water supply in many regions of the world primarily due to its capability to produce high quality potable water from nonconventional water sources, such as seawater, brackish ground water, and agricultural drainage (Kumar et al. 2006; Rahardianto et al. 2008; Shannon et al. 2008; Committee on Advancing Desalination Technology 2008; Van der Bruggen et al. 2003; Fritzmann et al. 2007). As an energy intensive process, energy (electricity) consumption is one of the major cost components in RO desalination (Zhu et al. 2009; Veerapaneni et al. 2007; Alvonitis et al. 2003; Busch and Mickols 2009; Semiat 2008; Reddy and Ghaffour 2007; Li 2010). A large amount of energy is required to drive the water through the RO membranes in seawater desalination. Brackish water RO desalination usually requires less energy at the same recovery than seawater desalination because of lower salinity (Committee on Advancing Desalination Technology 2008; Zhu et al. 2009; Li 2010). However, recoveries of 75 percent or above are usually required for brackish water desalination for economical operation and due to the difficulties associated with retentate handling and disposal (Van der Bruggen et al. 2003; Gluekstern and Priel 1997; Lie et al. 2012; Liu et al. 2011; Song 2013). Energy consumption in brackish water desalination increases rapidly with increasing water recovery beyond 75 percent. Therefore, minimization of energy consumption is one of the most effective ways to reduce costs in both seawater and brackish water RO desalination for a more affordable means of sustainable water supply.

The principle for RO desalination is that a net (positive) driving pressure is maintained on the feed side of the RO membrane to drive water through the membrane with the salts left behind. Energy is consumed when the raw (feed) water is pushed into the membrane elements by high pressure pumps press at the required pressure and flow rate. The energy requirement in RO desalination is affected by feed water salinity, process configuration, and the operating conditions (e.g., driving pressure and recovery). Although numerous studies have been conducted in the calculation of energy consumptions in the cross flow RO processes, the particular usages or needs of energy in RO desalination processes have not been well analyzed and delineated. The most frequently noted energy requirement of RO desalination (Shannon et al. 2008; Committee on Advancing Desalination Technology 2008; Avlontis et al. 2003) is still the thermodynamic minimum in a reversible (equilibrium) process that was probably first derived by Spiegler (1977) more than 30 years ago. This thermodynamic minimum energy only provides a theoretical limit on the energy consumption in a RO process with an infinitesimal permeate flux.

In this investigation, an ideal RO was defined and introduced for the first time as the most energy efficient RO process for desalination at the required permeate flux, against which the energy efficiency of cross flow RO processes could be more meaningfully assessed and measured. In order to define and quantify the energy requirement for the ideal RO process, the thermodynamic equilibrium RO process was first reviewed for the theoretical minimum energy requirement in desalination. Finally, the energy consumption in cross flow RO, which is currently the predominant configuration in water desalination, was analyzed by splitting it into different components (i.e., the thermodynamic minimal energy, additional energy requirement, and energy remaining in the retentate). The energy efficiency of the cross flow RO process at various recoveries was analyzed and assessed against the reversible and ideal RO processes. It is believed that a better understanding of the energy consumption in the RO desalination processes would be achieved by analyzing the total energy into individual components for different functions or needs that are fundamental to the RO processes.

2.2.1.1. Technical Approach and Hypothesis.

Two baseline energy consumptions, the energy of minimal thermodynamic requirement and energy of ideal desalination for required flux, were first defined and described for RO desalination. Then the energy requirement for the crossflow RO processes, which is the predominant configuration used in practical desalination applications, was determined and compared with the baseline energy consumptions. The underlying assumption is that the energy efficiency can be better assessed with the two baselines (thermodynamic and ideal) rather than one (thermodynamic).

2.2.1.2. Reversible RO Desalination Process.

The thermodynamic minimal energy requirement in water desalination was derived by many researchers for the general revisable separation processes without referring to the specific RO processes (Powell 1964, Lillian 2010). The specific energy (energy required for per unit permeate production) can be calculated by dividing the energy with the permeate volume

$$W_1 = 2.05\times10^{-5} C_0 \frac{1}{R}\ln\frac{1}{1-R} \tag{1}$$

where W_1 is the specific energy for desalination in the reversible RO processes. For convenient use, the energy unit in Eq. (1) is given in kilowatt-hour (kWh) that is equal to 3.6×10^6 Joules. With this leading coefficient, the unit of the salt concentration in Eq. (1) is mg/L.

2.2.1.3. Ideal RO Desalination Process.

It has been demonstrated that a nonzero permeate flux has to be maintained in a practical RO desalination process to minimize the total cost of membrane desalination. An ideal RO desalination process in this study is defined as a RO system that needs the smallest amount of energy to maintain a required permeate flux. If a constant P_{net} is maintained during the operation, going through similar integration steps as for the reversible RO process, the specific energy for the ideal RO process to maintain the required permeate flux is determined as

$$W_2 = 2.05\times10^{-5} C_0 \frac{1}{R}\ln\frac{1}{1-R} + 2.78\times10^{-7}\Delta P_{net} \tag{2}$$

where W_2 is the specific energy for the idea RO process to maintain a required permeate flux. The pressure in Eq. (2) is required in the metric unit of Pa. The first term on the right hand side of Eq. (2) is the amount of energy required to overcome the osmotic pressure, and the second term is the amount of energy needed to maintain the required permeate flux.

2.2.1.4. Cross Flow RO Process.

The practical RO desalination processes are dominantly employing a cross flow configuration with pressure vessels 6-8 m long, in which 6-8 membrane elements are connected in series. Feed water is supplied by a high pressure pump into one end of the pressure vessels, and retentate exits the pressure vessels through the other end. Permeate comes out of the pressure vessels through the third outlet usually placed along the central line. The specific energy requirement for permeate production in the cross flow RO process is

$$W_3 = 2.78 \times 10^{-7} \Delta P \quad (3)$$

where W_3 is the specific energy requirement in the common cross flow RO processes. The pressure ΔP in Eq. (3) is given in the metric unit of Pa. The specific energy in Eq. (3) is the net energy spent on permeate production and does not take into account of the energy remained in the retentate stream. If the retentate is discharged directly without energy recovery, the gross specific energy requirement for permeate production in the cross flow RO process will be higher accordingly.

Unlike in the case of the reversible RO process, the driving pressure in some sense is a free variable in the cross flow RO process, and actually is a primary design parameter in the cross flow RO processes. The key step for energy calculation in cross flow RO is the determination of the driving pressure that will be further elaborated in the following discussions.

2.2.2. Results and Discussion.

2.2.2.1. Energy Diagram.

The energy spent in a cross flow RO process can be analyzed graphically into different characteristic fractions with the help of a pressure-recovery diagram. An example of the pressure-recovery diagram for seawater desalination at a recovery of 60 percent is shown in Figure 2.2.1.1. The horizontal side of the square or rectangle indicates the volume of feed water pumped into the RO channel, and the permeate recovery is indicated by a fraction of the side. The vertical side of the square or rectangle indicates the driving pressure. The area of the square or rectangle represents the total energy used to pump the volume of feed water into the membrane channel. The total energy is divided into two parts by the vertical line passing the permeate recovery. The area on the right side of the recovery line represents the energy remaining in the retentate stream, while the area on the left side of the line is the energy used for permeate production.

The energy for permeate production can be further divided into two parts by the osmotic pressure curve (broken line in Figure 2.2.1.1) of the retentate as a function of the permeate recovery. According to Eq. (1), the lower part indicates the thermodynamic minimal energy for permeate production in a reversible RO desalination process. The upper part represents the additional energy spent in the cross flow RO process beyond the thermodynamic minimal energy. The three energy fractions (thermodynamic minimum, additional energy, and energy remaining in retentate) in cross flow RO were represented by the sizes of the three regions as indicated on the pressure-recovery diagram.

2.2.2.2. Additional Energy Requirement.

Figure 2.2.2.1 shows 40 percent of the total energy remained in the retentate stream at the recovery of 60 percent, which is readily recoverable with energy recovery devices. In the 60 percent of the energy that was spent for permeate production, about 35.6 percent was the thermodynamic minimum energy for permeate production, about 35.6 percent was the
thermodynamic minimum energy for desalination and the rest about 24.4 percent was the additional energy requirement of the cross flow RO process. One main reason for the additional energy in cross flow RO is the practical need for the production of the required permeates flux.

The additional energy in the cross flow RO process increases rapidly with increasing recovery. RO becomes the largest fraction of the total energy for brackish water desalination. The relative amounts of the three energy fractions in cross flow RO at recoveries above 50 percent were listed in Table 2.2.2.1 for salt concentration of 5,000 mg/L and net driving pressure of 0.34MPa (50psi) at the end of membrane channel. It can be seen that the additional energy requirement is greater than the thermodynamic minimal energy requirement for all recoveries.

Table 2.2.2.1. Comparison of three energy components in a cross flow RO process.

Energy component	Recovery (percent)					
	50.0	60.0	70.0	80.0	90.0	95.0
Minimum energy requirement	23.6	26.7	28.2	27.1	21.1	14.3
Additional energy requirement	**26.4**	**33.3**	**41.8**	**52.9**	**68.9**	**80.7**
Energy remained in retentate	50.0	40.0	30.0	20.0	10.0	5.0

2.2.2.3. Energy Requirements in Reversible, Ideal, Crossflow RO Processes.

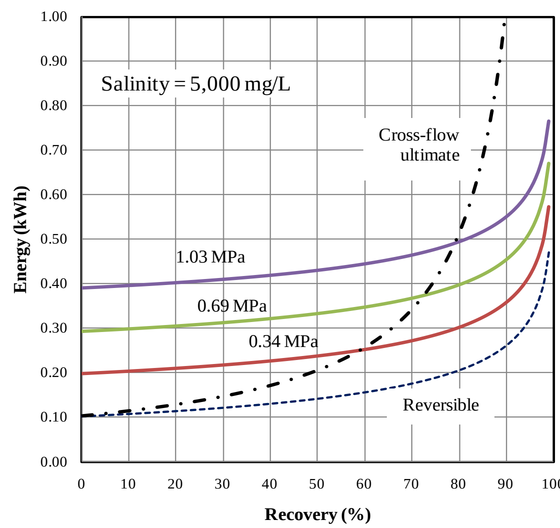

Figure 2.2.2.2. Specific energies for reversible, ideal, and crossflow RO desalination processes.

The specific energy requirements for reversible, ideal, and cross flow RO processes are presented in Figure 2.2.2.2, calculated for brackish water of 5000 mg/L salinity. The reversible RO process means the thermodynamic minimal energy is spent in the desalination process. Net driving pressures of 0.34, 0.69, and 1.03 MPa (50, 100, and 150 psi) were used in the calculations of specific energy for the ideal RO processes at three different levels of permeate fluxes. The ultimate specific energy in cross flow RO indicates the energy requirement for the given recovery regardless of permeate flux. It can be seen that the ultimate specific energy in cross flow RO (broken line) for brackish water desalination increased rapidly with recovery when the recovery was high. The specific energy was 0.5 kWh/m^3 for 80 percent recovery but became 1.0 kWh/m^3 for 90 percent recovery. In contrast, the energy requirement of ideal RO increased much more moderately than that of cross flow RO. For instance, the specific energy of the ideal RO with 0.69 MPa net driving pressure was 0.45 kWh/m^3 for recovery of 90 percent. Specific energy only increased 0.05 kWh/m^3 when the recovery increased from 80 percent to 90 percent. The results indicate that the crossflow RO is not energy efficient at high recoveries. The lower energy efficiency of the cross flow RO at high recoveries is a necessary cost to pay for the benefits of the cross flow configuration, including the continuous operation, concentration polarization reduction, fouling mitigation, and process simplicity.

2.2.3. Conclusions.

There is a serious limitation for the use of the thermodynamic minimal energy as a baseline to assess the energy efficiency of RO processes in water desalination because of the practically zero permeate flux in the thermodynamic reversible RO process. Because a nonzero permeate flux is always required for practical RO desalination processes, the energy efficiency of the RO processes is better assessed against the ideal RO process that represents the most energy efficient desalination process for a required permeate flux.

The energy consumption in the cross flow RO process could be graphically analyzed with the pressure-recovery diagram into three fractions: energy remaining in the retentate stream, thermodynamic minimum energy, and additional energy requirement. The additional energy is needed in the cross flow RO processes to maintain the required permeate flux and overcome the elevated osmotic pressure along the membrane channel. When the cross flow RO is working at low recoveries, the additional energy is mainly used to maintain the permeate flux. Therefore, the total energy requirement for the cross flow RO process is only slightly higher than that for the ideal RO process. However, the total energy requirement for cross flow RO process can be much greater than that for the ideal RO process when it is working at high recoveries.

The DOE and other related agencies should continue their efforts on the promotion of RO processes in brackish water desalination and the improvement of energy efficiency of the processes. The energy efficiency of RO desalination processes has increased significantly in the last two decades but there are still rooms for further improvement. Energy efficiency of RO desalination coupled with renewable energy introduces other challenges.

Task 3: Outreach and Education.

NWI has been active in interdisciplinary educational efforts for many years. NIW offers the first doctoral program in wind science and engineering (WiSE PhD program) established through funding from the NSF IGERT program in 2007. NWI has also developed a graduate certificate in wind energy, consisting of 15 hours of graduate-level coursework. Students may choose either a technical or managerial track. The technical track is calculus and physics-based and focuses on the technical aspects of the growing wind energy field. The existing wind energy curriculum was developed in close collaboration with an industry advisory board consisting of representatives from companies including Vestas, Siemens Wind Energy, Suzlon, Duke Energy, and EnXco.

In 2011, additional funding from the Texas Workforce Commission enabled NWI to conduct a wind energy workforce assessment in collaboration with the Texas Wind Alliance. The assessment yielded important data from Texas wind energy industry employers regarding the required knowledge and skills sets that college graduates must possess in order to successfully enter a career in wind energy. NWI incorporated these industry recommendations into its curriculum.

In fall 2011, the university’s Board of Regents approved the 120-hour Bachelor of Science in Wind Energy degree (BSWE) program. The multi-disciplinary program has strong foundations in science and technology. A significant component of the program will be the capstone courses, WE 4310 Wind Modeling and Design, and WE 4230 Independent Study in Wind Energy. Both courses provide students with extensive hands-on training and “real-world” problem-solving exercises related to the field of wind energy.

The BSWE degree plan also includes a unique Global Component (6 credit hours) designed to provide students with insight into the global nature of the wind energy industry. This program aspect is very critical given the international wind energy job market. Thanks to a recently formed collaboration with the University of Oldenburg and the University of Jade in Germany, WESP students will be able to travel to Germany during the summer to participate in 5 weeks of classes in project management, wind energy technology and international engineering. The program will provides students with the opportunity to interact with students from all over the world as classes are taught in English and students come from various parts of the world to participate in the summer program. Our German university partners will organize field trips to wind farm installations and provide guest lecturers from industry experts.

Beyond these fundamental NWI educational programs, various outreach and education efforts have been continuously performed with support from this award. These efforts, while less distinct relative to the technical research, have played an important role in enhancing awareness of the ongoing activities, as well as in raising the general awareness of wind energy. These efforts took on numerous forms, which, unlike the technical tasks, were not nominally tracked in detail, but are summarized here.

Subtask 3.1: Design and Deliver Workshops, and Organize and/or Moderate Sessions at Technical Conferences.

NWI faculty participated in numerous conferences and professional meetings during the course of the award. Nominally, their participation was to give a technical presentation as identified below in subtask 3.3, but on several occasions, faculty also moderated sessions. NWI faculty also participated and/or organized a number of workshops, short courses and symposiums, including, but not limited to:

1. **Wind Energy Institute**; UT School of Law; "Wind Power Fundamentals"; Feb 07
2. **Wind Energy 101**; Lubbock Chamber of Commerce; Aug 07
3. **Wind Energy Conference**; Fundamental of Wind Energy; Xcel Energy, Amarillo; Aug 07
4. **Community Wind and Water Conference**; TTU; Aug 07
5. **West Texas Wind Energy Consortium**, "Wind Power Basics and Research"; Oct 07
6. **Short Course, "Wind Power Systems**; Oct 07
7. **Texas Renewable Energy Industries Association**; "Wind Powered Desalination"; Nov 07
8. **UTCLE;** Univ. of Texas Cont. Legal Education Seminar, Wind Energy Overview for Texas; Feb 08
9. **UWIG, NREL**, Utility Wind Interest Group and The National Renewable Energy Laboratory, Wind Energy Industry/University Workshop; May 08
10. **Short Course, "Wind Power Systems**", Lubbock, Texas Jun 08
11. **Short Course, "Wind Power Systems",** Sweetwater, Texas; Oct. 08
12. **IEEE Green Technology Conference Short Course,** "Wind Power Systems", April 09
13. **Leadership Texas**, "Future Texas Wind"; July 10
14. **Workforce for Wind Energy,** Texas Renewables 2010, San Antonio, Texas, Nov.10
15. **Workforce for Wind Energy**, Growing Green Conf., TEEX, Odessa, Texas, Dec.10
16. **High Voltage Workforce,** Transmission Summit, TSTC, Sweetwater, Texas, Jan. 11
17. **Wind Energy Overview**, Texas Academy of Medicine, Engineering and Science, Austin, Texas, Jan.11, 2011
18. **Wind-Smith Academy**, American Wind Power Center, Lubbock, Texas, Mar. 11
19. **Research and Workforce needs in Smart Grid Energy Systems**, TTU Workshop, Apr. 11
20. **Wind Energy Workforce**, TTU Wind Energy Law Society, Sep. 11

In 2012, TTU hosted a major symposium on Wind Farm Underperformance with more than 200 participants from around the world. This significant symposium highlighted the research opportunities that exist at the wind plant system level through technical presentations, and was widely viewed as a significant success.

Subtask 3.2: Provide Public Outreach and Educational Activities by Upgrading and Maintaining the Wind Energy Web Components on the NWI Website and by Conducting Facility Tours at Reese Technology Center for Visiting Public, Students, and Dignitaries.

NWI has hosted a wealth of facility tours for widely varying audiences over the term of this award. These tours, typically 15 or more a year, range from federal and state elected officials (i.e. VIPs), to industrial partners, national labs and students of all ages.

Additionally, the entire NWI website has been reconstructed and redesigned allowing for easier access and more intuitive usage. Social media has been utilized to enable NWI to reach target audiences who would otherwise be unreachable, and digital images have been promoted through local and international media. Media coverage has been extensive and both national and international media avenues have been hosted to cover NWI research and its cutting-edge facilities.

Subtask 3.3: Disseminate Research Results through Conference Papers and Presentations, as well as the Submission of Peer-Reviewed Publications.

Text Books:

Karpat, F., S. Ekwaro-Osire, and E. Karpat (2011). “A Virtual Tool for Computer Aided Analysis of Spur Gears with Asymmetric Teeth,” in *Applications of MATLAB in Science and Engineering*, (Editor: T. Michałowski). InTech, Rijeka, Croatia.

Walker, R., and A. Swift (2012). *Wind Energy Impacts: A Comparison of Various Sources of Electricity*. Textbook being written for use in classroom, by public, or wind energy industry. Accepted for publication by John Wiley & Sons.

Swift, A. (2006). *Wind and Water: Redeveloping Regional Resources for the New Economy*. ISBN 0-9745756-1-5. Second Edition.

Reports:

Chapman, J. (2009). “Renewable Energy Futures.” National Renewable Energy Laboratory. Report contribution.

Chapman, J. (2009). “Wind Power and Water Desalination - Technology Integration.” US Department of the Interior (Bureau of Reclamation). July. Report contribution.

Newhouse, C., S. Bole, W. Burkett, P. Nash, and M. El-Shami (2009). “Study of Elastomeric Bearings for Superelevated U-Beam Bridges.” Texas Department of Transportation. October. Final report. Research Project 0-5834-1.

Swift, A., K. Rainwater, J. Chapman, D. Noll, A. Jackson, B. Ewing, L. Song, G. Ganesan, R. Marshall, V. Doon, and P. Nash (2009). “Desalination and Water Purification Research and Development

Program Report No. 146, Wind Power and Water Desalination Technology Integration." Bureau of Reclamation. Final Report. July.

Journal Papers:

Alemayehu, F. M., and S. Ekwaro-Osire (2013). "Uncertainty Considerations in the Dynamic Loading and Failure of Spur Gear Pairs." *Journal of Mechanical Design* 135.8, 084501-1–084501-7.

Basu, S. (2009). "Can the Dynamic Eddy-Viscosity class of Subgrid-scale models capture the inertial-range properties of Burgers turbulence?" *Journal of Turbulence* 10, 1-6.

Cui, L., A. Morse, K. Rainwater, and L. Song (2012). "Modeling of Concentration Polarization in a Reverse Osmosis Channel with Parabolic Crossflow Profile." *Water Environment Research*. Accepted.

Cui, L., A. Morse, K. Rainwater, and L. Song (2012). "Mathematical Modeling of Concentration Polarization in a Reverse Osmosis Channel with Parabolic Crossflow Profile." *Water Research*. Under review.

De-Silva, D., R. McComb, and A. Schiller (2010). "Does More Investment in Green Energy make Pay Checks Greener in Wind Energy?" Submitted to *Renewable Energy and Economic Policy.*

De-Silva, S., T. Hubbard, R. McComb, and A. Schiller (2010). "Firm Entry, Growth and Survival in the Green Industry." Submitted to *Renewable Energy and Economic Policy.*

De Silva, D., R. McComb, and A. Schiller (2011). "Do Production Subsidies Have a Wage Incidence in Wind Power?" *Journal of the European Association of Labour Economics*. Under review.

De Silva, D., R. McComb, and A. Schiller (2012). "Do Production Subsidies Have a Wage Incidence in Wind Power?" *Applied Economics.* In press.

Ekwaro-Osire, S. (2011). "On Spur Gears with Asymmetric Teeth." *Journal of Mechanical Design*. Under review.

Ewing, B. T., J. B. Kruse, and D. Sutter (2007). "Hurricanes and Economic Research: An Introduction to the Hurricane Katrina Symposium." *Southern Economic Journal* 74(2): 315-325.

Ewing, B. T., J. B. Kruse, and M. Thompson (2007). "Analysis of Time-Varying Turbulence in Geographically Dispersed Wind Energy Markets." *Energy Sources, Part B: Economics, Planning, and Policy* 3: 340-347.

Ewing, B. T., J. B. Kruse, and M. Thompson (2007). "A Multidisciplinary Plan for Executive Education and Lifelong Learning Programs in Wind Science and Engineering." *International Journal of Continuing Engineering Education and Life-Long Learning*: 19.1 74-81.

Ewing, B. T., J. B. Kruse, J. L. Schroeder, and D. A. Smith (2007). "Time Series Analysis of Wind Speed using VAR and Impulse Response Technique." *Journal of Wind Engineering and Industrial Aerodynamics* 95 (3): 209-219.

Giammanco, I. M., J. L. Schroeder, and M. D. Powell (2012). "Observed Characteristics of Tropical Cyclone Vertical Wind Profiles and Low-level Wind Maxima." *Weather and Forecasting*, doi:10.1175/WAF-D-11-00155.1.

Giammanco, I. M., J. L. Schroeder, and M. D. Powell (2012). "Observed Characteristics of Tropical Cyclone Vertical Wind Profiles." *Wind and Structures* 15, 65-86.

Hirth, B. D., J. L. Schroeder, S. Gunter, and J. Guynes (2012). "Measuring a Utility Scale Turbine Wake Using the TTUKa Mobile Research Radars." *Journal of Atmospheric and Oceanic Technology* **29,** 765-771.

Hirth, B. D., and J. L. Schroeder (2012). "Documenting Wind Speed and Power Deficits behind a Utility-Scale Wind Turbine." *Journal of Applied Meteorology and Climatology* 52, 39–46.

Hirth, B. D., J. L. Schroeder, S. W. Gunter, and J. Guynes (2014). "Coupling Doppler Radar-Derived Wind Maps with Operational Turbine Data to Document Wind Farm Complex Flows." *Journal of Wind Energy*. Submitted.

Hirth, B., J. L Schroeder, and S. Gunter (2011). "Observing Wind Turbine Wakes using Research Radar." *The Wind Engineer* 5-6.

Hoover, D., A. Bilbao, and J. A. Rice (2012). "WiseMote: A Novel Low Power, Low-Noise Wireless Sensor Network for Structural Health Monitoring." *Smart Structures and Systems* 10, 3: 271-296.

Hu, Y., S. Parameswaran, J. Tan, S. Dharmarathne, N. Marathe, Z. Chen, R. Grife, and A. Swift (2010). "Computing Turbulent Far-Wake Development behind a Wind Turbine with and without Swirl." *Wind & Structure*, *an International Journal* 18: 232-243.

Huang, G., and X. Chen (2007). "Wavelet-based Estimations of Evolutionary Spectra and its Application to Downburst Winds." *Engineering Structures* 31: 976-989.

Jie, D., and X. Chen (2012). "Assessing Small Failure Probability by Importance Splitting Method and Its Application to Wind Turbine Extreme Response Prediction." *Engineering Structures* 5: 180-191.

Karpat, F., and S. Ekwaro-Osire (2011). "Efficiency of High Contact Ratio Involute Spur Gears with Asymmetric Teeth." *Journal of Mechanical Design* 13: 319-327.

Liu, C., A. Morse, K. Rainwater, and L. Song (2012). "Mathematical Modeling of Concentration Polarization in a Reverse Osmosis Channel with Parabolic Crossflow Profile." *Water Research*. Under review.

Liu, C., K. Rainwater, and L. Song (2012). "Calculation of Energy Consumption for Crossflow RO Desalination Processes." *Desalination and Water Treatment* 42: 1-3, 295-303.

Lui, C., K. Rainwater, and L. Song (2010). "Determinations and Analyses of Energy Efficiency in Reverse Osmosis Desalination Processes." *Journal of Membrane Science.* Under review.

Liu, C., K. Rainwater, and L. Song (2011). "Energy Analysis and Efficiency Assessment of Reverse Osmosis Desalination Process." *Desalination.* In press.

Liu, M. Y., D. Zuo, and N. P. Jones (2013). "Analytical and Numerical Study of Deck-stay Interaction in a Cable-stayed Bridge in the Context of Field Observations." *Journal of Engineering Structures*. Under review.

McComb, R. and A. Schiller (2012). "Does More Investment in Green Energy make Paychecks Greener in Wind Power?" *Journal of Environmental Economics and Management*. Submitted.

Orwig, K. D. and J. L. Schroeder (2007). "Near-Surface Wind Characteristics of Extreme Thunderstorm Outflows." *Journal of Wind Engineering and Industrial Aerodynamics* 95: 565-584.

Parameswaran, S., Y. Hu, S. Dharmarathne, and N. Marathe (2011). "Computing Turbulent Far-Wake Development Behind a Wind Turbine with and without Swirl." *Wind and Structures: International Journal.* Accepted for publication.

Rainwater, K., P. Nash, L. Song, and J. Schroeder (2013). "The Seminole Project: Renewable Energy for Municipal Water Desalination." *Journal of Contemporary Water Research and Education* 151: 50-60.

Schiller, A., D. De Silva, R. McComb, Y. Moh, and A. Vargas (2009). "The Effect of Migration on Wages: Evidence from a National Experiment." *American Economic Review* 100(2). Papers and Proceedings.

Storm, B., J. Dudhia, S. Basu, A. Swift, and I. Giammanco (2007). "Evaluation of the Weather Research and Forecasting (WRF) Model on Low-level Jets: Implications for Short-term Wind Energy Forecasts." *Wind Energy* 12.1: 81-90.

Walter, K., C. Weiss, A. Swift, J. Chapman, and N. K. Walter (2009) "Speed and Direction Shear in the Stable Nocturnal Boundary Layer." *Journal of Solar Energy Engineering* 131; 011013. 1 to 7.

Walter, K., C. Weiss, A. Swift, J. Chapman, and N. D. Kelley (2007). "Speed and Direction Shear in the Stable Nocturnal Boundary Layer. Part I: Numerical Simulations of Turbine Power Production." *Journal of Solar Energy Engineering* 131: 011013.

Walter, K., C. Weiss, A. Swift, J. Chapman, and N. D. Kelley (2007). "Speed and Direction Shear in the Stable Nocturnal Boundary Layer. Part II: Observations." *Journal of Solar Energy Engineering* 131: 011017.

Technical Presentations:

Aguilar, T. A., and J. Schroeder (2009). "Near-Surface Wind Flow Characteristics of a Thunderstorm Outflow Event." Williamsburg, Virginia: 34th Conference on Radar Meteorology. Oct 5-9. Proceedings.

Alemayehu, F. M., and S. Ekwaro-Osire (2012). "Uncertainty Considerations in the Dynamics of Gear-Pair." Houston, Texas: ASME International Mechanical Engineering Congress & Exposition. Nov 9–15. Proceedings.

Alemayhu, F. M., and S. Ekwaro-Osire (2011). "Probabilistic Multibody Modeling of Gear Pairs." Denver, Colorado: ASME International Mechanical Engineering Congress and Exposition. Nov 11-17. Proceedings.

Alemayehu, F. M., and S. Ekwaro-Osire (2012). "Probabilistic Analysis in Multibody Dynamic." Berlin, Germany: International Conference on Integrated Design and Process Technology. June 10-14. Proceedings.

Alemayehu, F. M. and S. Ekwaro-Osire (2012). "Uncertainty in the Dynamics of Gear-Pair Fatigue and Fracture." Costa Mesa, California: SEM Annual Conference & Exposition. June 11-14. Proceedings.

Anderson, W. C., S. Basu, and C. W. Letchford (2007). "Next-generation Subgrid-scale Closures for Large-eddy Simulation of Turbulent Flow in the Atmospheric Boundary Layer." Cairns, Australia*:* Twelfth International Conference on Wind Engineering. July 1-6. Presentation.

Basu, S. (2009). "Addressing a Few Emergent Challenges in Wind Power Meteorology." Bloomington, IN*:* Vishor Lecture, Department of Geography, University of Indiana. Presentation.

Basu, S., F. C. Bosveld, and A. A. M. Holtslag (2009). "Stable Boundary Layers with Low-Level Jets: What did we learn from the LES Comparison with GABLS?" San Francisco, CA*:* American Geophysical Union Fall Meeting. December 14-18. Presentation.

Basu, S. (2009). "GABLS 3rd LES intercomparison Study." Boulder, CO*:* GABLS Workshop. June 26-27. Presentation.

Basu, S., and A. A. M. Holtslag (2009). "Solving the Mysteries of Decoupling, Run-away Surface Cooling and Crashing in Stable Atmospheric Boundary Layer Model Studies." Boulder, CO*:* GABLS Workshop. June 26-27. Presentation.

Bayne. S. (2012). "Major Key Challenges on Grid Integration." Lubbock, Texas: National Wind Resource Center Symposium on the Underperformance of Wind Farms. March 28-30. Presentation.

Bilbao, A., D. Hoover, J. Rice, and J. Chapman (2011). "Ultra-low Power Wireless Sensing for Long-term Structural Health Monitoring." San Diego, CA: SPIE Smart Structures/NDE 2011, Vol. 6932. Proceedings.

Basu, S., A. Ruiz-Columbie, and S. Harshan (2008). "Deriving Monin-Obukhov Similarity Functions from Dynamic Large-eddy Simulations." San Francisco*,* CA: American Geophysical Union Fall Meeting. 15-19 December.

Chamana, M. and S. B. Bayne (2011). "Modeling and Control of Directly Connected and Inverter Interfaced Sources in a Microgrid." Boston, MA: 43rd North American Power Symposium. August 4-6. Presentation.

Chamana, M., and S. B. Bayne (2011). "Modeling and Control of a Battery Management System (BMS) in a Microgrid." Amsterdam, Netherlands: 33rd International Telecommunications Energy Conference. October 9-13. Presentation.

Chapman, J. (2009). "Modern Wind Technology." Raleigh, NC*:* US-Korea Conference on Science, Technology and Entrepreneurship. July 16-19. Presentation.

Chapman, J. (2009). "Wind Energy Issues." Lubbock, TX*:* 1st Annual IEEE Green Technology Conference. April 16-17. Presentation.

Chen, X., N. Marathe, S. Dharmarthne, Y. Hu, and S. Parameswaran (2011). "Review of Wind Turbine Wake Studies in the Past Five Years," Amsterdam, Netherlands: 33rd International Telecommunications Energy Conference. October 9-13. Presentation.

Chen, X., N. Marathe, S. Dharmarathne, H. Yingying, and S. Parameswaran (2011). "Review of Wind Turbine Wake Studies in Past Five Years." Amsterdam, Netherlands: 13th International Conference on Wind Engineering, July 11-15. Presentation.

Correa, A. C., G. Hill, R. McComb, A. Swift, and J. Zak. (2009). "Green Campus Action Plan: Good Stewardship, Good Citizenship, Good Business." Lubbock, TX: Texas Tech University. April 15. Panel presentation.

De-Silva, D., R. McComb, and A. Schiller (2011). "Does More Investment with Green Energy Make Paychecks Greener in Wind Power?" Boston, MA: International Industrial Organization Conference. April 10. Presentation.

De-Silva, D. (2011). "Firm Entry and Growth in the Green Industry." St. Louis, MO: Midwest Economics Association. March 16-19. Presentation.

Durukan, I., S. Ekwaro-Osire, and F. M. Alemayehu (2010). "Energy Storage System for Wind Turbine." Vancouver, British Columbia, Canada: 2010 ASME International Mechanical Engineering Congress & Exposition. Nov 12-18. Presentation.

Ekwaro-Osire, S. (2011). "On Spur Gears with Asymmetric Teeth." Boulder, CO: National Wind Technology Center. March 11. Presentation.

Ekwaro-Osire, S. (2011). "A Comprehensive Approach for Accounting for Uncertainty in Gearbox Failure of Wind Turbines." Jeju Island, South Korea: International Conference on Integrated Design and Process Technology, June 12-16. Presentation and proceedings.

Ekwaro-Osire, S. (2011). "A Comprehensive Approach for Accounting for Uncertainty in Gearbox Failure of Wind Turbines." Lubbock, TX: Wind Science and Engineering Wednesday seminar series. February 9. Presentation.

Ekwaro-Osire, S. (2011). "A Comprehensive Approach for Mitigation and Prediction of Gearbox Failure of Wind Turbines." Norwood, MA: FM Global. January 28. Invited talk.

Ekwaro-Osire, S., T. H. Jang, I. Durukan, F. M. Alemayehu, and F. Karpat (2011). "Experimental Study of Gears with Asymmetric Teeth." Denver, CO: ASME International Mechanical Engineering Congress and Exposition. Nov 11-17. Proceedings.

Gilliam, X., S. Basu, and C. Ho (2007). "Detection of Intermittent Turbulence in the Stable Boundary Layer using Empirical Mode Decomposition." Acapulco, Mexico: NG548-06 AUG Joint Assembly. May 22-25. Presentation.

Hirth, B., and J. Schroeder (2009). "Examination of the Coastal Transition Zone of Hurricane Frances." San Juan, Puerto Rico: 11th Americas Conference on Wind Engineering. May 01. Proceedings.

Gong, K. and X. Chen (2011). "Influence of Translation Model on Modeling and Simulation of non-Gaussian Stochastic Processes." Amsterdam, The Netherlands: 13th International Conference on Wind Engineering. July 11. Submitted.

Gong, K., and X. Chen (2012). "Estimating Extremes of Combined Gaussian and non-Gaussian Response Processes." Notre Dame, Indiana: 11th ASCE Joint Specialty Conference on Probabilistic Mechanics and Structural Reliability (EMI/PMC2912). June 17-20. Presentation.

Gong, K., and X. Chen (2012). "Prediction of Wind Turbine Extreme Response to Non-Gaussian Wind Field." Seattle, WA: 12th Americas Conference on Wind Engineering (12ACWE). June 16-20. Submitted.

Gong, K., and X. Chen (2012). "Understanding the Dynamic Coupling of Wind Turbine Tower and Blades." Seattle, WA: 12th Americas Conference on Wind Engineering (12ACWE). June 16-20. Submitted.

Gong, K., and X. Chen (2012). "Estimating Extremes of Combined Gaussian and non-Gaussian Response Processes." South Bend, Indiana: 2012 Joint Conference of the Engineering Mechanics Institute and the 11th ASCE Joint Specialty Conference on Probabilistic Mechanics and Structural Reliability (EMI/PMC2012). June 17-20. Proceedings.

Gunter, W. S., and J. L. Schroeder (2012). "High-Resolution Full-Scale Observations of Thunderstorm Outflow Winds." Hyannis, Massachusetts: 3rd Annual AAWE Workshop. Aug 12-14. Presentation.

Gunter, W. S., and J. L. Schroeder (2013). "High-Resolution Full-scale Observations of Thunderstorm Outflow Winds." Seattle, WA: 12th Americas Conference on Wind Engineering (12ACWE). Jun 16-20. Presentation.

Harshan, S., S. Basu, and A. Ruiz Columbie (2009). "Evaluating the Performance of the WRF Model in Representing the Antarctic Boundary Layer." Boulder, CO*:* 10th WRF Users' Workshop. June 23-26. Presentation.

Ho, C., X. Gilliam, and S. Basu (2009). "Detecting Intermittent Turbulence using Advanced Signal Processing Techniques." Orlando, FL*:* 47th AIAA Aerospace Sciences Meeting. January 5-8. Presentation.

Hirth, B. D., and J. L. Schroeder (2012). "Measurements of Utility-Scale Turbine Wakes using the Texas Tech University Ka-band Mobile Research Radars." Hyannis, Massachusetts: 3rd Annual AAWE Workshop. Aug 12-14. Presentation.

Hirth, B. D., and J. L. Schroeder (2013). "Using the TTUKa Mobile Doppler Radars to Measure Complex Flows in Wind Farms." Seattle, WA: 12th Americas Conference on Wind Engineering (12ACWE). Jun 16-20. Presentation.

Hirth, B. D., and J. L. Schroeder (2013). "Measuring Turbine Wakes and Complex Flows in Wind Farms using the TTUKa Mobile Research Radars." Cambridge, UK: 6th European and African Conference on Wind Engineering. June 7-11. Accepted.

Hirth, B. D., and J. L. Schroeder (2013). "Documenting Complex Flows in Wind Farms using the TTUKa Mobile Research Radars." Austin, Texas: Fourth Conference on Weather, Climate, and the New Energy Economy. January 6-10. Presentation.

Hirth, B. D., and J. L. Schroeder (2013). "Measurements of the Complex Flow through a Wind Farm using Mobile Doppler Radars." Vienna, Austria: European Wind Energy Association (EAWE) Annual Conference. Feb 4-7. Presentation.

Hirth, B. D., and J. L. Schroeder (2012). "Measuring Complex Flows in Wind Farms using Advanced Doppler Radars." Vienna, Austria: European Academy of Wind Energy (EAWE) Annual Conference. Feb 4-7. Presentation.

Hirth, B. D., and J. L. Schroeder (2013). "Measuring Complex Flows in Wind Farms using Advanced Doppler Radars." Chicago, IL: American Wind Energy Association, WindPower 2013, May 5-8. Presentation.

Hirth, B. D., and J. L. Schroeder (2014). "Doppler Radar Observations of Turbine Wakes and Complex Flows within Wind Farms." Copenhagen, Denmark*:* 2013 International Conference on Aerodynamics of Offshore Wind Energy Systems and Wakes, June 17-19. Submitted.

Hu, Y., S. Parameswaran, T. Liu, S. Dharmarathne, R. Grife, and A. Swift (2010). "Computing Turbulent Far-Wake Development Behind a Wind Turbine with and without Swirl." Chapel Hill, NC: Fifth International Symposium on Computational Wind Engineering. May 23-27. Presentation.

Karpat, F., S. Ekwaro-Osire, and E. Karpat (2012). "A Virtual Tool for Wear Simulation of Standard and Non-Standard Spur Gears." Houston, Texas: ASME International Mechanical Engineering Congress & Exposition. Nov 9-15. Presentation.

Karpat, F., S. Ekwaro-Osire, and E. Karpat (2012). "A Virtual Tool for Wear Simulation of Standard and Non-Standard Spur Gears." Houston, Texas: 2012 ASME International Mechanical Engineering Congress & Exposition. Nov 9-15. Proceedings.

Karpat, F., and S. Ekwaro-Osire (2012). "Power Losses of High Contact Ratio Involute Spur Gears with Asymmetric Teeth." Houston, Texas: 2012 ASME International Mechanical Engineering Congress & Exposition. Nov 9-15. Presentation.

Karpat, F., and S. Ekwaro-Osire (2012). "Power Losses of High Contact Ratio Involute Spur Gears with Asymmetric Teeth." Houston, Texas: 2012 ASME International Mechanical Engineering Congress & Exposition. Nov 9-15. Proceedings.

Karpat, F., and S. Ekwaro-Osire (2010). "Efficiency of the High Contact Ratio Involute Spur Gears with Asymmetric Teeth." Vancouver, British Columbia, Canada: 2010 ASME International Mechanical Engineering Congress & Exposition. Nov 12–18. Proceedings.

Kersh, K. L., P. H. Gowda, S. Basu, T. A. Howell, S. O'Shaugnessy, N. Rajan, and O. Z. Akasheh (2009). "Vegetation Fraction Mapping with Artificial Neural Network and High Resolution Multispectral Aerial Imagery Acquired During BEAREX07." San Francisco, CA*:* American Geophysical Union Fall Meeting. December 14-18. Proceedings.

Kiesling, E. (2010). "Extreme Weather Safety on Wind Farms." Austin, Texas: American Wind Energy Association, Wind Power Health and Safety Workshop. October 26. Presentation.

McNeill, J., and D. Zuo (2011). "Inhomogeneous, non-Gaussian Low-level Jet Simulation: Implications for Wind Turbine Fatigue Loads." Anaheim, CA: WINDPOWER 2011 Conference & Exhibition. May 22-25. Submitted.

McNeill, J., and D. Zuo (2011). "Low-level Jet Characterization and Implications for Wind Turbine Inflow Simulation." Amsterdam, Netherlands: 13th International Conference on Wind Engineering. July 10-15. Presentation.

Orwig, K. D., and J. Schroeder (2009). "Full-Scale Strong Winds from a Time-Varying Perspective." San Juan, Puerto Rico: 11th Americas Conference on Wind Engineering. June 22-26. Proceedings.

Parameswaran, S. (2012). “CFD Study of Wake Interaction of Two Wind Turbines.” Lubbock, Texas: National Wind Resource Center Symposium on the Underperformance of Wind Farms. March 28-30. Presentation.

Parameswaran, S., T. Maxwell, and S. Thyageswaran (2009). Held a technical three-day workshop at “Future Trends in Sustainable Surface Transportation.” Jointly sponsored by the department of Mechanical Engineering at TTU and the Coimbatore Institute of Technology in India. March 17-19.

Rainwater, K. A. (2011). “Permian Basin Groundwater Issues.” Big Spring. TX: Permian Basin Regional Planning Commission Annual General Membership Meeting. October 12. Presentation.

Rainwater, K. A. (2011). “Desalinization Program.” Seminole, TX: Innovative Farming: Integrating Limited Water Resources into Today’s Farming Conference, Llano Estacado Underground Water Conservation District and AgrilLife Extension. December 6. Presentation.

Rainwater, K. (2011). “Reducing the Stress of Rural Community Desalination with Renewable Wind Energy.” San Antonio, TX: Multi-States Salinity Coalition. February 17-18. Presentation.

Rainwater, K. (2011). “Municipal Demonstration of a Wind-powered RO System.” South Padre Island, TX: South Central Membrane Association Annual Conference. September 28. Presentation.

Reddy, D., and S. Bayne (2011). “ASIC Architecture Development for Energy Harvesting.” Lubbock, TX: Texas Tech University Graduate research poster presentation.

Reddy, D., N. Beniwal, and S. Bayne (2011). “New ASIC Architecture Development for Energy Harvesting.” Amsterdam, Netherlands: 33rd International Telecommunications Energy Conference. October 9-13. Presentation.

Ruiz Columbie, A., S. Basu, P. S. Skinner, P. H. Gowda, and S. Harshan (2009). “Observational and Modeling Studies of Evening Transitional Boundary Layers.” San Francisco, CA: American Geophysical Union Fall Meeting. December 14-18. Presentation.

Ruiz Columbie, A., S. Basu, and S. Harshan (2009). “How does the WRF Model Capture the Intrinsic Features of Evening Transitional Boundary Layers?” Boulder, CO: 10th WRF Users’ Workshop. June 23-26. Presentation.

Schroeder, J. (2010). “Documenting the Engineering-Relevant Aspects of Extreme Thunderstorm Winds.” Atlanta, GA: NSF CMMI Research and Innovation Conference. January 4-7. Poster presentation.

Schroeder, J. L., B. D. Hirth, and J. G. Guynes (2013). “Using the TTUKa Radars to Measure Complex Flows Through Wind Farms.” Denmark Technical University, Denmark: Workshop. April 30. Presentation.

Schroeder, J. L. (2012). “Innovative Technologies to Investigate Fine-Scale Wind Flow.” Sydney, Australia: 15th Australian Wind Engineering Society Workshop. Feb 23-24. Presentation.

Schroeder, J. L. (2012). "Wind Characterization and Assessment." Lubbock, Texas*:* National Wind Resource Center Symposium on the Underperformance of Wind Farms. March 28-30. Presentation.

Schroeder, J., C. Weiss, and J. Guynes (2009). "Innovative Technologies to Investigate Fine-Scale Atmospheric Motions and their Impact." San Juan, Puerto Rico: 11th Americas Conference on Wind Engineering. June 22-26. Proceedings.

Schuetze, B., K. Rainwater, and L. Song (2011). "Development of a Small-Scale Reverse Osmosis System for Energy-Efficient Brackish Water Desalination at High Recoveries." Las Vegas, NV: Annual Meeting of the North American Membrane Society. June 8. Presentation.

Sim, C., S. Basu, and L. Manuel (2009). "The Influence of Stable Boundary Layer Flows on Wind Turbine Fatigue Loads." Orlando, FL: 47th AIAA Aerospace Sciences Meeting. January 5-8. Presentation.

Sim, C., L. Manual, and S. Basu (2009). "Simulation and Analysis of Wind Turbine Loads for Neutrally Stable Inflow Turbulence." San Francisco, CA: American Geophysical Union Fall Meeting. December 14-18. Presentation.

Song, L. (2010). "Energy Analysis and Cost Minimization of RO Desalination Processes." South Padre Island, TX: South Central Membrane Association Annual Conference. September 28. Presentation.

Storm, B., S. Basu, and J. Dudhia (2007). "Advanced Research WRF (ARW) Modeled Low-level Jet Climatology Compared to Observed Climatologies." Acapulco, Mexico: American Geophysical Union Joint Assembly. May 22-25. Presentation.

Storm, B., S. Basu, and J. Dudhia (2007). "Sensitivities of the WRF Model in Forecasting Low Level Jet Events." Los Angeles, CA: WINDPOWER Conference. June 3-6. Presentation.

Storm, B., S. Basu, and J. Dudhia (2007). "WRF Modeled Low-level Jet Climatology Compared to Observed Climatologies: Weakness and Strengths." Boulder, CO: 8th Annual WRF User's Workshop. June 11-15. Proceedings.

Storm, B., S. Basu, and J. Dudhia (2007). "Advanced Research WRF (ARW) Modeled Low-level Jet Climatology Compared to Observed Climatologies." Park City, UT: 22nd Conference on Weather Analysis and Forecasting/18th Conference on Numerical Weather Prediction. June 25- 29. Proceedings.

Storm, B., J. Dudhia, and S. Basu (2007). "WRF PBL Sensitivities and Verification in Forecasting Low-level Jet Events." Boulder, CO: 8th Annual WRF User's Workshop. June 11-15. Presentation.

Storm, B., J. Dudhia and S. Basu (2007). "Sensitivities of the Weather Research and Forecasting (WRF) Model in Forecasting Low-level Jet Events and the Impact on Forecasting Severe Weather." Park City, UT: 22nd Conference on Weather Analysis and Forecasting/18th Conference on Numerical Weather Prediction. June 25-29. Presentation.

Swift, A., and R. Walker (2011). "Workforce and Educational Programs for the Wind Energy Industry." Atlanta, GA: WINDPOWER 2012 conference. June 3-6. Proceedings.

Swift, A. (2009). "Wind Power Systems." Lubbock, TX: IEEE Green Technology Conference Short Course. April 16-17. Presentation.

Swift, A. (2009). "Wind Energy and Wind Turbines." Bellevue, WA: American Society of Agricultural and Biological Engineers. October 11-14. Presentation.

Swift, A. (2009). "Wind Energy Programs at Universities." Davis, CA: California Energy Commission's Wind Energy Collaborative. U.C. Davis. March 4. Presentation.

Swift, A. (2009). "New Roadmaps for Wind and Solar Research and Development." Published testimony before the Committee on Science and Technology, Subcommittee on Energy and the Environment, U.S. House of Representatives. July 14, 2009. Published by Office of the Clerk: HSY195.200

Walker, R., S. Bayne, M. Giberson, S. Nimmagadda, and A. Islam (2011). "Wind Turbine Integration and Model Validation in the ERCOT and SPP Markets." Atlanta, GA: WINDPOWER 2012 conference. June 3-6. Proceedings.

Walker, R. (2012). "An Industrial Perspective on Wind Farms' Underperformance." Lubbock, Texas: National Wind Resource Center Symposium on the Underperformance of Wind Farms. March 28-30. Presentation.

Walker, R. (2011). "The History and Future of Wind Energy in Texas." Sweetwater, TX: Texas Wind Energy Clearinghouse Transmission Summit. January 13-14. Presentation.

Walker, R., and A. Swift (2009). "Filling the Wind Industry Need for Trained Professionals." Chicago, Ill: American Wind Energy Association WINDPower. May 4-7 Poster.

Walter, K. R., C. C. Weiss, J. Chapman, and N. D. Kelley (2007). "Tall Tower Wind Shear Observations in the Stable Nocturnal Boundary Layer." Reno, NV: 45th American Institute of Aeronautics and Astronautics (AIAA) Aerospace Sciences Meeting. AIAA- 2007-1224. Jan. 8-11. Proceedings.

Walter, K. R., C. C. Weiss, J. Chapman, and N. D. Kelley (2007). "Observations of Extreme Speed and Directional Wind Shear in the U.S. Great Plains." Milan, Italy: 2007 European Wind Energy Conference and Exhibition. May 7-10. Proceedings.

Zuo, D. (2012). "Assessment of Wind Turbine Loading in Stable Atmospheric Boundary Layers based on Conditionally Simulated Inflow Fields." New York, NY: 11th International Conference on Structural Safety & Reliability. June 16-20. Abstract submitted.

Subtask 3.4: Provide Outreach Activities at Wind Energy-Related Conferences and Tradeshows, including WINDPOWER Conferences.

The NWI has dedicated time and energy to provide substantial participation to the annual AWEA national WINDPOWER conference every year between 2007 and 2013. These efforts extend beyond simple attendance and/or making oral or poster presentations, but also include the annual support for a booth in the exhibit hall. Leveraging its undergraduate program, NWI has also consistently supported a significant number of students to attend this conference. Faculty and graduate students also attended other technical conferences over the same period, but this was nominally to give a technical poster or podium presentation.

Subtask 3.5: Complete "Run on the Wind" summer youth camps for grades 7-11 and develop wind energy instructional materials for secondary and middle school teachers.

3.5.1. Run on the Wind Summer Camp.

TTU (in collaboration with IDEAL, a TTU-sponsored K-12 education initiative) has hosted a two-week summer camp for five years. The camp is focused on grades 8-11 and the NWI has provided in-kind materials such as space, controlled access to the research facilities etc. Curricula were created and implemented at each camp, using the experience of the previous camp to further develop and improve the educational experience. The camp hosted an average of 12 high school students each summer, for a total of 60 students with a special emphasis on disadvantaged groups.

NWI staff have developed curriculum and provided activities for the camps, as well as provided instruction. Camps were organized and conducted by IDEAL, a TTU organization that conducts university summer camps. The Institute for the Development and Enrichment of Advanced Learners (IDEAL) at TTU focuses on science, technology, engineering, and mathematics programs for K-12. IDEAL helps to encourage students to pursue a post-secondary education and increase their knowledge about admission to a two- or four-year institution of higher learning. The mission of IDEAL is to provide distinctive and unique outreach programs that promote academic excellence and diversity, with the biggest focus on introducing underrepresented students to a collegiate experience and dispelling myths and fears about higher education. All programs are designed to give children a successful academic experience on a university campus. See Appendix A for a typical Run on the Wind camp schedule (June 9-14, 2013).

3.5.2. Curriculum Development.

3.5.2.1. Introduction.

With the increased need for employees in the wind energy industry, emphasis on knowledge and skill development in secondary education is growing. Agricultural Education has traditionally been a training ground for hands-on mechanical skills and concepts. Agricultural Education is a Career and Technical Education program teaching both vocational subjects and literacy programs. Graduates of Ag Education can directly enter the workforce, or continue their education at varying levels of post-secondary institutions. Emphasis has grown at all levels of post-secondary institutions with the creation of programs at the Texas State Technical College, two-year junior colleges and at four-year institutions with bachelors and graduate programs. Teachers are responsible for assuring students are prepared for every potential avenue. The inclusion of the wind energy industry to the agricultural education curriculum will impact the number of future employees at all levels of the industry.

With increasing state requirements, subjects cannot be added to programs if they do not coincide with state mandates. Texas has implemented the Texas Essential Knowledge and Skills (TEKS). Every class taught in the public school system must teach the outlined TEKS for that particular class. Many of the TEKS are broad and can be taught in the context the teacher chooses. Creating new teaching resources must align with the TEKS if they are to be adopted. The implementation of new educational programs is also exponentially more successful if is coincides with teacher professional development. Agriculture teachers have a continuing desire and need for in-service training to ensure their skills and content knowledge are current (Barrick, Ladewig, & Hedges, 1983). Annually, the agriculture teachers of every state come together for professional development in a wide range of topics.

3.5.2.2. Program Development.

Teachers were asked what wind energy topics could be included in agricultural instruction and what resources would help increase the adoption of the lessons. Additionally, an assessment of the TEKS for all agriculture courses was conducted to determine where wind energy topics and skills could be taught. Three courses were selected to target for lesson development: Principles of Agriculture, Natural Resources, and Energy and Natural Resources. Identified topics included: geographic impact of wind energy, science of energy, careers, renewable energies, politics, economic impact, myths of wind energy, history, story of a turbine, barriers, and growth of the industry. Resources included hands-on projects, PowerPoints, and visual aids. Topics were aligned with TEKS from each course and lessons and activities were outlined.

3.5.2.3. Educational Resource.

Identified topics were combined and resources were centered on six general subjects (Past, Present and Future, Careers, What is Energy, Controversial Issues, Wind Turbine Technology, Wind Farm Economics, and Creating Energy) and three independent activities. Twenty one documents were created for the instruction. A detailed lesson plan was created for each subject and five were accompanied by a PowerPoint. Lesson plans included TEKS to be addressed, learning outcomes, talking points, directions, and teacher instructions. When needed, lesson plans were accompanied by handouts or worksheets. Lessons were created to emphasized student-centered instruction and inquiry-based techniques when possible. The three standalone activities were designed to reinforce instruction, and to involve students.

Standalone activities were: *Turbine Design Competition*, *Windiest Place at School*, and *Producing More Energy*. *The Turbine Design Competition* challenged students to make their own wind turbine from everyday items such as a ceiling fan motor. Students would work to make the most productive turbine. *The Windiest Place at School* project gave students the opportunity to use an anemometer around the facility. Finally, *Producing More Energy* was developed around kits from KidWind to explore the use of blade length and design, and the size of gears.

3.5.2.4. Professional Development.

In August of 2011, at the professional development conference for the Vocational Agriculture Teachers Association of Texas, a 90 minute workshop was conducted to introduce the teaching resources. Twenty-three teachers attended and received resources on CD. The program included an overview of the project, and introduction to the materials, and samples of the materials. Teachers were also instructed about the TEKS that could be addressed with the lessons. Each activity was described and a model of a turbine design was demonstrated. While the implementation of the lessons is not quantifiably known, qualitatively it was well received and follow-up discussions indicate that the resources have been adopted by several participants.

Bibliography

Addison, P. S. (2002). *The Illustrated Wavelet Transform Handbook*. New York: Taylor and Francis TasGroup.

Agarwall, P., and L. Manuel (2008). “Extreme Loads for an Offshore Wind Turbine using Statistical Extrapolation from Limited Field Data.” *Wind Energy* 11: 673-684.

Ameya, S., and B. Wim (2007). "Influence of Different Wind Profiles Due to Varying Atmospheric Stability on the Fatigue Life of Wind Turbines." *Journal of Physics: Conference Series* 75: 012056.

Arroyo, J. (2011). *Updates on TWDB’s Innovative Water Technology Programs*. Report to Texas Water Development Board, Austin, Texas. http://www.twdb.state.tx.us/innovativewater/doc/20110405_Updates_IWT_Program.pdf. Accessed February 2013, 7 p.

Au, S. K., and J. L. Beck (2001). “Estimation of Small Failure Probabilities in High Dimensions by Subset Simulation.” *Probabilistic Engineering Mechanics* 16: 263-277.

Baker, M., and A. Swift (2011). “Wind Energy Workforce Assessment.” Texas Workforce Commission. December.

Baker, M., A. Swift, and C. Henkhaus (2011). “Texas Wind Energy Workforce Gap Analysis: Implications for Secondary and Higher Education Programs in Agricultural Sciences.” Western Region Agricultural Education Conference. Submitted.

Banta, R. M., R. K. Newsom, J. K. Lundquist, Y. L. Pichugina, R. L. Coulter, and L. Mahrt (2002). "Nocturnal Low-level Jet Characteristics Over Kansas During Cases-99." *Boundary-Layer Meteorology* 105:221-52.

Barber, N. L. (2009). *Summary of Estimated Water Use in the United States in 2005. Fact sheet 2009-3098*. United States Geological Society, US Department of the Interior. http://pubs.usgs.gov/fs/2009/3098

Barthelmie, R. J., et al (2007). “Modeling and Measurements of Power Losses and Turbulence Intensity in Wind Turbine Wakes at Middelgrunden Offshore Wind Farm.” *Wind Energ* 10: 517-528.

Barthelmie, R. J., et al (2009). “Modelling and Measuring Flow and Wind Turbine Wakes in Large Wind Farms Offshore.” *Wind Energy* 12: 431-444.

Barthelmie, R. J., et al (2010). “Quantifying the Impact of Wind Turbine Wakes on Power Output at Offshore Wind Farms.” *J. Atmos. Oceanic Technol*. 27: 1302-1317.

Barthelmie, R. J., and L. E. Jensen (2012). “Evaluation of Wind Farm Efficiency and Wind Turbine Wakes at the Nysted Offshore Wind Farm.” *Wind Energy*, 13: 573-586.

Barthelmie, R. J., and S. C. Pryor (2013). “An Overview of Data for Wake Model Evaluation in the Virtual Wakes Laboratory.” *Appl. Energy* 104: 834-844.

Bilgili, M., A. Yasar, and E. Simsek (2011). "Offshore Wind Power Development in Europe and its Comparison with Onshore Counterpart." *Renewable and Sustainable Energy Reviews* 15:905-15.

Bradley, R. and S. Kalaswad (2003). *The Groundwater Resources of the Dockum Aquifer in Texas*. Report 359, Texas Water Development Board, Austin, Texas. 81 p.

Burton, T. et al (2011). *Wind Energy Handbook*. Wiley.

Calhoun, R., R. Heap, M. Princevac, R. Newsom, H. Fernando, and D. Ligon (2006). “Virtual Towers using Coherent Doppler Lidar During the Joint Urban 2003 Dispersion Experiment.” *Journal of Applied Meteorology* 45: 1116-1126.

Caughey, S. J., J. C. Wyngaard,and J. C. Kaimal (1979). "Turbulence in the Evolving Stable Boundary Layer." *Journal of the Atmospheric Sciences* 36:1041-52.

Center for Geospatial Technology (2006). E*stimated Usable Aquifer Lifetime*. Ogallala Map Series. Texas Tech University. http://www.gis.ttu.edu/OgallalaAquiferMaps/MapSeries.aspx. Accessed February 2013.

Chen, L., and C. W. Letchford (2005). "Proper Orthogonal Decomposition of two Vertical Profiles of Full-scale Nonstationary Downburst Wind Speeds[lzcl]." *Journal of Wind Engineering and Industrial Aerodynamics* 93:187-216.

Chen, L., and C. W. Letchford (2006). "Multi-scale Correlation Analyses of Two Lateral Profiles of Full-scale Downburst Wind Speeds." *Journal of Wind Engineering and Industrial Aerodynamics* 94:675-96.

Chen, L., and C. W. Letchford (2007). "Numerical Simulation of Extreme Winds From Thunderstorm Downbursts." *Journal of Wind Engineering and Industrial Aerodynamics* 95:977-90.

Chen, X., and G. Huang (2009). "Evaluation of Peak Resultant Response for Wind-excited Tall Buildings." *Engineering Structures* 31.4: 858-868.

Chowdhury, S., J. Zhang, A. Messac, and L. Castillo (2012). "Unrestricted Wind Farm Layout Optimization (UWFLO): Investigating Key factors Influencing the Maximum Power Generation." *Renewable Energy* 38: 16-30.

Cirrus Associates, LLC, 2009. *Evaluation of the Proposed Well Location for a Municipal Water Supply Well in the Dockum Aquifer, Gaines County, Texas, Project No. 02-013600.03*. Report to Texas Tech University Wind Science and Engineering Center, Lubbock, Texas. 41 p.

Cirrus Associates, LLC, 2011. *Geology Report Dockum Well SR-1, City of Seminole, Gaines County, Texas, Project No. 02-013600.01*. Report to Texas Tech University Water Resources Center, Lubbock, Texas. 68 p.

"Deep Cycle Battery FAQ" Northern Arizona Wind & Sun. http://www.windsun.com/Batteries/Battery_FAQ.htm#AGM

Del-Franco, M. (2009). *North American Wind Power* 6.7. 38.

Ding, J., and X. Chen (2013). "Assessing Small Failure Probability by Importance Splitting Method and its Application to Wind Turbine Extreme Response Prediction." *Engineering Structures* 54: 180-91.

Ding, J., K. Gong, and X. Chen (2013). "Comparison of Statistical Extrapolation Methods for the Evaluation of Long-term Extreme Response of Wind Turbine." *Engineering Structures* 57: 100-115.

Divya R. (2011). "New Architecture Development for Energy Harvesting." Texas Tech University. August 2011. Thesis.

Energy Matters, LLC. January 2010. http://www.energymatters.net to http://forums.energymatters.com.

Ewing, J., T. Jones, T. Yan, , A. Vreughenhil, D. Fryar, J. Pickens, K. Gordon, J. Nicot, B. Scanlon, J. Ashworth, and J. Beach (2008). *Groundwater Availability Model for the Dockum Aquifer, Final Report.* Texas Water Development Board, Austin, Texas. 510.

"First Solar Reaches US $1 Per Watt Milestone." *Renewable Energy World.com*, February 2010. http//www.renewableenergyworld.com/rea/news/article/2009/02/first-solar-passesus1watt.

Fitzwater, L. M., and S. R. Winterstein (2001). "Predicting Design Wind Turbine Loads from Limited Data: Comparing Random Process and Random Peak Models." *Journal of Solar Energy Engineering* 123.4: 364-371.

Freudenreich, K., and K. Argyriadis (2008). "Wind Turbine Load Level based on Extrapolation and Simplified Methods." *Wind Energy* 11.6: 589-600.

Gaumond, M., and coauthors (2013). "Evaluation of the Wind Direction Uncertainty and its Impact on Wake Modelling at the Horns Rev Offshore Wind Farm." *Wind Energy*. In press.

Green, C. (2009). “Integrating Renewables onto the Emerging Grid.” *ReNew Grid*. 1.

Grigoriu, M. (1995). *Applied non-Gaussian Processes: Examples, Theory, Simulation, Linear Random Vibration, and MATLAB solutions*. Englewood Cliffs, NJ: PTR Prentice Hall.

Haldar, A., and S. Mahadevan (2000). *Probability, Reliability and Statistical Methods in Engineering Design*. John Wiley & Sons, Inc.

Hirth, B. D., J. L. Schroeder, W. S. Gunter, and J. G. Guynes (2012). “Measuring a Utility-scale Turbine Wake using the TTUKa Mobile Research Radars.” *J. Atmos. Oceanic Technol*. 29: 766-771.

Hirth, B. D., and J. L. Schroeder (2013). “Documenting Wind Speed and Power Deficits behind a Utility-scale Wind Turbine.” *J. Appl. Meteor. Climatol*. 52: 39-52.

Hirth, B. D., J. L. Schroeder, W. S. Gunter, and J. G. Guynes (2013). “Coupling Doppler Radar-derived Wind Maps with Operational Turbine Data to Document Wind Farm Complex Flows.” *Wind Energy*. Accepted.

Holmes, J. D., H. M. Hangan, J. L. Schroeder, C. W. Letchford, and K. D. Orwig (2008). “A Forensic Study of the Lubbock-Reese Downdraft of 2002.” *Wind and Structures* 11: 137-152.

Hoshiya, M. (1995). “Kriging and Conditional Simulation of Gaussian Field.” *Journal of Engineering Mechanics* 121: 181-6.

IEC 61400-1. (2005). *Wind Turbines-Part I: Design Requirements*. Edition 3. International Electrotechnical Commission, Geneva, Switzerland.

Iungo, G. V., Y. Wu, and F. Porté-Agel (2013). “Field Measurements of Wind Turbine Wakes with Lidars.” *J. Atmos. Oceanic Technol.* 30: 274-287.

Jonathan, S., and M. Christian (2006). "Influence of Atmospheric Stability on Wind Turbine Power Performance Curves." *J. Solar Energy Eng* 128:531.

Jonkman J., S. Butterfield, W. Musial, and G. Scott (2009). “Definition of a 5-MW Reference Wind Turbine for Offshore System Development.” *Technical Report NREL/TP-500-38060,* National Renewable Energy Laboratory, Golden, CO.

Jonkman, J., and M. Buhl, (2005). “FAST user’s guide.” National Renewable Energy Laboratory, Golden, CO.

Karpat, F., and S. Ekwaro-Osire (2008). "Influence of Tip relief Modification on the Wear of Spur Gears with Asymmetric Teeth." *Tribology Transactions* 51.5: 581-588.

Käsler, Y., S. Rahm, and R. Simmet (2010). “Wake Measurement of a Multi-MW Wind Turbine with Coherent Long-range Pulsed Doppler Wind Lidar.” *J. Atmos. Oceanic Technol.* 27: 1529-1532.

Kelley, N. D., M. Shirazi, D. Jager, S. Wilde, J. Adams, M. Buhl et al (2004). "Lamar Low-Level Jet Project Interim Report." National Renewable Energy Laboratory.

King, K. (2008). *Renewable Energy Resource Assessment*. Washington, D.C.: Department of Energy.

Kipp and Zonen. *CM-3 Pyranometer Instruction Manual.*

Lewis, W. (1983). “Investigations of the Strength of Gear Teeth.” Engineers Club of Philadelphia, pp. 16–23. Proceedings.

Lillian, J. (2010). “Assessing Micro-Inverters’ Practicable Production Capabilities; What Types of PV Installations can Potential Energy Gains Justify Added Costs.” *Solar Industry* 2.12: 8.

Lin, A. D., and G. X. Kuang (2008). “Dynamic Interaction between Contact Loads and Tooth Wear of Engaged Plastic Gear Pairs.” *International Journal of Mechanical Sciences* 50.2: 205–213.

Manohar, C. (2011). “Modeling and Control of Directly Connected and Inverter Interfaced Sources in a Micro Grid.” Thesis. August 2011.

Maxwell, E. L. (1987). “A Quasi-Physical Model for Converting Hourly Global Horizontal to Direct Normal Insolation.” Solar Energy Research Institute. U.S. Department of Energy. August.

Meyers, J., and C. Meneveau (2012). "Optimal Turbine Spacing in Fully Developed Wind Farm Boundary Layers." *Wind Energy* 15: 305-317.

McKay, P., R. Carriveau, and D. S. Ting (2013). "Wake Impacts on Downstream Wind Turbine Performance and Yaw Alignment." *Wind Energy* 16: 221-234.

Milsoft Utility Solutions software, WindMil Version 7.3.7.6. Copyright 1998-2011 Auto-Desk, Inc. http://www.milsoft.com

Moraes, O. L. L. (1988). "The Velocity Spectra in the Stable Atmospheric Boundary Layer." *Boundary-Layer Meteorology* 43: 223-30.

Moriarty, P.J. (2008). "Database for Validation of Design Load Extrapolation Techniques." *Wind Energy* 11.6: 559-576.

Musial, W., S. Butterfield, and B. McNiff (2007). "Improving Wind Turbine Gearbox Reliability." European Wind Energy Conference. Milan, Italy. Presentation

Natarajan, A., and D. R. Verelst (2011). "Outlier Robustness for Wind Turbine Extrapolated Extreme Loads." *Wind Energy* 15.5: 679-697.

Nguyen, H. H., L. Manuel, and P. S. Veers (2011). "Wind Turbine Loads during Simulated Thunderstorm Microbursts." *Journal of Renewable and Sustainable Energy* 3: 053104-19.

Nieuwstadt, F. T. M. (1984). "The Turbulent Structure of the Stable, Nocturnal Boundary Layer." *Journal of the Atmospheric Sciences* 41: 2202-16.

Oyague, F. (2009). *Gearbox Modeling and Load Simulation of a Baseline 750-kW Wind Turbine Using State-of-the- Art Simulation Codes*. Golden, Colorado.

Pedersen, B.M., K.S. Hansen, S. Oye, M. Brinch and O. Fabian (1992). "Some Experimental Investigations on the Influence of the Mounting Arrangements on the Accuracy of Cup-anemometer Measurements." *Journal of Wind Engineering and Industrial Aerodynamics* 39: 373-383.

Pedersen, T. (2002).*Wind Turbine Power Performance Verification in Complex Terrain and Wind Farms*. Risø DTU Danish National Laboratory for Sustainable Energy. Technical University of Denmark. Presentation.

Politis, E. S., et al (2012). "Modeling Wake Effects in Large Wind Farms in Complex Terrain: the Problem, the Methods and the Issues." *Wind Energy* 15: 161-182.

Powel, C. A. (1964). *Electrical Transmission and Distribution Reference Book*. Pittsburg, PA: Westinghouse Electric Corporation.

Price, S. and R. Margolis (2010). *2008 Solar Technologies Market Report*. U.S. Department of Energy, Energy Efficiency and Renewable Energy. January.

Priestly, M. B. (1965)."Evolutionary Spectra and Nonstationary Processes." *Journal of Royal Statistical Society, Series B (Methodological)* 27: 204-37.

Puigcorbe, J., and A. De-Beaumont (2010). "Wind Turbine Gearbox Reliability: The Impact of Rotor Support." *Renewable Energy World Magazine*.

Rainwater, K., J. Stovall et al (2005). "Trans-boundary Impacts on Regional Ground Water Modeling in Texas." National Groundwater Association, September. 43.5 706-716.

Ribrant, J., and L. M. Bertling (2007). "Survey of Failures in Wind Power Systems With Focus on Swedish Wind Power Plants During 1997–2005." IEEE Transactions on Energy Conversion 22.1: 167–173.

Sanchez, J. (2010). "Tracked PV Array Systems and Performance." Data application from National Renewable Energy Labs. http://nrel.gov/rredc/pvwatts/

Schepers, J. G., T. S. Obdam, and J. Prospathopoulos (2012). "Analysis of Wake Measurements from the ECN Wind Turbine Test Site Wieringermeer, EWTW." *Wind Energy* 15: 575-591.

Shillington, S. (2009). "Austin Energy Proposes Huge Solar Plant." *Austinist*. January 2009. http://austinist.com/2009/01/29/austin_energy_has_proposed_a.php.

Sichani, M. T., S. R. K. Nielsen, and C. Bucher (2011). "Applications of Asymptotic Sampling on High Dimensional Structural Dynamic Problems." *Structural Safety* 33: 305-316.

Sichani, M.T., and S. R. K. Nielsen (2012). "First Passage Probability Estimation of Wind Turbines by Markov Chain Monte Carlo." *Structure and Infrastructure Engineering* 1-13.

Simiu, E., and R. H. Scanlan (1996). *Wind Effects on Structures: Fundamentals and Applications to Design* 3rd Edition. New York, NY: John Wiley & Sons, Inc. 1996.

Stull, R. B. (1988). *An Introduction to Boundary Layer Meteorology.* Springer.

Shinozuka, M., and C. Jan (1988). "Digital Simulation of Random Processes and its Applications." *Journal of Sound and Vibration* 25: 111-28.

Swift, A. (1980). "The Effects of Yawed Flow on Wind Turbine Rotors." Washington University. Thesis.

Swift, A., K. Rainwater, J. Chapman, , D. Noll, , A. Jackson, , B. Ewing, , L. Song, , G. Ganesan, , G. Marshall, V. Doon, and P. Nash (2009). *Wind Power and Water Desalination Technology Integration, Report 146*. Bureau of Reclamation, Denver, Colorado. 400 p.

Swift, A. (2009). "New Roadmaps for Wind and Solar Research and Development." Published and transcribed Testimony before the Committee on Science and Technology, Subcommittee on Energy and the Environment, US House of Representatives. July 14, 2009. Published by Office of the Clerk. HSY195.200.

Swift, A. (2010). "Texas Energy – Past and Present: Wind Energy: Value and Challenges for West Texas." *Lyceum E-Journal* 1.3, Midland. Summer .

"Sun or Moon Altitude/Azimuth Table: U.S. Cities and Towns." Naval Oceanography Portal, U.S. Naval Meteorology and Oceanography Command. http://www.usno.navy.mil/USNO/astronomical-applications/data-service/alt-az,us.

Trebilcock, M. (2009). "Taking a Deep Breath on Wind Power." National Wind Watch. *Energy Matters, LLC*. January. http://www.windwatch. org/documents/cost-of-pumped-hydro-storage/

Torcellini, P., N. Long, and R. Judkoff (2003). *Consumptive Water Use for US Power Production*. National Renewable Energy Laboratory Technical Report. (NREL/TP-550-33905) December.

U. S. Battery Manufacturing Company. ISO Certified. http://www.usbattery.com/usb_solar_renewable_energy_p2.html

Walker, R., K. Mehta, A. Swift, and K. Seger (2010). "Development of Workforce for Industry." Phoenix, Arizona: ASME 2010 4th International Conference on Energy Sustainability ES2010. May 17-22. Number: ES2010-90348.20 A. Proceedings

Walter, K. (2007). *Wind Power Systems in the Stable Nocturnal Boundary Layer*. Texas Tech University Lubbock, Texas. August.

Walter, K., C. C. Weiss, A. H. P. Swift, J. Chapman, and N. Kelley (2009). "Speed and Direction Shear in the Stable Nocturnal Boundary Layer." *Journal of Solar Energy Engineering* 131: 011013-7.

Wiser, R. and M. Bolinger (2009). *Wind Technologies Market Report*. U. S. Department of Energy. August 2010.

Wharton, S., and J. K. Lundquist (2010). "Atmospheric Stability Impacts on Power Curves of Tall Wind Turbines - an Analysis of a West Coast North American Wind Farm." Lawrence Livermore National Laboratory. Report.

Windographer, Mistaya Engineering Inc. http://www.mistaya.ca/windographer/overview.htm.